Mathematical modeling of the fatigue life following rim indentation test in aluminum alloy wheels

by

Mohit Bhatnagar

A THESIS SUBMITTED IN PARTIAL FULFILLMENT OF
THE REQUIREMENTS FOR THE DEGREE OF

MASTER OF APPLIED SCIENCE

in

THE FACULTY OF GRADUATE STUDIES

(Mechanical Engineering)

THE UNIVERSITY OF BRITISH COLUMBIA
(Vancouver)

January 2010

Abstract

The volume of components manufactured from cast aluminum alloys in both the aerospace and automotive industries has seen a tremendous rise in the past 10 years primarily due to their high strength to weight ratio. In the case of the automotive industry, cast wheels also provide aesthetically appealing designs for the consumers, which is another factor for their increased demand. The cyclic nature of in-service loading in some applications makes fatigue performance a key design consideration. Manufacturers use standardized testing procedures (SAE J328) to assess the fatigue life of wheels for regular driving or cornering conditions. Recently, a leading North American wheel manufacturing company has began testing the radial fatigue life of wheels following rim indentation. The development of this test has highlighted the need for a tool to support the wheel design process that is capable of predicting the fatigue life of cast components following permanent deformation.

A considerable amount of research work has already been conducted on establishing the effects of microstructure and casting defects on the fatigue life of cast aluminum alloy A356. However, there has been limited work published on the effects of initial plastic deformation on the fatigue life of cast alloy A356. Thus, the current research project aims to quantify the effects of initial plastic strain on the fatigue life of automotive wheels manufactured from A356. Specifically, the research aims to enhance the understanding of the impact of rim indentation on the fatigue life of a wheel.

A finite element model was developed to predict the deformation occurring during application of a static load during the rim indentation test. The residual stress distribution occurring after the T6 heat treatment process was used as an input to the rim indentation model. The model was then extended to calculate the stress state of the wheel under radial fatigue test conditions. Lab-scale experiments were performed to characterize the fatigue behavior of alloy A356 following different amounts of pre-strain (plastic strain). This data was used to develop an empirical relationship to relate the fatigue life to initial plastic strain and the cyclic stress state. Industrial-scale rim indentation and radial fatigue tests were used to validate the overall model predictions.

Table of Contents

List of Tables

List of Figures

Acknowledgements

I would like to extend my heartfelt gratitude towrads my supervisors Dr. Robert Hall and Dr. Daan Maijer, who have patiently guided me in this research project. Their invaluable advice and constructive feedback have helped me complete this project successfully. I would also like to thank Dr. Douglas Romilly and Dr. Edouard Asselin for agreeing to read this thesis and provide their insightful comments. My sincere thanks to Dr. Yves Nadot for his generosity in helping me in this project.

Next, I would like to express my sincere thanks to the wheel manufacturing company for their co-operation in allowing me to use their facility and product as part of the research project.

I would like to recognize Mr. Mathew Roy and Mr. Dave Marechad, Ph. D. students in the Materials Engineering department at UBC, Vancouver, for their help in this research project. I would also like to acknowledge the Materials Engineering Machine shop personnel who provided me with their technical assistance throughout this project.

I want to thank all my friends and colleagues in the UBC Mechanical Engineering Department, especially the Applied Mechanics ROTA Group for their stimulating discussions and seminars. Your academic advice helped me complete this thesis, and your friendship has made my time here memorable.

I want to thank my friends at Vancouver, especially Ms. Akila Kannan and my friends in India, especially Mr. Nakul Aggarwal and Mr. Tushar Mishra for being there for me, when I needed them the most.

Last but not least, I would like thank my parents and my sister for all their constant words of encouragement and having faith in me all the time.

To my parents and sister

1 Introduction

1.1. Automotive wheels

The use of cast aluminum alloys in wheel fabrication has resulted in a sharp increase in the demand for aesthetic wheels with intricate designs. The casting process has provided wheel designers with the freedom to explore designs with complicated geometry that are impossible to fabricate by the forging process [1]. Wheels made out of cast aluminum alloys have a higher aesthetic appeal compared to traditional forged steel. Moreover, cast aluminum alloys have a higher strength to weight ratio compared to forged steel which can potentially contribute in production of lighter wheels with better fuel efficiency [2][3]. Forged and welded steel wheels are cheaper than cast aluminum alloys wheels but lack the aesthetic appeal. The type of wheel chosen depends on the consumer's needs and budget.

Another trend in today's automotive industry is the increased demand for large diameter wheels. This demand is also driven by the aesthetic appeal of large diameter wheels with thin spokes and large rims. Owing to the high strength to weight ratio of cast aluminum alloys, these large diameter wheels have been made possible without sacrificing the structural integrity of the wheels [1].

Although, cast aluminum alloys are light and durable, their relatively low fatigue resistance hinders their application in structural components which undergo repetitive loading[2]. The cyclic nature of in-service loading in wheels makes fatigue life a key criterion for design purposes.

1.2. Wheel fatigue testing

An aluminum alloy wheel design must pass three tests before it can be approved for production [4]. Two of these tests - the radial fatigue and bending (cornering) fatigue (SAE J328) are the standard tests outlined by SAE for wheels used on passenger cars and light trucks to assess their in-service fatigue life characteristics. The third test is a drop test (SAE J 175) which is performed to assess the damage to the tire-wheel assembly from a sudden impact. Once in production, periodic quality assurance checks are also conducted on wheels to ensure that the standards continue to be met.

Some manufacturing companies have designed additional tests to ensure wheel quality. As part of its continuous self improvement strategy, a leading North American wheel manufacturing company has added rim indentation testing to its quality control program. In this test, the rim is indented (permanently deformed) by applying a static load. The deformed wheel is then tested for radial fatigue life. Wheel designs are rejected following rim indentation if they deform more than the permissible limit of 3mm. This testing protocol was designed to assess the ability of a wheel to withstand an event such as driving up a curb or through a deep pot hole which causes permanent rim deformation and may impact radial fatigue life.

1.3. Design tools

Once a new wheel design has been conceptualized, a prototype of the wheel is manufactured and tested through accelerated fatigue life tests prior to mass production. Based on the results of the fatigue tests, modifications are made in the wheel design if required [5]. This cycle of designing, manufacturing, testing and then modifying continues until a design is reached which satisfies the fatigue life criteria. This iterative method of wheel design is cumbersome and cost inefficient. Moreover, there is an added pressure in the automotive industry to minimize the time taken between the inception of wheel design and full-scale production [6].

The recent advancements in the computational capabilities of computers as well as the development of analysis software has led many manufacturing companies to employ Computer Aided Engineering (CAE) techniques in conjunction with traditional testing to opti-

mize part designs [6]. It has also been reported that fatigue testing without concurrent stress analysis does not yield optimum wheel designs [7]. The use of CAE analysis software enables a more thorough analysis of a system as compared to traditional methods. This research project aims to model the rim indentation test and radial fatigue test for automotive wheels using an available CAE tool. It should be understood that the current state of the art in fatigue modeling does not eliminate the traditional testing since fatigue life is dependent on several unpredictable factors [6]. This research work is focused on advancing the efforts in the use of these advanced analytical tools for wheel design.

2 Literature Review

2.1. Fatigue life of cast aluminum alloys

Cast aluminum alloys are being used in the aerospace and automotive industries to replace components made from forged steel and cast iron alloys. Cast aluminum alloys offer a better strength-to-weight ratio and hence can potentially improve fuel efficiency. However the casting process produces a wide range of discontinuities such as porosity, intermetallic particles, trapped oxide films as well as variations in microstructural features, all of which are deleterious to mechanical properties-especially fatigue life [8]. These factors either individually or in combination can result in the fatigue failure of cast aluminum alloys, hence the failure causing defect can be either one or combination of discontinuities.

One of the common aluminum alloys used for mass production of automotive components is A356 which has the composition by wt %: 7.25Si, 0.32Mg, 0.06Fe, <0.01Cu, <0.01Mn, <0.01Cr, <0.01Ni, <0.02Zn, <0.01Ti and <0.01B with the rest being aluminum. Silicon is present in an aluminum-silicon eutectic bonded to the primary aluminum matrix. The presence of magnesium (Mg) makes the alloy heat-treatable and can result in improved mechanical properties of the alloy with proper heat treatment process. The T6 heat treatment process is employed for strengthening of the alloy A356. This process employed by the wheel manufacturing company consists of 3 steps i) Solutionizing step - heating the alloy to a temperature of 540 °C and then holding it for 4 hours at that temperature ii) Water quench iii) Artificial aging. Holding the alloy for an extended period of time results in dissolution of Mg and Si in the α-Aluminum phase. The rapid water cooling inhibits the formation of unwanted phases and precipitation of Mg-Si particles, resulting in a non-equilibrium super saturated solid solution. Finally, in the last step of artificial aging, the

supersaturated solid solution is held at an intermediate temperature of 140 °C, for a specified time till the desired material properties are achieved.

One of the major concerns with the wide scale application of cast aluminum alloys is their reduced fatigue life when compared to forged steel.

Figure 2-1 shows a typical fatigue life curve for cast alloy A356, as published by Wang et. al. [9]. This type of graph provides important information about the fatigue properties of A356. The fatigue life curve is plotted showing stress amplitude versus cycles to failure. Figure 2-1 shows that the fatigue life is inversely proportional to stress amplitude level. At each stress amplitude level, the fatigue life is not defined by a single point but rather a scatter of points that may exhibit a difference between the lower and upper limit of up to one order in magnitude. The scatter in the fatigue life can be attributed to the type, size, position and shape of failure causing defects in the alloy [10]. A more detailed description of these factors is provided later in this chapter. Lastly, the arrow marks on the graph depict runout/ no failure, i.e. fatigue samples which did not fail by 10^7 cycles. This does not mean that these samples will never fail as cast aluminum alloys do not show any fatigue endurance limit but a limit of 10^7 cycles has been specified by ASTM standard E466 to measure the fatigue life of cast aluminum alloys, after which the test is stopped.

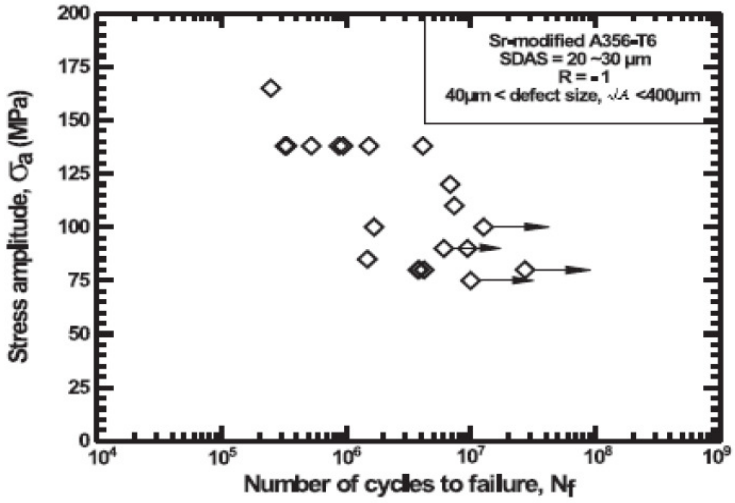

Figure 2-1. Fatigue life curve [9]

2.1.1. Micro-structural features

The main microstructural components of alloy A356 are a primary Al matrix, an Al-Si eutectic and Fe rich intermetallics. The volume fraction of the eutectic phase is dictated by the chemistry of the alloy but the size and distribution of primary dendrites and eutectic structures are controlled by the solidification time [11]. The fatigue failure of cast aluminum alloys is dominated by discontinuities like pores and oxide films. In order to analyze the effects of the micro-structural constituents on fatigue life, castings must be made with specially clean and degassed melts. Many authors such as Wang et. al. [11], Yi et. al. [8] and Campbell et. al. [12] have used the Hot Isostatic Pressing (HIP) process to reduce the size and distribution of porosity in the castings and thereby focus on the effects of microstructure.

Figure 2-2 shows the microstructure of an unmodified alloy A356 [11]. Fe-intermetallics and silicon particles are present in the eutectic phase bonded to the aluminum matrix. For slow solidification rates, the microstructure produced can be very coarse hence, strontium is added in small quantities to modify the morphology of the eutectic from large flake-like colonies as seen in Figure 2-2 to the fine fibres shown in Figure 2-3. The modification of the eutectic phase results in better fatigue and tensile properties for A356 [11]

.

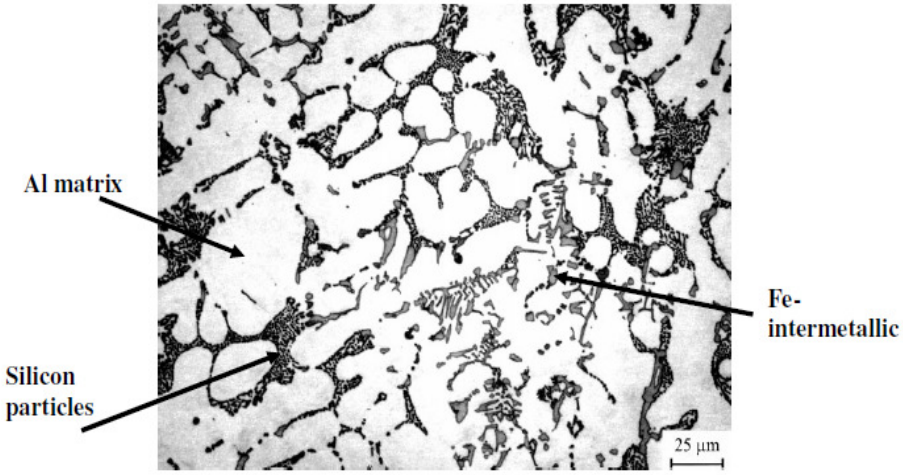

Figure 2-2. Unmodified microstructure of A356 [11]

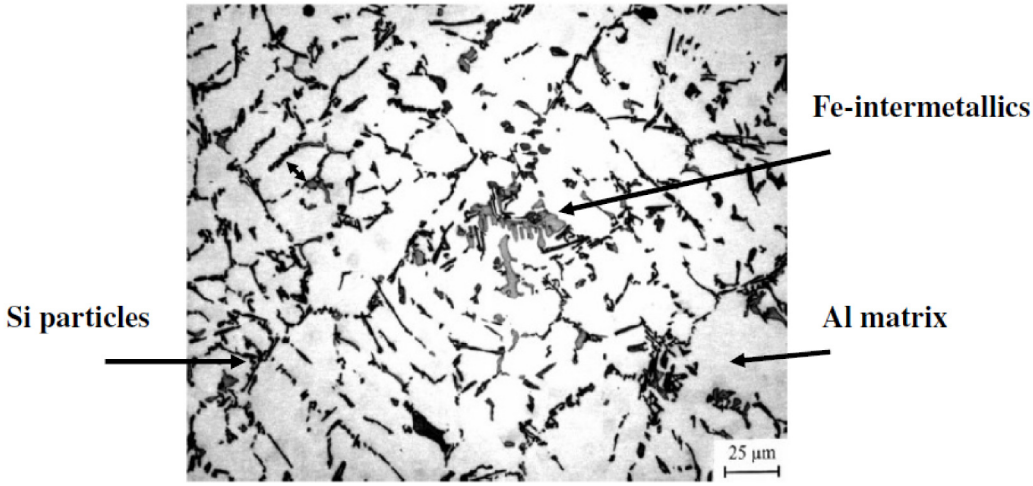

Figure 2-3. Modified microstructure of A356 [11]

2.1.1.1. Secondary dendrite arm spacing (SDAS)

Secondary dendrite arm spacing (SDAS) is a characteristic feature of cast aluminum alloys that is typically reported. It is the spacing between secondary arms of the primary aluminum dendrite which defines a grain. The dendrite size and morphology depends upon the solidification rate [9]. Cast aluminum alloys with a finer microstructure, i.e. lower SDAS, exhibit better mechanical properties like Yield strength, Ultimate tensile strength and elongation as compared to alloys with coarse dendrite structures [12]. Heat treatment, ageing and the HIPing process are known to have no effect on SDAS.

In defect free castings, i.e. castings free of pores and oxides, fatigue cracks are known to initiate in the dendritic microstructure of the alloy. Wang et. al [11] experimentally deduced that fatigue life increases with a decrease in SDAS when SDAS is less than 60µm, whereas when the SDAS is greater than 60µm, the fatigue life increases with an increase in SDAS [11]. However, no explanation was provided to support the experimental results. Figure 2-4 shows the experimental results reported by Wang. et. al. All the samples tested were HIPed to remove porosity before T6 heat treatment.

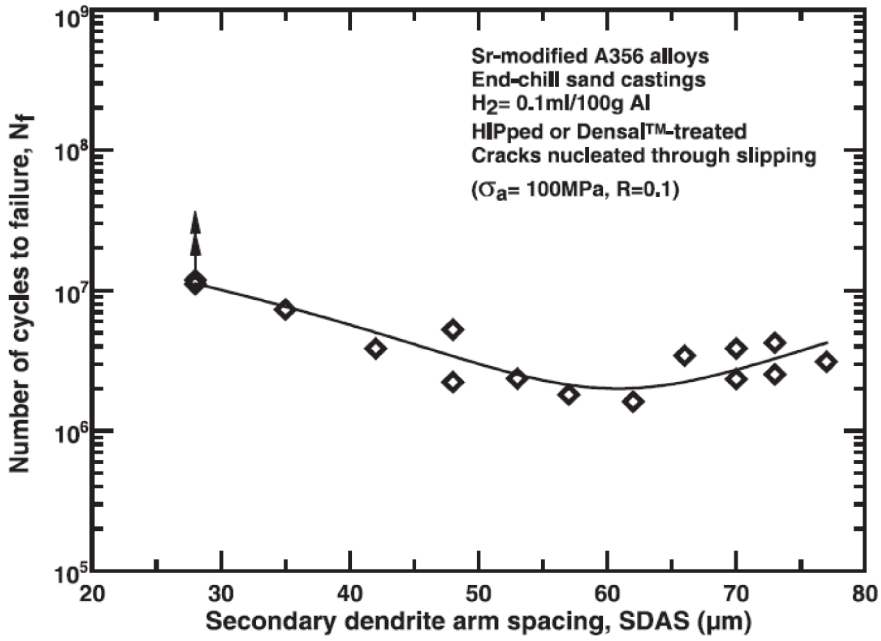

Figure 2-4. Effect of SDAS on fatigue life [11]

2.1.1.2. Silicon eutectic particles

The Si- particles in the eutectic of alloy A356 are distributed around the α-Al dendrites to form a cell pattern. This repeated cell pattern across the metallographic surface is called a micro-cell [3] or a dendrite-cell. Generally, the shapes of these micro-cells are elliptical with the minor axis length equal to the secondary dendrite arm spacing. The major axis is twice the length of the minor axis and is hardly affected by solidification time or HIPing. Longer solidification time leads to larger and more acicular Si particles [3].

As noted earlier, strontium-modification is used to produce fibrous silicon particles. The modified alloy A356 has better mechanical and fatigue properties [11]. For HIPed castings with low Fe- content, the eutectic Si particles can act as initiation sites for fatigue failure. Gall et. al. [13] investigated the effects of bonded Si- particles in the Al- matrix using finite element analysis. Their work concluded that in the absence of voids, bonded particles like eutectic Silicon can have sufficient plastic strain accumulated around them during cyclic loading to cause debonding. The debonded Si-particles result in high stress concentration and can cause fatigue crack initiation at the site.

2.1.1.3. Fe-intermetallics

Plate like Fe-rich intermetallic particles are present in the castings and their size is proportional to Fe-content, i.e. higher Fe- content leads to large plate like intermetallics whereas low Fe-content results in small needle like Fe- intermetallics in the eutectic region [14]. Fe intermetallics are observed to debond from the Al-matrix in a crack initiating micro-cell because of accumulated plastic strain. The presence of Fe-intermetallic plates can cause higher localized plastic strain as compared to Si-eutectic particles in HIPed castings because of their elongated shape. With an increase in Fe-content in the alloy, the fatigue life decreases for coarse SDAS whereas for fine to intermediate SDAS, there is no apparent effect of increased Fe- content [11].

Yi et. al. [14] observed that there exists a critical stress level below which high Fe-content reduces the observed fatigue life, this critical stress level is reported to be 130-140 MPa (see Figure 2-5). However, if the applied stress is above the critical stress level, the high Fe-content increases the fatigue life slightly [14]. The presence of high Fe-content at low

amplitude stress levels i.e. less than 130-140 MPa results in a large localized plastic strain concentration at the crack initiation site. The localized plastic strain can result in debonding of the Fe- intermetallics from the Al-matrix and then act as a crack initiation site [13]. At low amplitude stress levels, in HIPed castings, fatigue life is dominated by crack initiation life; a high Fe-content contributes to crack initiation thus reducing the number of cycles for fatigue crack initiation. On the other hand, when the applied stress levels are high, the fatigue life is dominated by the propagation phase. The presence of plate-like Fe-intermetallics particles at an angle to, or perpendicular to the propagation crack tip can provide extra resistance to crack growth, hence resulting in higher fatigue life.

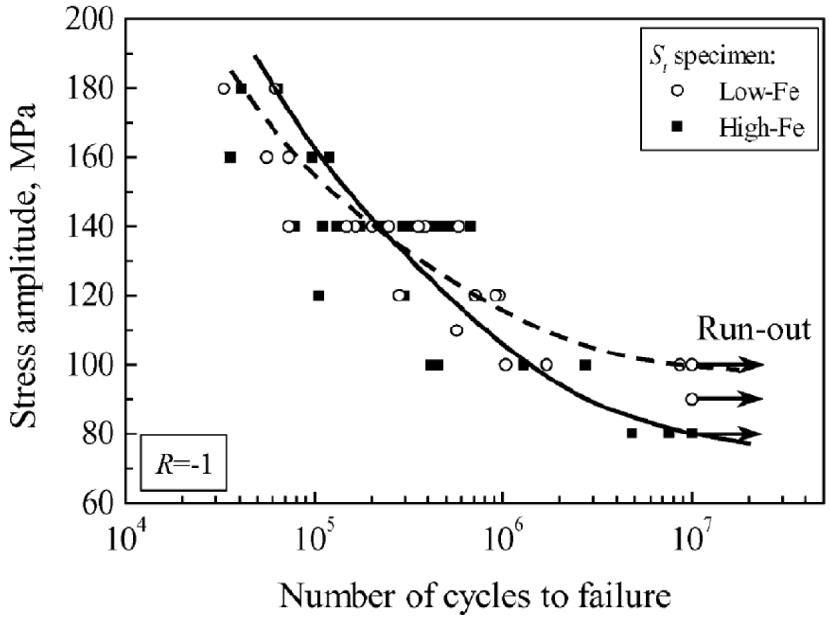

Figure 2-5. Fatigue life A356 with varying Fe-content [14]

2.1.2. Defects

Casting defects such as oxide films or pores are inevitably present in cast aluminum alloys, generally due to poor mold design, bad casting practices or turbulence [12]. Pores and oxide films are more harmful to fatigue life than any other microstructural feature. It is an ongoing debate among various authors as to which defect is more detrimental to fatigue life; pores or oxide films. On the one hand, authors Wang. et. al.[9], Couper et. al. [15], McDowell et. al. [16] believe that the pores have a more significant effect on fatigue life of cast aluminum alloys as compared to oxide films, whereas authors such as Campbell et. al. [17] and Nyahumwa et. al. [18] have the opposite opinion. It is still not clear which is the most detrimental defect and more research work is required in this area. A brief description of pores and oxide films is provided in the following sections.

2.1.2.1. Oxide films

Oxide films exist on the surface of the melt and get entrained into the melt during filling due to turbulence or poorly designed runner systems [12]. Two types of oxide films have been found to exist in cast aluminum alloys, old films and new films [12]. Old films which are formed during the melting process at the surface of the furnace or transfer ladle are generally thicker with higher levels of magnesium and oxygen [18]. These old oxide films are more likely to be flat and less convoluted than new films (see Figure 2-6). These films tend to partially bond with the Al matrix reducing the stress concentration at their edges [19].

The new oxide films are formed due to folding-in of a thin oxide film formed on the liquid surface. These are called bi-films [17]. When entrained in the melt, these films form an oxide-to-oxide (dry side-to-dry side) interface with varying amounts of air trapped between the two interfaces [18]. When viewed with a scanning electron microscope (SEM) (see Figure 2-7), they appear very thin and finely folded. These double films have no significant bond between the interfaces and can act as a crack initiation site for fatigue failure [12].

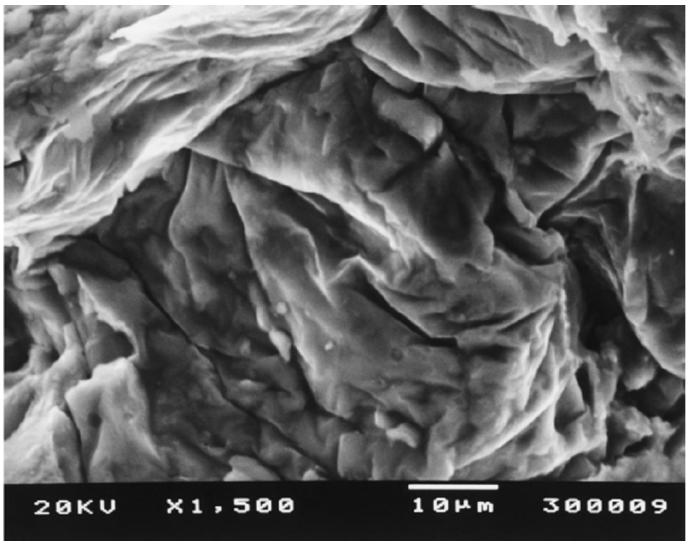

Figure 2-6. Old oxide film [18]

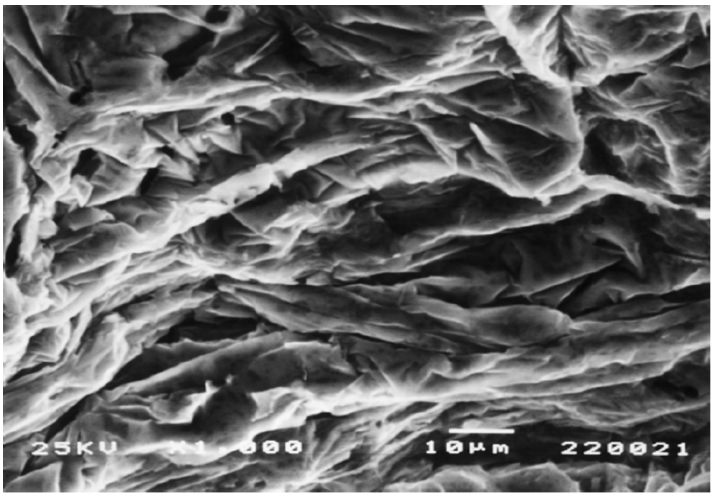

Figure 2-7. New oxide film [18]

2.1.2.2. Micro-porosity

Figure 2-8 shows a typical pore in an alloy A356 produced during the casting process. The size and distribution of pores is highly variable depending on casting process parameters such as local cooling rate and hydrogen content [3]. Pores associated with dissolved gases are generally round in shape and occur as individual bubbles whereas shrinkage porosity occurs in clusters of irregularly shaped pores [10]. The size of pores in the alloy A356 varies from ten to hundreds of microns [2]. Various casting processes give rise to different pore densities; abundant porosity has been seen in high pressure die castings whereas squeeze castings can be essentially pore free if the melt is handled with care. Semi-solid castings can minimize defects but due to complex shapes of final products, ideal conditions are not reached and defects tend to occur [10].

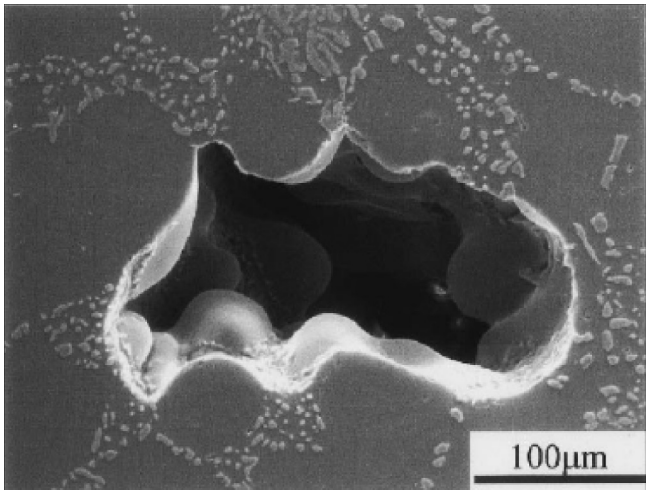

Figure 2-8. A typical cast A356 pore [8]

The eutectic regions are the favored location for porosity [2]. The presence of eutectic silicon and intermetallic particles around pores help in the formation of cracks [9]. Yi. et. al. [8] used finite element modeling techniques to verify that a high stress concentration is developed at the roots of pores in between the secondary dendrite arms which leads to fatigue crack formation. Figure 2-9 shows the normalized stress field around the concave

tips of the pore. Here, σ refers to the localized stress and σ^{∞} refers to the far-field amplitude stress applied to the sample. Figure 2-9 shows that the normalized stress ratio can be as high as 6. Thus, even if the far-field amplitude stress applied is below the yield strength, the localized stress at the pore tip may be much higher than the yield strength due to the stress concentration effect of the pore [8]. Therefore, it is predicted that a fatigue crack can readily initiate in the early stages of loading and fatigue life when pores are present is dominated by crack propagation [9].

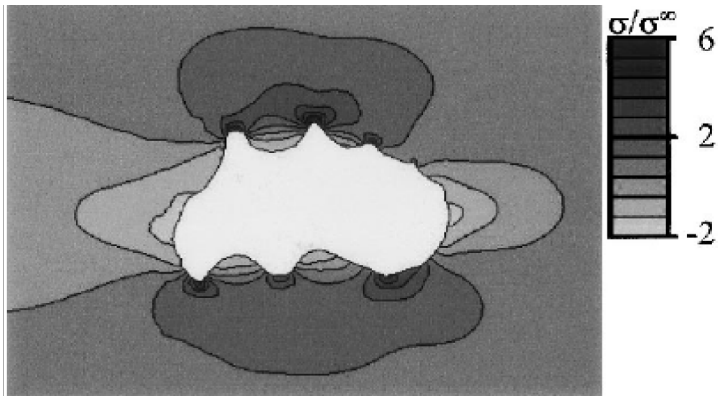

Figure 2-9. Finite element generated stress field around a pore [8]

2.2. Fatigue modeling

One of the first attempts to quantify fatigue life was made by Paris in 1960. According to the Paris law, the rate of crack growth is proportional to the stress intensity factor range at the crack tip. Equation (2-1) shows the Paris law,

$$\frac{da}{dN} = C(\Delta K)^m \tag{2-1}$$

where *da/dN* represents crack growth rate, a is the crack size, *N* is the number of loading cycles, *C* and *m* are material constants and ΔK is the stress intensity factor range at the crack. In cast aluminum alloys, large pores present at or near the specimen surface are predominantly the cause of fatigue failure [20]. The number of cycles required to initiate a crack from a defect is called fatigue initiation life. For large pores present at or near the surface of a specimen, fatigue initiation life is almost negligible [19][21]. As a result, a fracture mechanics or crack growth type approach, as in Equation (2-1) can be used for predicting fatigue life of cast aluminum alloys.

Many authors [15][22] have tried to model the fatigue life of cast aluminum alloys using a modified Paris law where ΔK_{eff} is calculated considering the closure effect. The modified Paris law is shown in Equation (2-2)

$$\frac{da}{dN} = C(\Delta K_{eff})^m \tag{2-2}$$

where ΔK_{eff} is the closure corrected effective stress intensity range at the crack initiating defect.

Couper et. al. [15] integrated Equation (2-2) from an initial crack size (a_i) to a final crack size (a_f) and estimated ΔK_{eff} using the closure effect. They found that predictions for fatigue life were in good agreement with their experiments. The initial crack size (a_i) was

determined from the pore responsible for the fatigue failure. Skallerud et. al [22] in a similar approach integrated Equation (2-2) and were able to predict fatigue life in good agreement with experiments. Fatigue life prediction by both the authors [15] and [22] were in good agreement with the experimental data but both had a similar trend of over estimating the fatigue life.

It was later realized that the Paris law is only applicable to long cracks [20] i.e. cracks greater in size than 2mm. In cast aluminum alloys, an appreciable amount of time in fatigue crack growth is spent in the small crack growth regime. A small crack is generally identified as a crack less than 1 to 2mm in size. It has been shown that small cracks grow faster and at smaller ΔK than long cracks [20]. Hence, small crack growth should be taken into consideration while modeling fatigue behavior. Thus, Linear Elastic Fracture Mechanics (LEFM) based on long crack growth theory is not suitable for accurately describing the full fatigue life behavior of cast aluminum alloys.

Other authors have also tried to model small crack growth using LEFM and introducing different definitions of ΔK based on the crack closure effect, but in general the equations have become more complicated and their use has been limited [20].

To overcome these deficiencies, Nisitani et. al. [23] proposed the fatigue crack growth relation (see equation (2-3)) independent of stress intensity factor range. In this equation, they were able to successfully relate fatigue crack growth to crack size.

$$\frac{da}{dN} = C\left(\frac{\sigma_a}{\sigma_y}\right)^n a \tag{2-3}$$

where σ_a and σ_y are applied amplitude stress and yield strength, respectively. C and n are material constants determined empirically. Caton et. al. [20] acknowledged that in equation (2-3), the term within the parenthesis raised to power n is dimensionless and the driving power for crack growth rate is in units of length but equation (2-3) neglected the effects of local heterogeneities on crack growth. Caton et. al. [20] proposed equation (2-4)

$$\frac{da}{dN} = C\left(\varepsilon_{\max}\frac{\sigma_a}{\sigma_y}\right)^n a \tag{2-4}$$

where ε_{max} is the maximum total strain achieved during the loading cycle. Yi et. al. [8] expanded and integrated the equation (2-4) from an initial crack size (a_0) to a final crack size (a_f) determined by fracture toughness to give an expression for fatigue propagation life (N_p):

$$N_p = C_1\left(\varepsilon_{\max}\frac{\sigma_a}{\sigma_y}\right)^{-st}\left(a_0^{-t+1} - a_f^{-t+1}\right) \tag{2-5}$$

Equation (2-5) was successfully used to predict fatigue propagation life when the initiating defects are pores in non-HIPed castings and dendrite-cell in HIPed castings [8] but total fatigue life for cast aluminum alloys may include fatigue initiation life, as shown in equation (2-6). Whenever, a large pore is present at or near the specimen surface, the fatigue crack initiation life is almost negligible and total fatigue life can be considered equal to crack propagation life [21]. In other fatigue crack initiation mechanisms i.e. fatigue cracks initiating from oxide films, dendrites, eutectic particles, fatigue initiation life play an important role in the total fatigue life of the specimen. For large pores present deep in the specimen and low far field stress levels, initiation life can account for a large part of the total fatigue life. In this case, the total fatigue life may be defined as:

$$N_f = N_i + N_p \tag{2-6}$$

where N_f, N_i and N_p represent total, initiation and propagation fatigue life, respectively.

Fatigue crack initiation life is defined as the number of cycles required to develop a fatigue crack from a pore or a micro-cell. Yi. et. al. [3] proposed a fatigue initiation life relation based on the total accumulated equivalent plastic strain (ε_{eq}^{p}) at the failure causing dendrite cell, see equation (2-7).

$$N_i = \frac{C_0}{\lambda_2}\left[\frac{1}{\sigma_a}\left(k_0 + \frac{\alpha}{\sqrt{\lambda_2}}\right)\right]^{\frac{2}{\beta}} \tag{2-7}$$

where, λ_2 refers to the secondary dendrite arm length, σ_a is the amplitude stress, C_0, k_0, α and β are material constants.

Yi et. al. [8] combined equations (2-5) and (2-7) and gave a generalized fatigue life model for failure emanating from either eutectic particles (Si particles or Fe-intermetallics), SDAS or pores as shown in Equation (2-8).

$$N_f = N_i + N_p = \frac{C_0}{\lambda_2}\left[\frac{1}{\sigma_a}\left(k_0 + \frac{\alpha}{\sqrt{\lambda_2}}\right)\right]^{\frac{2}{\beta}} + C_1\left(\varepsilon_{\max}\frac{\sigma_a}{\sigma_y}\right)^{-st}\left(a_0^{-t+1} - a_f^{-t+1}\right) \tag{2-8}$$

Figure 2-10 shows a comparison between the fatigue life predicted by models (2-5), (2-7) and (2-8) with the experimental results for non-HIPed cast A356 samples [3]. It can be clearly seen that for non- HIPed castings, where pores act as the failure causing defects, the total fatigue life is dominated by the propagation life for $\sigma_a > 80$ MPa whereas initiation life dominates at very low stress levels. It should also be noted that the fatigue life prediction models aptly match with the experimental results.

Figure 2-11 shows a similar comparison between the empirical models (2-5), (2-7) and (2-8) with the experimental results for HIPed cast alloy A356 [3]. For the HIPed castings, it was observed that Si-particles were the failure initiation sites [3]. It can be inferred from Figure 2-11 that for HIPed castings, the fatigue life is dominated by the crack initiation life for $\sigma_a < 140$ MPa.

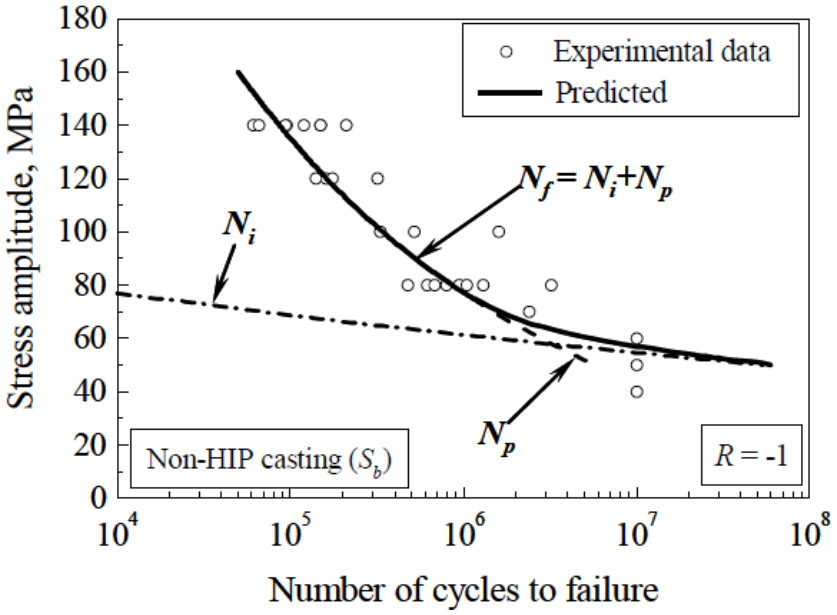

Figure 2-10. Fatigue life comparison for non-HIPed A356 [3]

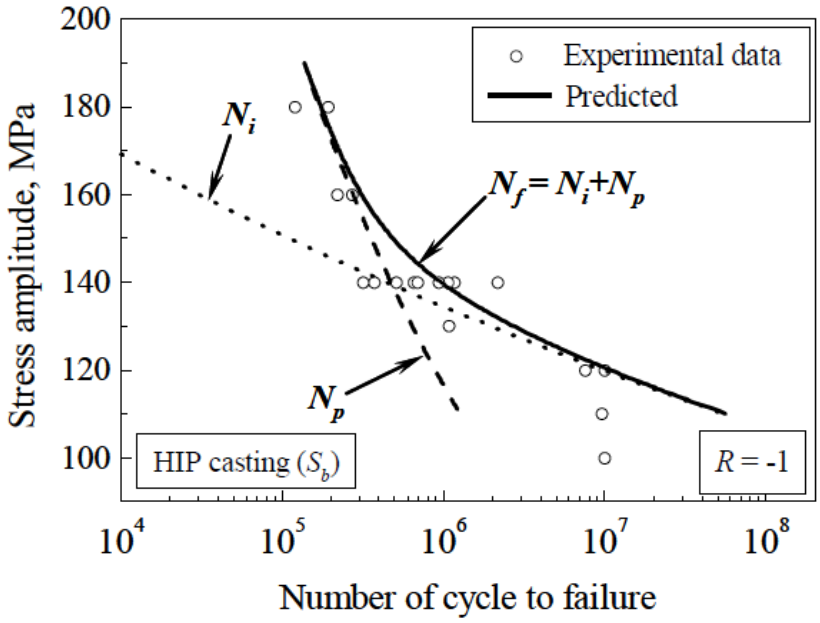

Figure 2-11. Fatigue life comparison for HIPed A356 [3]

2.3. Fatigue life of pre-strained aluminum alloys

As explained in the Section 1.2, a leading wheel manufacturing company is interested in determining the radial fatigue of plastically deformed cast A356 aluminum wheels. Section 2.1 introduced the prominent work done in the field of fatigue life of cast aluminum alloys. This section will review the effects of plastic deformation on fatigue life.

One of the earliest attempts to identify the effects of pre-straining of Al alloys on their fatigue life was reported by A. F. Getman and Yu. K. Shtovba in 1982 [24]. They tried to investigate the effects of plastic deformation on forged Al alloys immediately after hardening. The specimens were aged artificially after deformation. After experimenting with different degrees of pre-strains, they concluded that plastic deformation up to 2% does not have any significant effect on the fatigue life of forged Al alloys. Plastic deformation of more than 2% leads to a decrease in fatigue life [24].

In a recent work, K. S. Al-Rubaie et. al. [25] and [26], showed the effects of pre-strain on fatigue life of forged aluminum alloys 7475- T7351 and 7050-T7451. They showed that with an increase in the level of pre-strain, the fatigue life decreased for the aluminum alloys.

The fatigue life of pre-strained forged aluminum alloys is found to decrease with an increase in the level of pre-strain. Significant work has been done on understanding the fatigue life characteristics of pre-strained forged aluminum alloys [24-26]. The effects of pre-straining on the fatigue life of cast aluminum alloys is an area of research that has received little attention and to the best of the author's knowledge there are no publications on it.

2.4. Wheel testing

Wheels are considered a safety related component. Consequently, their fatigue performance under various loading conditions is an important issue. The current emphasis on making lighter wheels by either using cast aluminum alloys or making thinner gauge sections has increased the amount of study in this area. Wheels made of cast aluminum alloys typically have improved aesthetic designs that are attractive to consumers. As the complexity of wheel designs increases, it is difficult to estimate the fatigue strength of the wheels using analytical methods [27]. Component-level fatigue tests are full-scale experiments performed by industry, either at a testing facility or at a wheel-manufacturing foundry, to assess the fatigue life or durability of a wheel. Two fatigue tests performed as part of typical quality assurance testing are: 1) the radial fatigue test and 2) cornering test (SAE J328a) [27]. Based on the results of these fatigue tests, the wheel designs can be modified to improve strength and fatigue life. A brief description to the tests will be provided in the following section.

2.4.1. Radial fatigue test

A typical radial fatigue test setup according to standard (SAE J328a) is shown in the Figure 2-12. In this test, a test wheel and tire are mounted on a hub by lug nuts at a suitable torque and placed in contact with a rotating drum. The drum axis is parallel to the axis of the test wheel. A hydraulic ram loads the test wheel and tire by pushing it normal to the surface of drum and in-line radially with the center of the test wheel and the drum. The drum is rotated at a simulated road speed based on the size of the wheel. This test simulates typical car operation where the weight of a car is balanced with a vertical reaction force from the road through the tires. To accelerate fatigue testing and enhance the effectiveness of the radial fatigue test, the entire vehicle weight is applied to a single tire resulting in radial compressive loading. While the test is running, the radial load at each point on the wheel is cyclically varying with the rotation of the wheel leading to possible fatigue failure.

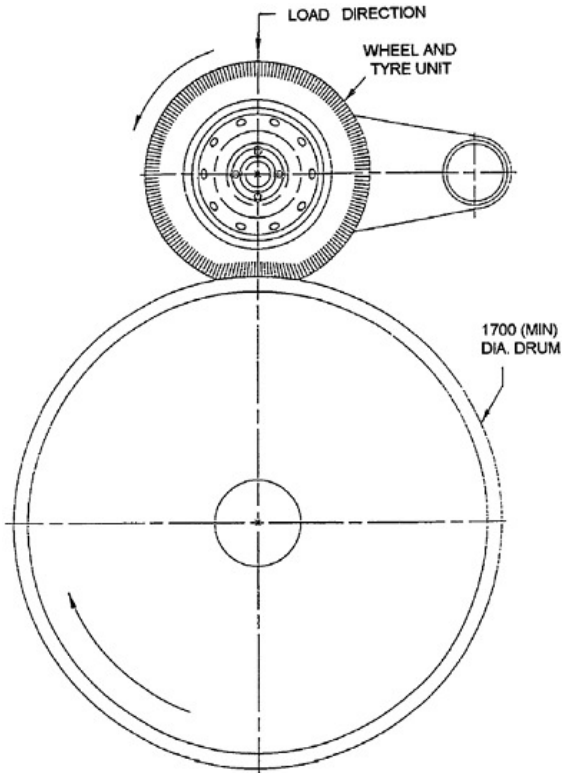

Figure 2-12. Radial fatigue test setup [27]

According to SAE J 328a standards, a wheel should maintain its structural integrity for a minimum 4 x 10^6 cycles under the radial load, given by equation (2-9).

$$Q = S \times F \tag{2-9}$$

where Q is the radial load applied on the wheel, S is the acceleration test factor according to SAE J328a standards (S=2.2) and F is the maximum possible load on the wheel (i.e. the full weight of the vehicle).

2.4.2. Cornering test

The cornering fatigue test (SAE J328a) is a durability test performed on wheels to assess their fatigue characteristics under cornering conditions. In this test, the dynamic forces acting on the wheel during the cornering of an automobile on the road are simulated by applying a varying or constant load to a load arm attached to a rotating wheel, as shown in Figure 2-13.

In this test, the inboard rim flange is clamped securely to a rotating table. The hub of the wheel is attached to a rigid shaft running through the centre. The test load is applied to the shaft as shown in Figure 2-13. A cyclic bending load is generated by rotating the table.

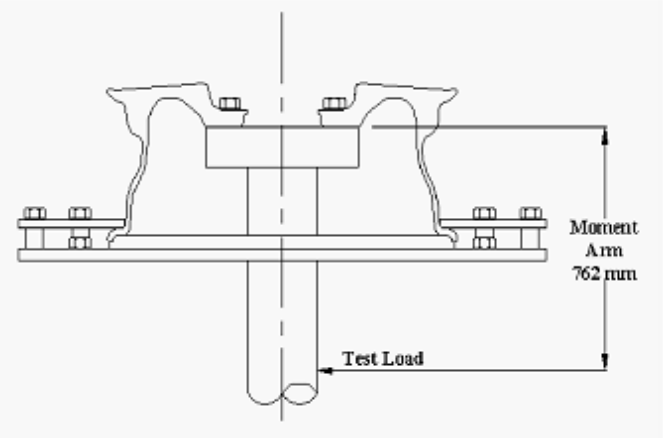

Figure 2-13. Cornering fatigue test setup [28]

2.5. Radial fatigue modeling

The rim indentation test for wheels is followed by the radial fatigue test. In order to predict the fatigue life of deformed wheels under radial load, the characterization of the stress state of the wheel under radial load is required. Hence, the effect of radial load on the wheel is discussed in this section.

The weight of a vehicle is supported on the four wheels of the automobile. The vertical reaction forces exerted by the road on the tires balance the total weight of the automobile. The reaction forces compress the tire, which in turn transmits the forces to the wheel. When the tire is compressed, the contact between the road and the tire is a flat surface called the contact patch. The contact patch is measured in terms of the angle swept by the contact patch length at the centre of the wheel, shown as θ in Figure 2-14. The value of contact patch (θ) depends on the tire pressure, vehicle weight and tire geometry.

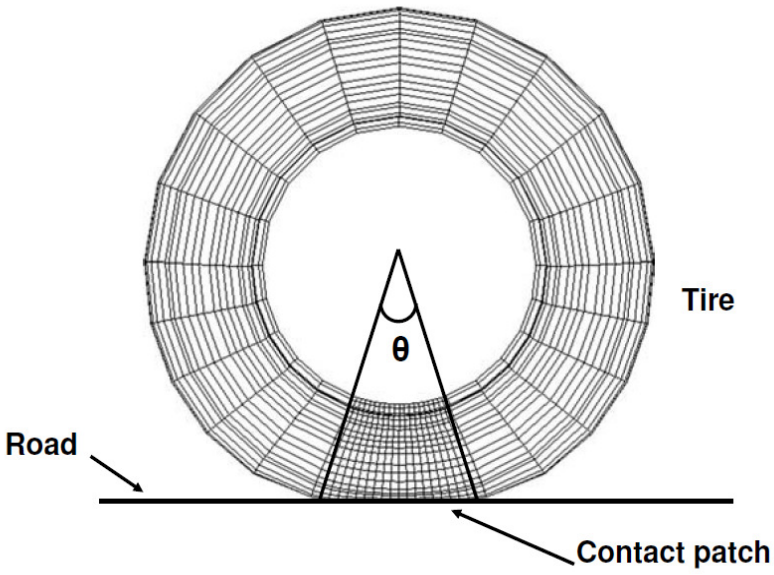

Figure 2-14. Tire under a vertical load [31]

The radial load on the wheel can be estimated as a pressure load applied to the bead area. Stearns et. al. [29] suggested the contact patch angle to be 80° and hence to quantify the effect of the radial load on the wheel, a pressure load should be applied for the corresponding 80° degrees of the bead area on the wheel. Ramamurthy et. al. [27] demonstrated through experiments and a finite element model that the effect of radial load on the wheel is not limited to the corresponding angle on the wheel but should span the entire bottom half of the wheel i.e. pressure should be applied to 180° of the bead area.

Stearns et. al. [29] investigated the effect of the radial load on the wheel. The contact region between the tire and the wheel is the bead seats area as shown in Figure 2-15. They assumed the entire radial load was applied on the bead area of the wheel. They experimentally deduced that the radial load applied on the wheel by the tire follows a cosine curve i.e. the load is maximum at the centre of contact patch and decreases to zero following a cosine curve, as shown in Figure 2-16.

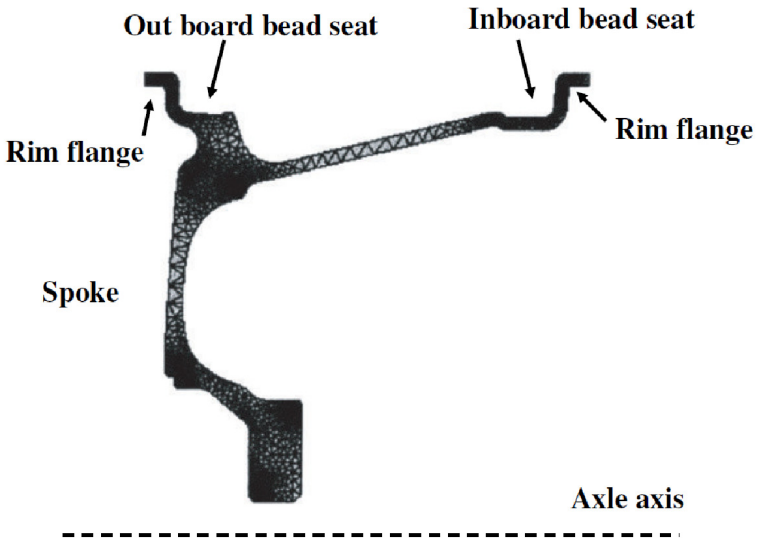

Figure 2-15. Axisymmetric model of wheel [29]

The variable pressure load W_r can be estimated as shown in equation (2-10).

$$W_r = W_0 \times \cos\left(\frac{\pi}{2} \times \frac{\theta}{\theta_0}\right) \tag{2-10}$$

where W_r is the pressure load on the bead area at a circumferential angle θ from the centre of the patch, W_0 is the maximum pressure load at the centre of contact patch, θ is the circumferential angle of the wheel ($-\theta_0 < \theta < \theta_0$) and θ_0 is half of the angle swept by the contact patch at the centre. Distributed pressure load (W_r) can be integrated over the bead area to give total radial load (W), as shown in equation (2-11).

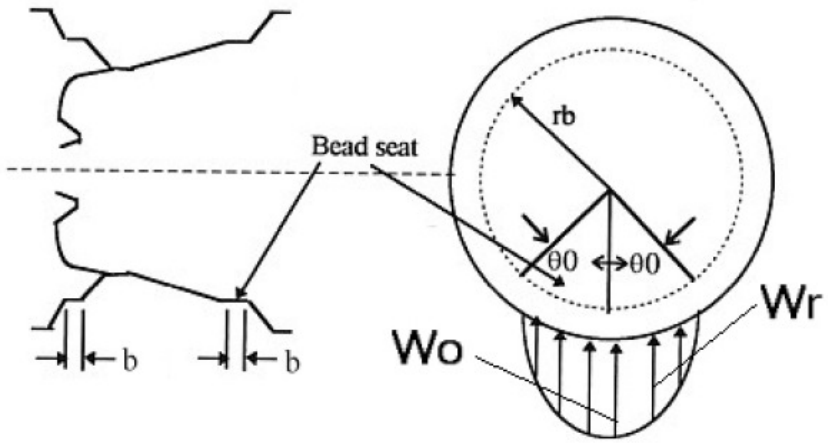

Figure 2-16. Radial load schematic at the bead area [29]

$$W = b\int_{-\theta_0}^{\theta_0} W_r \times r_b d\theta \tag{2-11}$$

where r_b is the bead radius and b is the bead width. Equation (2-10) can be substituted in to equation (2-11) to calculate the maximum distributed pressure load (W_0) at the centre of the contact patch, shown in equation (2-12).

$$W_0 = \frac{W \times \pi}{b \times r_b \times 4 \times \theta_0} \tag{2-12}$$

Once, W_0 has been determined, equation(2-10) can be used to calculate the pressure load at any circumferential location.

This same approach has been used in this research project.

3 Scope and Objectives

3.1. Scope of research work

This research work aims to develop finite element models of the rim indentation and the radial fatigue tests for aluminum alloy automotive wheels. These models may be used as design tools for predicting the fatigue life of wheels early in the design stage in an attempt to reduce the wheel development time. In order to predict the fatigue life of wheels following rim indentation, a numerical model of the fatigue life for pre-strained cast aluminum alloys is required which relates the fatigue life to the level of pre-strain and stress state in the wheel. Thus, a sub-section of this research project is to develop an empirical relation to quantify the effects of initial plastic strain on the fatigue life of A356-T6 alloy.

Figure 3-1. shows a flowchart of the work completed during the course of this research. Industrial-scale rim indentation and radial fatigue tests were done on cast alloy A356 wheels to obtain data required to model these industrial tests on a finite element platform.

The rim indentation test was performed by deforming the inboard rim flange of the wheel with a static load. The amount of plastic deformation sustained by the wheel is a measure of the quality of rim design. Rim indentation is a contact modeling problem between the wheel and the platen. This non-linear problem required an iterative solution technique. The commercial finite element software package ABAQUS™ has been employed for this work as it is well suited for this type of mechanical problem.

The rim indentation test is followed by radial fatigue tests on the deformed wheels. Modeling radial fatigue required a solution technique which is capable of reproducing the loading conditions in the radial fatigue test to estimate the stress state of the wheel. The

complex geometry of the wheel makes this problem unsolvable with analytical solution techniques. Hence, ABAQUS was used to model the radial fatigue test.

Laboratory-scale experiments were performed to determine the material characteristics of A356-T6 alloy used in the wheels. Young's modulus, yield strength, flow strength and plastic strain for alloy A356 were determined by tensile tests.

Laboratory-scale experiments were also performed to characterize the fatigue behavior of A356 following different amounts of pre-strain (plastic strain). The data was used to develop an empirical relationship between fatigue life and initial plastic strain. The samples for the fatigue test were taken from the same type of wheels used in industrial tests. The amount of pre-strain applied to the fatigue samples was estimated from the rim indentation model for a plastically deformed wheel.

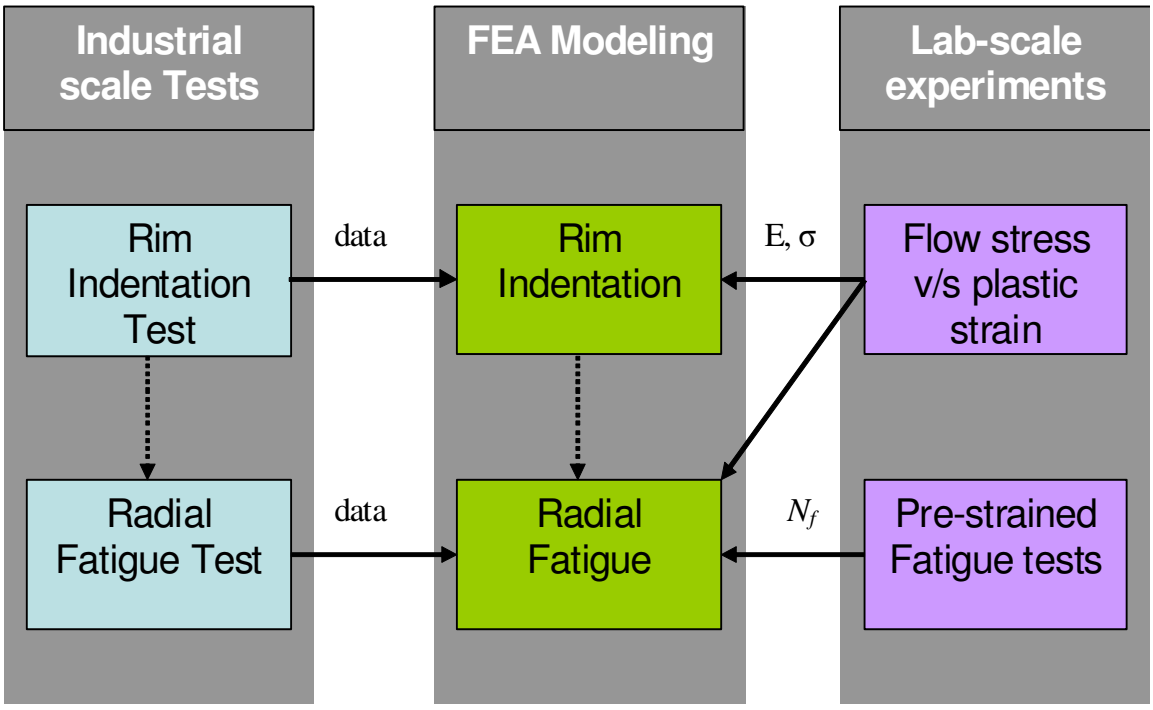

Figure 3-1. Research methodology

Finally, models of the quench process [1], rim indentation and radial fatigue testing were combined with the empirical fatigue life equation to predict the radial fatigue life of a rim indented wheel.

3.2. Objectives

The objectives of this research work are:

1) To develop and validate finite element models of the rim indentation and radial fatigue tests for aluminum alloy automotive wheels.

2) To develop an empirical relationship between fatigue life, level of pre-strain, and applied stress amplitude for cast aluminum alloys.

3) To combine the results of the rim indentation and radial fatigue models with the developed fatigue life equation to predict the fatigue life of a wheel.

4 Experimental Work

Experimental work was conducted during this project to provide data necessary to formulate and validate the models. This test work included both laboratory testing and industrial scale component testing. The testing completed for this project and the results will be presented in this chapter. Laboratory scale experiments were performed to characterize the constitutive behavior of the A356 aluminum alloy of the wheels and to develop a fatigue life equation for pre-strained cast aluminium alloys. Industrial tests were performed to provide the data necessary to validate the finite element models of the rim indentation test and the post-indentation radial fatigue test.

4.1. Industrial scale experiments

Industrial scale experiments were performed in collaboration with a North American wheel manufacturing company at their facility in British Columbia, Canada. The following industrial experiments were performed: i) Rim indentation testing on finished wheels, ii) Radial fatigue testing on a finished wheel

4.1.1. Rim indentation test

The rim indentation test is a new quality assurance test added by the wheel manufacturing company as part of their quality control program. In this test, a wheel is permanently deformed under a static load. The amount of load applied depends on the material and geometry of the wheel. The permanent deformation sustained by the wheel is used as a measure of the quality of wheel design.

4.1.1.1. Test setup

A dual column Sintech 20/G universal testing machine was used to deform the wheel. The rim indentation test setup on this machine is shown in Figure 4-1. A custom designed fixture was specified by the company to locate the wheel under the cross-head. A cylindrical platen was mounted in the cross-head. During a test, the wheel is aligned with the inboard rim flange placed directly under the platen. An optical sensor, mounted on the test machine, measured the coordinates of the cross-head and a load cell (20,000 lbf or 88 kN) was used to measure the load applied by the platen. The position of the cross-head and the load applied by the platen was monitored by a computer. The data acquisition software also routed the signal to stop the test, if either the load or the displacement of the cross-head exceeded their pre-assigned limits.

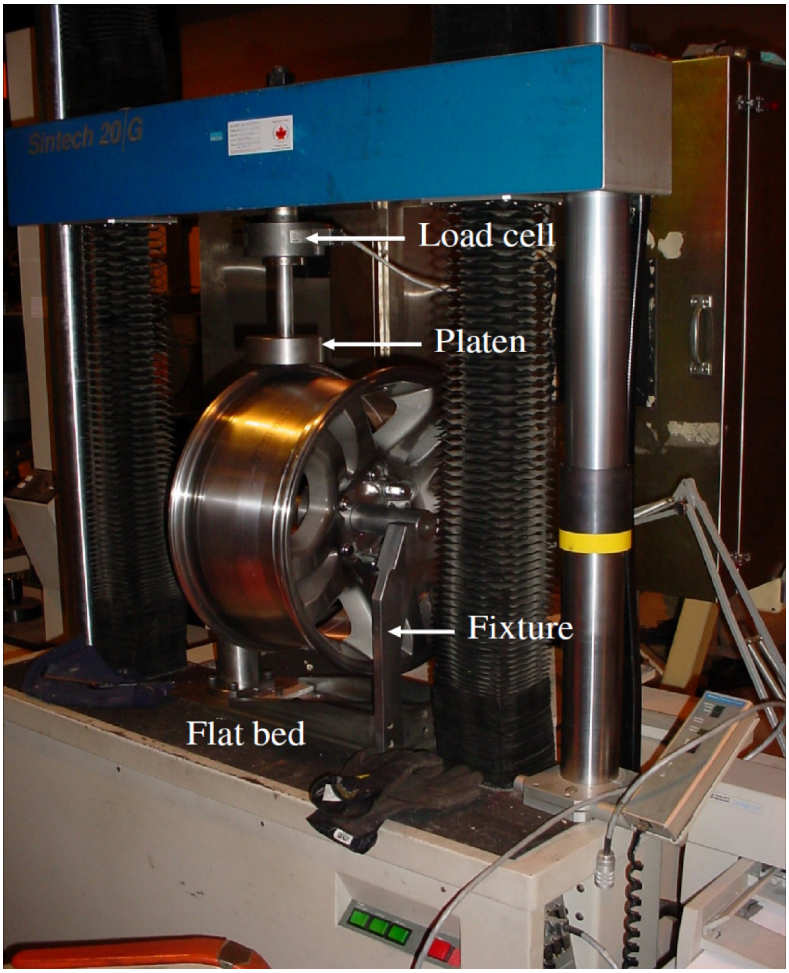

Figure 4-1. Sintech universal test machine

At the start of a test, the platen is placed just above the rim of the wheel. Testing is conducted by applying a pre-determined load with the platen moving at 0.1 mm/s. The wheel is unloaded and the permanent deformation is measured. If the deformation is less than 3 mm, the wheel has passed the test.

4.1.1.2. Test results

Two rim indentation tests were performed at Powertech, a commercial testing facility in Surrey, BC. As per the wheel manufacturing specifications, a maximum load of 20.5 kN was applied in the tests.

The load versus displacement curves measured during the rim indentation tests for the two wheels are shown in Figure 4-2. The load increases from zero at the start of the test when the platen contacts the inboard rim flange. Displacement increases with increasing load until the peak load is reached and the wheel is unloaded. The amount of deformation in the wheel is equal to the displacement of the platen and the permanent deformation is determined as the displacement offset at zero load after unloading.

In the rim indentation test graphs, shown in Figure 4-2, both wheels were subjected to a maximum load of 20.5 kN. The peak displacement of wheel #1 under load was 8.87 mm with 1.89 mm permanent displacement whereas wheel #2 deformed 8.32 mm with 1.4 mm permanent deformation. The permanent displacement sustained by both the wheels was within the acceptable limit of 3 mm as outlined by the wheel manufacturing company. Although, care was taken to ensure the same test conditions for both the wheels but the difference in the displacements of the wheels is very apparent. The discrepancies observed may be attributed to variations in the experimental setup such as orientation of the wheel and / or variations in the wheel manufacturing process. Additional testing would be necessary to characterize the extent of the variability and isolate the specific cause. However, these results provided data suitable for validating a finite element model of the rim indentation test.

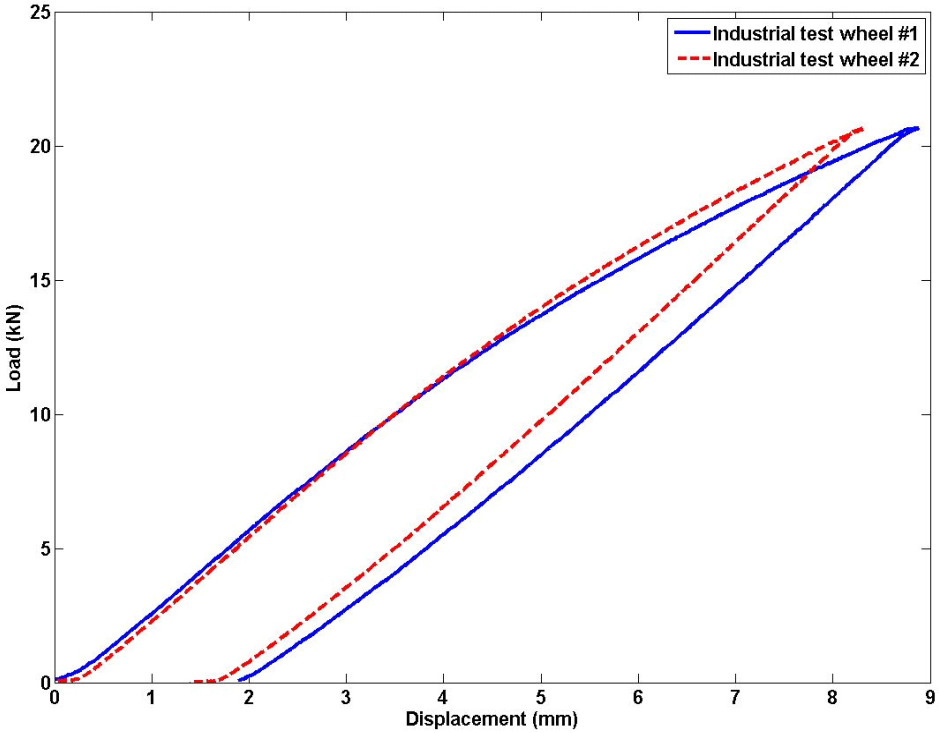

Figure 4-2. Rim indentation graphs

4.1.2. Radial fatigue test

The radial fatigue test is an SAE standard test (SAE J328a) used to assess fatigue life of wheels subjected to a radial load. It was mentioned in the literature review that radial fatigue is one of the durability tests each wheel design has to pass before being approved for full scale production. Wheel designs that do not satisfy the radial fatigue life criterion (see Section 2.4.1) are modified based on test results.

The relevance of the radial fatigue test in this research project is that as part of the new quality assessment testing in the wheel manufacturing company, wheels must satisfy a radial fatigue criterion following rim indentation testing. Radial fatigue tests were performed on wheels to systematically measure strain at a variety of locations under different loading conditions on the wheel to collect data for verifying the radial fatigue test model.

4.1.2.1. Test preparation

The strain experienced by a wheel during the radial fatigue test was characterized using strain gauges. The locations of the strain gauges were chosen using the following criteria: i) space available for mounting the gauges, ii) the surface was relatively flat and iii) the location was expected to experience significant strain. A preliminary version of the radial fatigue test model that will be described in the next chapter was used to evaluate locations based on the third criterion. Based on the previous criteria, the six locations shown in Figure 4-3 were selected. A standardized procedure was used according to the strain gauge manufacturer's specifications to mount the strain gauges. The strain gauges were mounted by the quality control personnel from the wheel manufacturing company. Three strain gauges were mounted at each location. The strain gauges used in the experiments were manufactured by Kyowa Sensor System Solutions. The specifications of the strain gauges are provided in Table 4-1. Strain gauges 1 to 12 were of type 1 whereas gauges 13 to 18 were of type 2. As these strain gauges were readily available with the wheel manufacturing company, rosettes were not purchased. The orientation of the strain gauges was such that all strain components on the plane could be calculated. Pictures of the installed gauges and their orientations are shown in refer Figure 4-4, 4-5 and 4-6. Figure 4-5 shows gauges 13, 14 and 15, the angle between the longitudinal axes of gauges 13 and 14 as well as gauges

13 and 15 is same 135° such that gauges are in a 45° rosette formation. Same orientation was used at other gauge locations. The gauges used had self compensation temperature range from 10 to 100 °C.

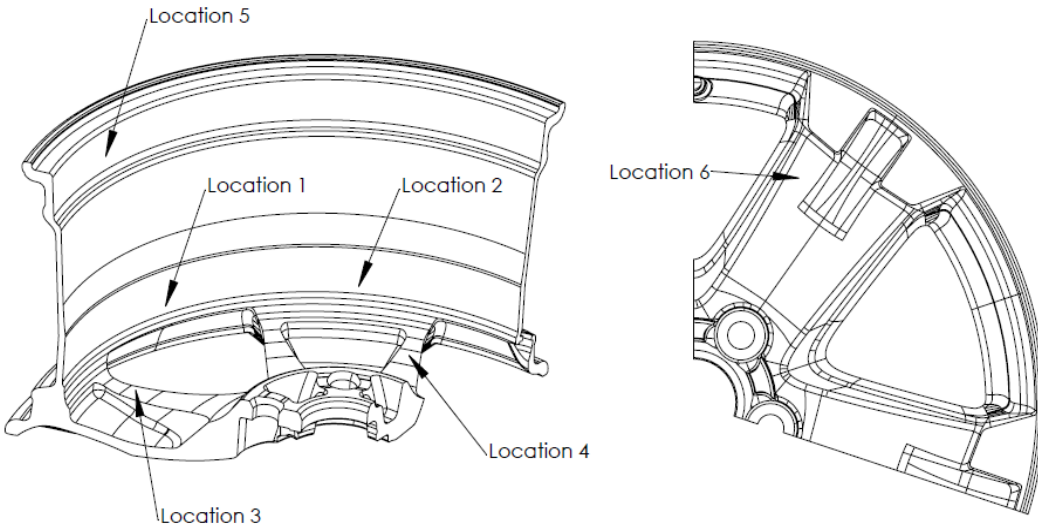

Figure 4-3. Strain gauge locations

Table 4-1. Gauge specifications

	Type 1	Type 2
Gage Length(mm)	3	1
Resistance (ohms)	119.6+/- 0.4	119.6+/- 0.4
Gage Factor	2.13 +/- 1%	2.17 +/- 1%
Thermal expansion(/°C)	23.4	23.4
Transverse sensitivity	0.5	2.3

Figure 4-4. Strain gauges at locations 1 to 4

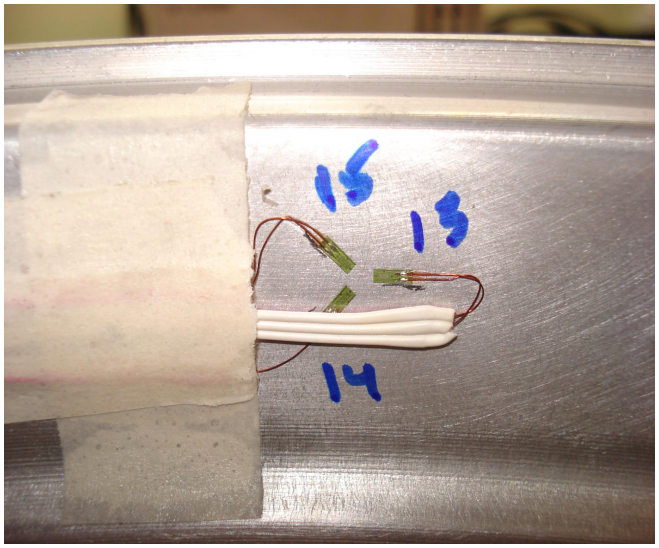

Figure 4-5. Strain gauges at location 5, inboard rim

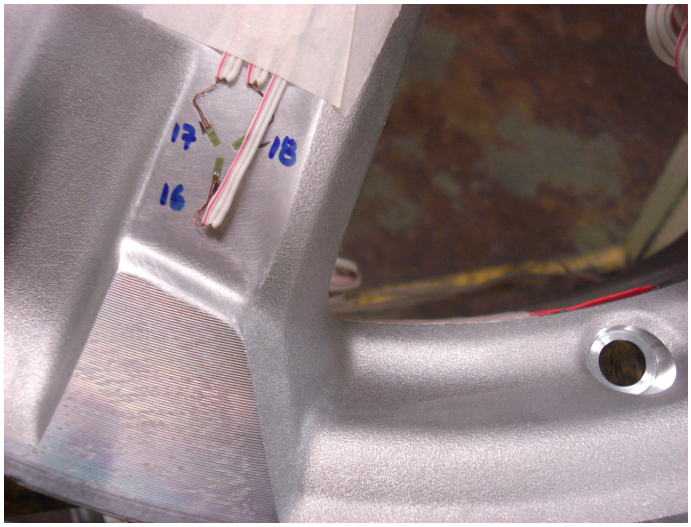

Figure 4-6. Strain gauges at location 6, spoke

4.1.2.2. Test procedure

With the strain gauges mounted on the wheel, strain measurements were taken under the following four conditions:

1) Base level:

The first set of strain measurements were taken on a fully finished wheel without the tire. One might expect the strain readings to be zero as no load had been applied to the wheel but generally they were not. The gauges tend to develop an initial strain due to a number of reasons like installation, rough handing, temperature, etc. This is known as zero error or base level strain. This base level strain was measured for all the strain gauges.

Strain measurements for each of the 18 gauges at conditions 2, 3 and 4 were zero error corrected by subtracting the base level strain from them.

2) Tire mounted on the wheel but not inflated:

Next, a tire was mounted on the wheel but not inflated. A second set of strain readings were recorded for this condition.

3) Tire inflated to test conditions i.e. 60 psi:

The tire was inflated to the test pressure of 60psi and a third set of strain readings were recorded.

4) Wheel rotated under radial fatigue test conditions:

Finally, the wheel was mounted on the radial fatigue test setup, shown in Figure 4-7. The wheel manufacturing company's standard for their radial fatigue testing of the wheel model used for this investigation were:

Tire pressure = 60 psi

Radial Load = 1560 kgf

A non-standard rotational speed of 3 km/hr was selected for this test. This speed was selected because it was slow enough to provide enough strain data for almost 2 complete rotations within the limitations of the DAQ system. A total of 4000 data points were collected for each strain gauge.

The strain measurements from the Radial Fatigue Test were used to validate the radial fatigue model which was developed in ABAQUS.

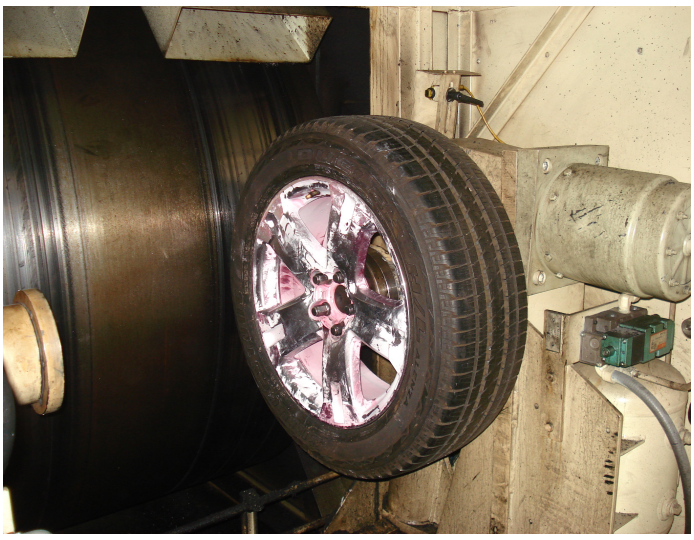

Figure 4-7. Radial fatigue test setup

4.1.2.3. Test results

Strain measurements for one strain gauge from each of the six locations, i.e. strain gauges 1, 4, 7, 10, 13 and 16 at radial fatigue test conditions are presented here. These particular gauges are chosen because of their orientation; gauges 1 and 4 are mounted on the spoke perpendicular to radial direction, gauges 7, 10 and 13 provide an estimate of the hoop strain whereas gauge 16 gives a measure of the radial strain in the spoke. A summary of the entire strain measurement dataset can be found in Appendix A.

Figure 4-8 shows the strain curves for strain gauges 1 and 4. As shown in Figure 4-4, the strain gauges 1 and 4 are located on two different spokes but in the same orientation. Hence, the same trend and numerical values in the strain graphs are expected. The gap between the peaks of the two curves shows the time taken by the wheel to rotate the angular distance between the two gauges.

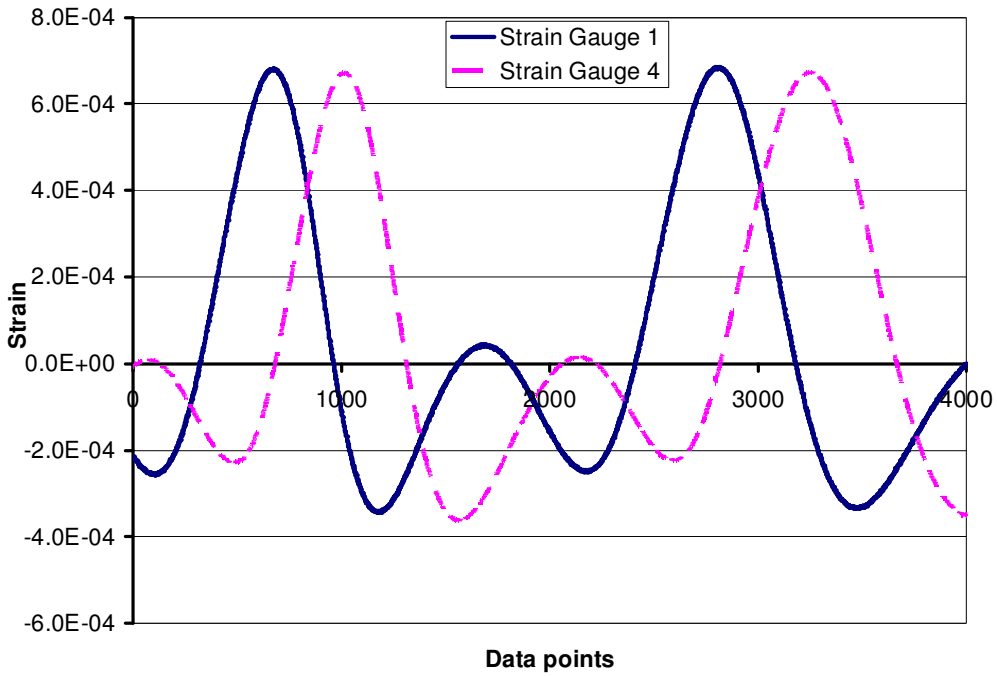

Figure 4-8. Strain graphs for gauges 1 and 4

Figure 4-9 shows measurements for strain gauges 7 and 10, respectively. Strain gauges 7 and 10 show similar trends but the strain levels of strain gauge 10 are much higher than that of strain gauge 7. The difference in strain levels can be attributed to their different locations (see Figure 4-4). Strain gauge 7 is located near a stiff spoke region; hence the stress in that area gets well distributed and results in a lower strain level whereas strain gauge 10 is located near the opening between two consecutive spokes, the stiffness of the area around strain gauge 10 is lower which is believed to have resulted in the higher strain values.

Figure 4-10 shows the measurements for strain gauge 13. Strain gauge 13 is of special interest in this study because of its position on the inboard bead area where rim deformation takes place in the rim indentation model (refer to Figure 4-5). A large part of the strain curve lies in the tensile region. The maximum strain seen by strain gauge 13 is 1.03 $x10^{-3}$. This is higher than any other tensile strain zone in the wheel.

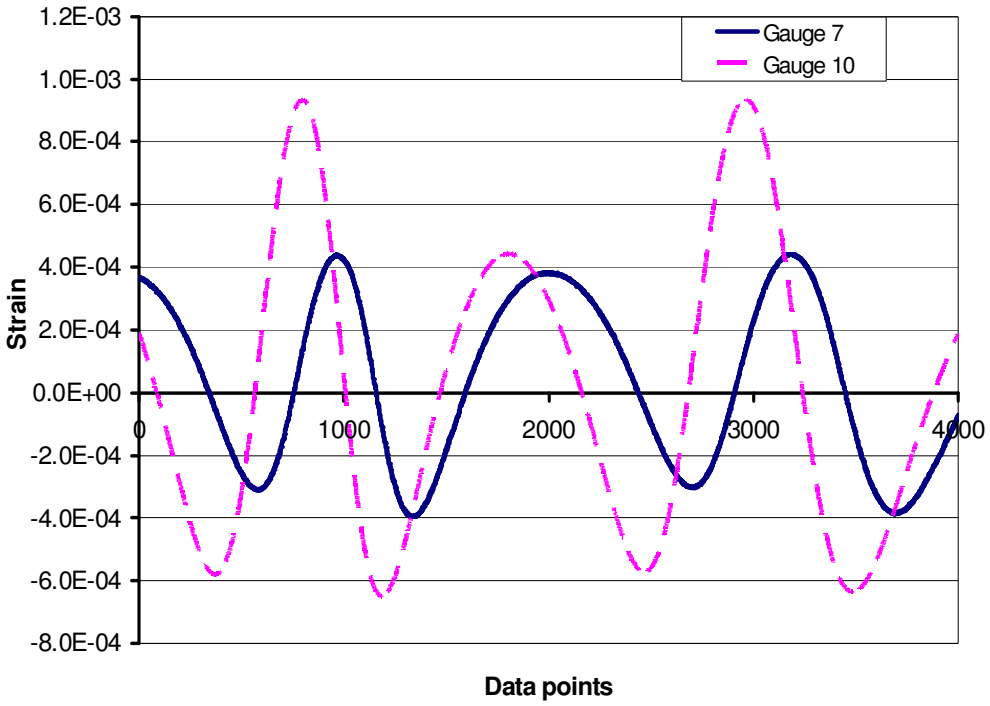

Figure 4-9. Strain graph for gauges 7 and 10

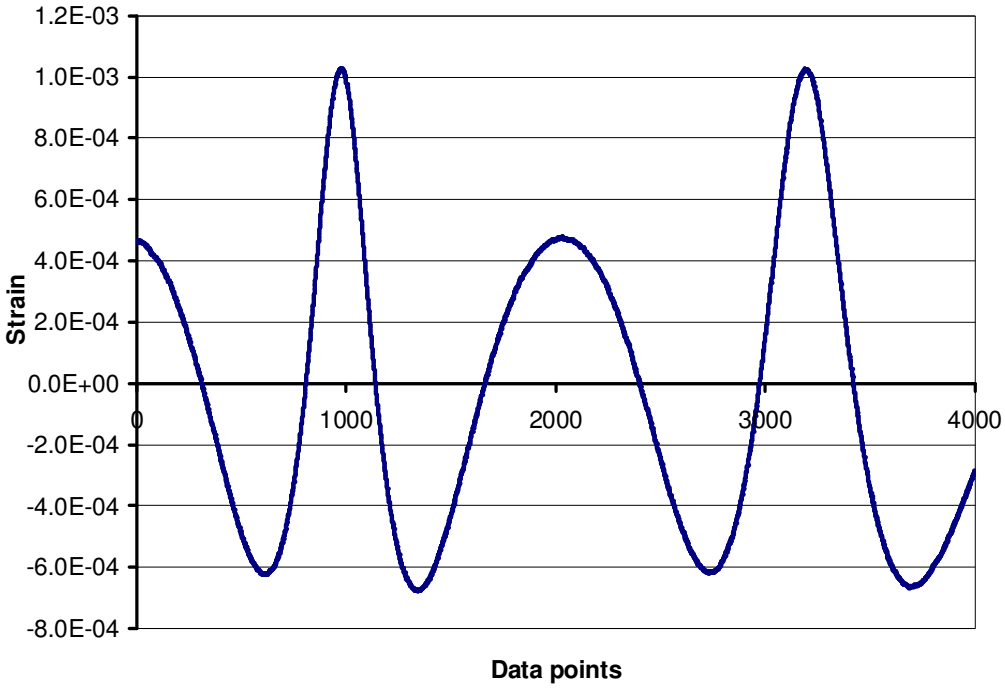

Figure 4-10. Strain graph for gauge 13

Figure 4-11 shows the measurements for the strain gauge 16. Strain gauge 16 was the only strain gauge in the experiment which did not show any tensile strain during the radial fatigue test. High compressive strains were seen in this spoke region. This can be attributed to the geometry of the wheel and high radial load applied on the wheel.

These strain curves provide information on the strain characteristics of the wheel during the radial fatigue test. This data was used to validate the Radial Fatigue model.

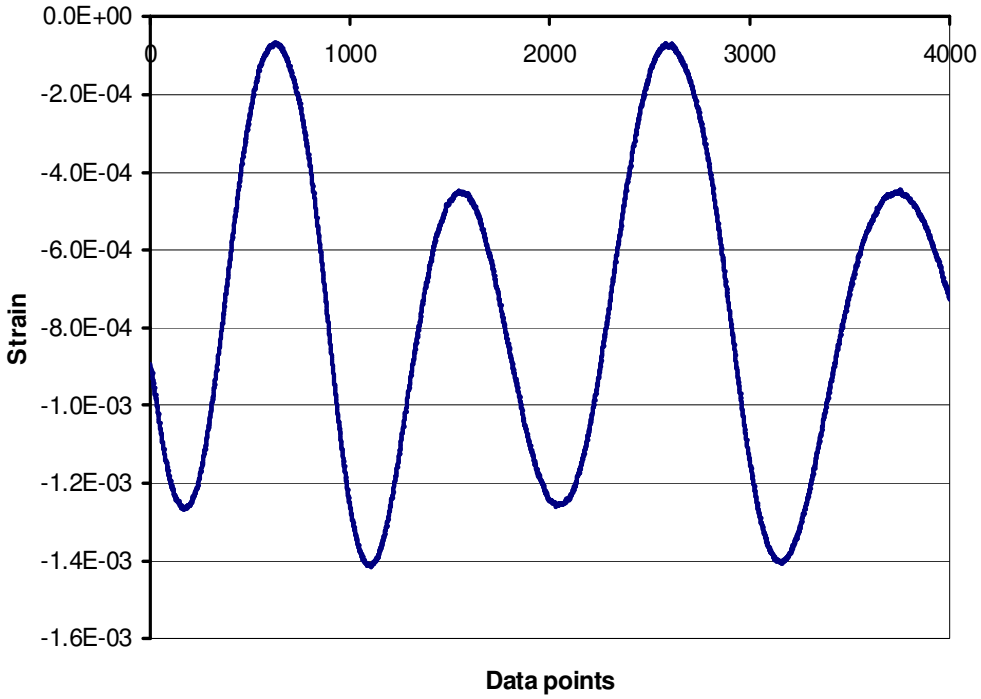

Figure 4-11. Strain graph for gauge 16

4.2. Laboratory-scale experiments

Two types of laboratory scale experiments were performed to: i) determine the mechanical properties of A356-T6 alloy and ii) develop an empirical relationship between fatigue life of pre-strained cast aluminum alloys and pre-strain level.

4.2.1. Tensile test

Laboratory scale tensile experiments were completed to determine the mechanical properties of A356 aluminium alloy used in the wheels. This was done because the mechanical properties like Young's modulus, and stress versus strain data for A356 available in the literature showed a wide amount of variability. Also, these mechanical properties are dependent on the casting and heat treatment processes and hence, are specific to each foundry. In order to make sure that all the mechanical properties used in the modeling work pertain to the aluminum alloy used by the wheel manufacturing company, laboratory scale tensile tests were performed on test specimens machined from the inboard flange section of a wheel manufactured at the foundry.

4.2.1.1. Tensile test set up

Tensile test specimens were machined by the machine shop in the Department of Materials Engineering at UBC. The dimensions of the tensile test specimen, shown in Figure 4-12, were selected according to the ASTM E8 standard. All dimensions are in mm.

An Instron 8874 servomechanical test platform (refer Figure 4-13) was used to conduct uniaxial tensile tests. The testing machine is equipped with a 25 kN load cell and interchangeable, hydraulic wedge-shape grips for holding test specimens. Tests were conducted in displacement control mode based on crosshead position. The combination of the small cross-sectional area of the gauge length and the alloy resulted in the expectation of low peak loads during these tests. Thus, limited machine compliance was expected. However to accurately measure strain in the sample, extensometers were mounted on the samples. Wavemaker, the Instron machine control software, was used to control the cross-head displacement during the test.

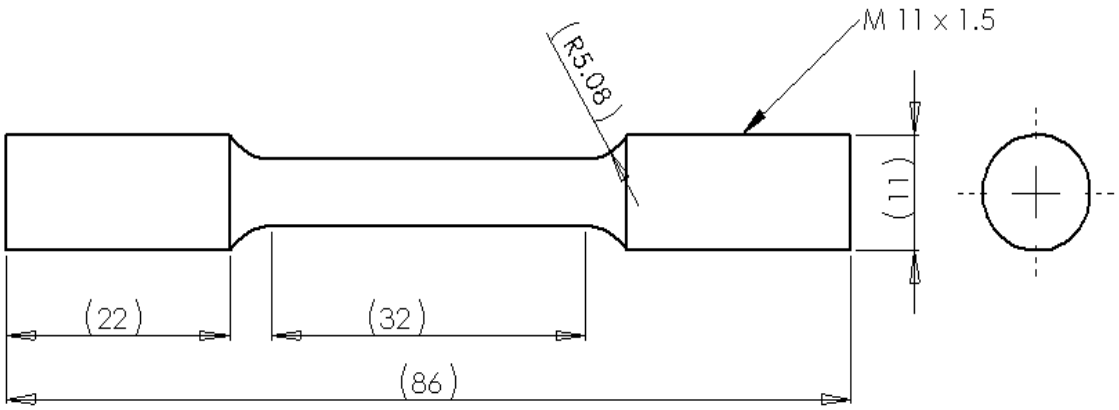

Figure 4-12. Tensile test specimen

Figure 4-13. Instron 8874 servomechanical test platform

4.2.1.2. Test procedure

A set of threaded adapters were fabricated to mount the tensile samples in the Instron 8874 servomechanical test platform because the hydraulic grips would not accommodate the sample diameter. Locknuts were used with the adapters to ensure that the test samples were held rigid in the machine. The assembled sample and adapters were placed between the grips of the Instron machine and the jaws of the machine were tightened. Two tensile tests were performed at a strain rate of $0.01s^{-1}$. The first sample was strained to 15% where as the second was strained to failure.

4.2.1.3. Results

The change in the gauge length of the extensometer and load applied to the tensile sample were recorded. The change in length was converted to engineering strain and then consequently to true strain using equations (4-1) and (4-2). Similarly, engineering stress and true stress values were calculated using equations (4-3) and (4-4).

$$e = \frac{\Delta L}{L_o} \tag{4-1}$$

$$\varepsilon = \frac{\partial L}{L} = \ln\left(\frac{L_f}{L_o}\right) = \ln(1+e) \tag{4-2}$$

where e and ε refer to engineering and true strain, respectively. L_o refers to the initial length (initial extensometer gauge length) whereas L_f refers to the final length. ΔL and ∂L represents total change in gauge length and infinitesimal change in length.

$$\sigma_{eng} = \frac{F}{A} \tag{4-3}$$

$$\sigma_{true} = \frac{F}{A_{inst}} = \sigma_{eng}(1+\varepsilon) \tag{4-4}$$

where σ_{eng} and σ_{true} refer to engineering and true stress, respectively. F is the load applied, A is the initial area of cross-section whereas A_{inst} represents instantaneous area during the test.

The true stress versus true strain curves for the two tensile tests are shown in Figure 4-14. The similarity of the curves indicates an accurate and repeatable test. The Young's modulus, calculated as the slope of the engineering stress versus strain curve in the elastic range with low strain, were 67.53 and 66.25 GPa. A line was drawn with slope equal to the Young's modulus offset by 0.2% engineering strain to intersect the engineering stress-strain curve to estimate the yield strength. The calculated yield strengths were 167 and 164 MPa. The ultimate tensile strength were estimated from the true-stress versus strain curve (see Figure 4-14) to be 319 and 317 MPa with 16% strain to failure.

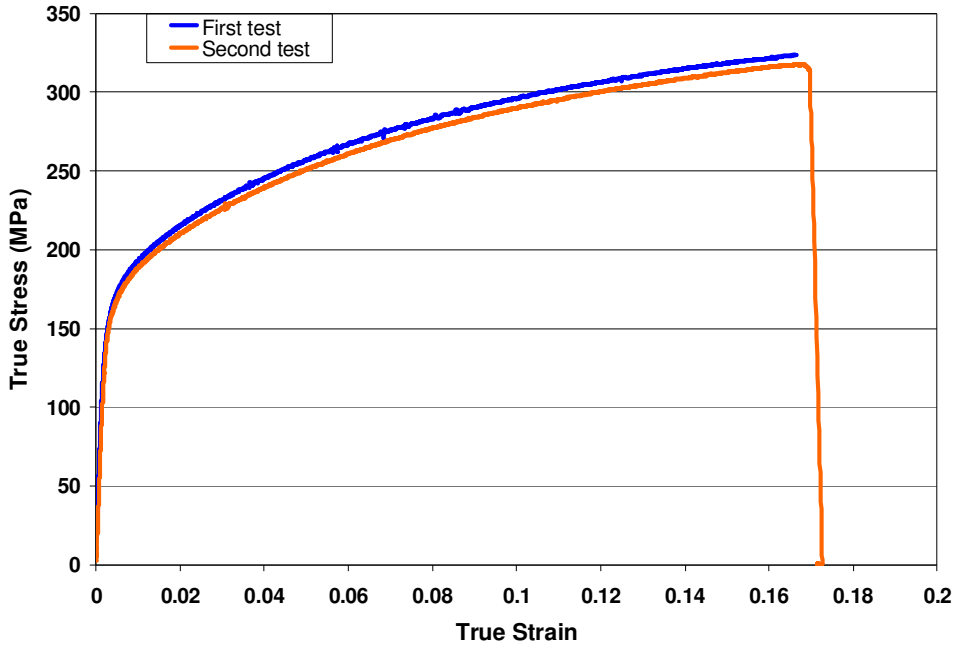

Figure 4-14. Flow curves alloy A356

4.2.2. Fatigue life experiments

The literature review revealed that there is an absence of research work available on fatigue life of pre-strained cast aluminum alloys. It has also been noted that in order to predict the fatigue life of wheels following rim indentation testing, a numerical model of fatigue life for pre-strained cast aluminum alloys is required. In order to formulate such an empirical relationship, lab-scale fatigue experiments were performed with pre-strained fatigue samples.

4.2.2.1. Fatigue sample and test setup

Samples for fatigue testing were produced by the machine shop in the Department of Materials Engineering at UBC. The samples, shown in Figure 4-15, with dimensions in mm were machined according to ASTM standard E466 with dimensions are in mm. In the literature review, it was noted that the fatigue life of cast aluminum alloys depends on the size of its microstructure and defects. In the industrial radial fatigue tests on wheels following rim indentation testing performed by the wheel manufacturing company, fatigue failures were observed on the inboard rim flange at the indented location. This was contrary to other radial fatigue tests performed by the wheel manufacturing company on the wheels free of any rim indentation, where fatigue failure occurred at the spoke region. It was inferred from these tests that the microstructure, defects and the permanent deformation at the inboard flange are together responsible for crack formation. To ensure that the laboratory scale fatigue samples had the same defects and microstructure as the inboard flange of the wheels, fatigue samples were machined out of the inboard rim sections of a series of wheels supplied by the manufacturer.

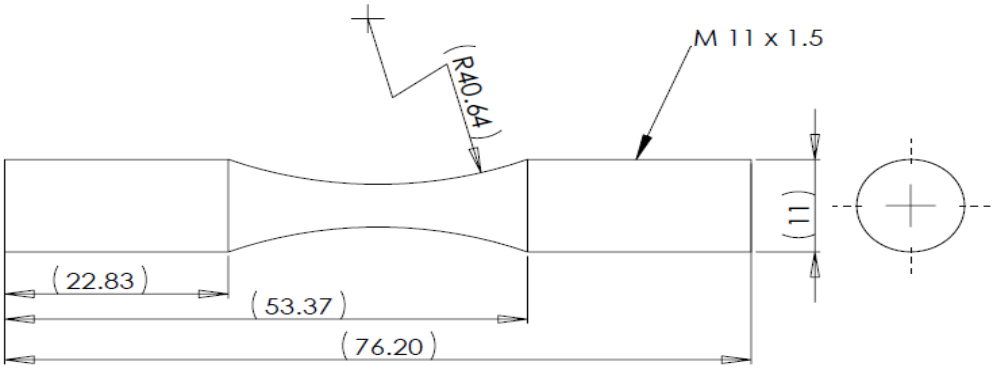

Figure 4-15. Fatigue specimen

A Sonntag uniaxial fatigue testing machine (refer to Figure 4-16) was used for these experiments. In this machine, a cyclic force is generated by an eccentric mass spinning at 1800 rpm. The offset of the eccentric mass from the center of rotation is adjusted to control the load amplitude. The specimen fixture is mounted on the oscillator housing. Only the vertical component of the dynamic force is transmitted to the specimen since the horizontal component is absorbed by the flexplates (Manufacturer's manual), refer Figure 4-17.

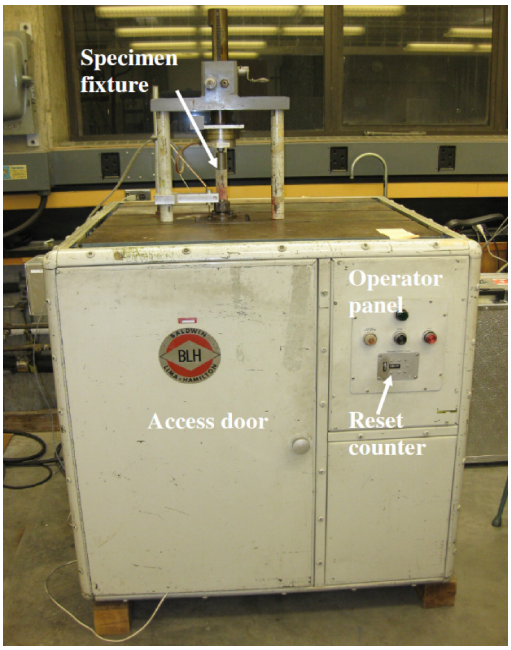

Figure 4-16. Sonntag fatigue machine

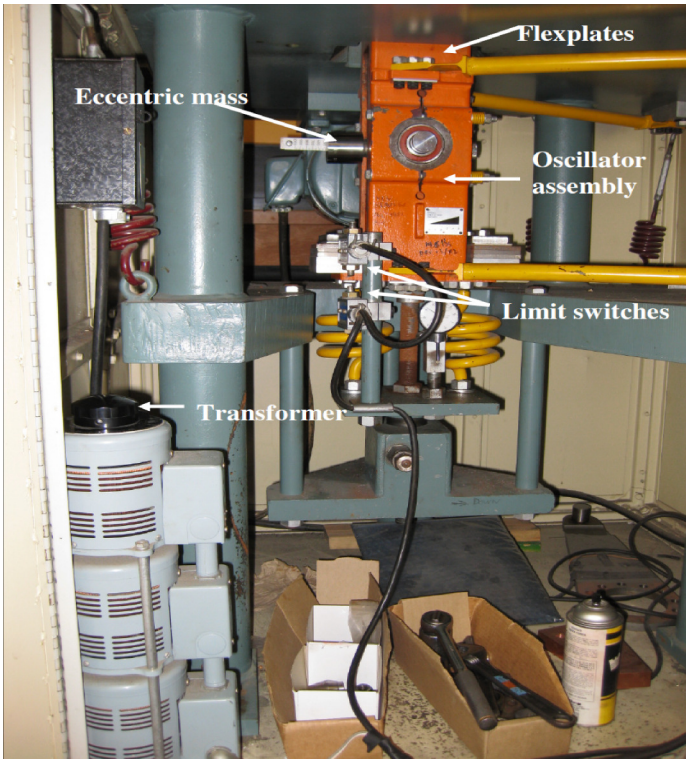

Figure 4-17. Sonntag fatigue machine assembly

The fatigue machine has been instrumented with an Omega LCHD- 2000 lb load cell and a Linear Variable Differential transformer (LVDT), to measure the load and oscillator table displacement, respectively (refer to Figure 4-18). As the test is displacement controlled, a data acquisition system is used to monitor the LVDT during a test. The data acquisition program written in LabView acquires a baseline amplitude of the displacement waveform in 3 cycles and compares that to the amplitude of displacement acquired during the test. If the waveform changes by more than a prescribed amount (1-2%), the test is automatically stopped. Using this system, tests can be stopped allowing the surface of the sample to be checked for the presence of cracks using die penetrant inspection. If a crack is detected, testing is stopped, otherwise the test is restarted. Using this approach, testing can be stopped before catastrophic failure which destroys the fracture surface of the sample.

Before running the fatigue test, the load cell is used to check the pre-load applied to the fatigue sample, adjustments are made to the sample fixture to ensure zero pre-load. This step is necessary as the fatigue tests are performed at fully reversed stress cycles, i.e. R=-1. During testing, the load amplitude waveform is checked to ensure that it is sinusoidal. Noise in the signal suggests loose assembly which can be rectified by checking all connections.

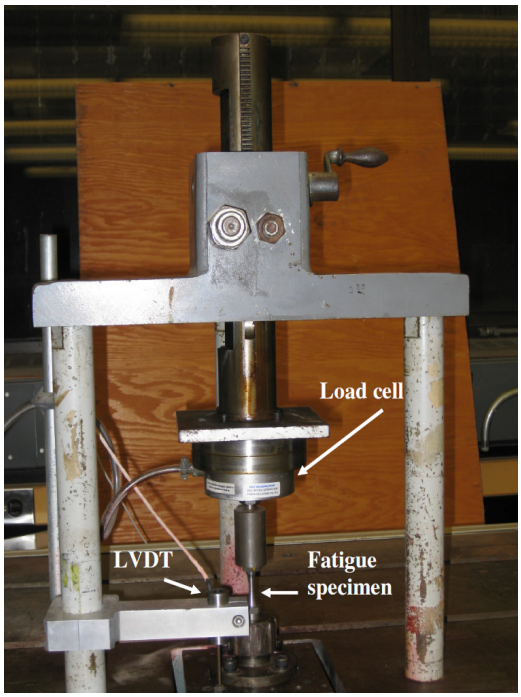

Figure 4-18. Instrumentation on fatigue machine

4.2.2.2. Pre-strain levels and technique

Prior to fatigue testing, samples were pre-strained to impose inelastic deformation. In order to make the laboratory scale fatigue experiments more representative of the strain conditions present in wheels following rim deformation tests, a maximum pre-strain level for the laboratory scale experiments was selected using the rim indentation model that will be described in Chapter 5. The peak plastic strain predicted by the model was 10%. Hence, the pre-strain levels selected for the laboratory fatigue experiments were 5% and 10%.

The Instron 8800 servomechanical test platform (refer Figure 4-13) was used to pre-strain samples prior to fatigue testing. The fatigue samples have an hourglass shape that results in a continuous variation of stress and strain along the gauge length. A 2D axisymmetric model of a fatigue sample was developed in ABAQUS to determine the required cross-head displacement to achieve the desired pre-strain. The model, shown in Figure 4-19, employed the flow stress data measured via the tensile tests described in Section 4.2.1. Boundary conditions were applied at the bottom edge and the vertical axis of the fatigue sample. The top edge of the sample was displaced. The effect of the displacement on the fatigue sample in terms of plastic strain was estimated. Figure 4-19 shows the equivalent plastic strain at the neck region of the fatigue sample. The middle of the sample sustains maximum plastic strain shown in red color and the majority of the sample does not undergo any plastic strain, shown in dark blue color. The peak load predicted at 10% strain was 5 kN which agreed well with the measured load of 5.35 kN. Using these results the cross-head displacements for 5 and 10% pre-strain in the neck region of the fatigue samples were determined to be 0.5155 and 0.9787 mm, respectively.

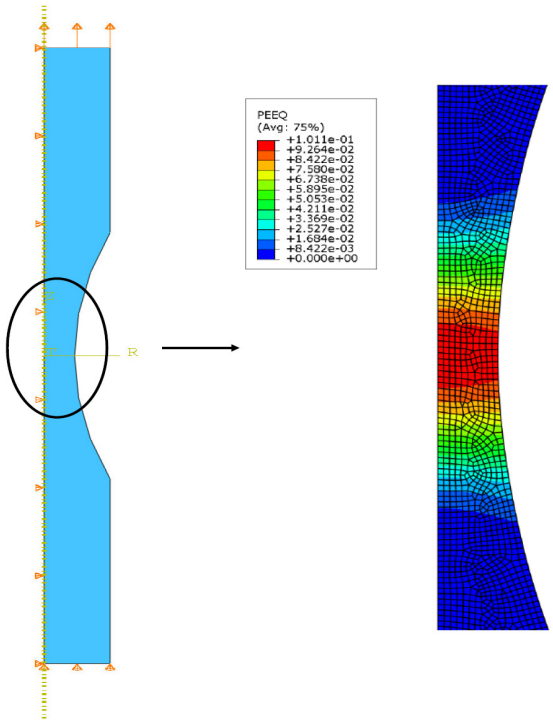

Figure 4-19. Axisymmetric model of fatigue sample

4.2.2.3. S-N data

Figure 4-20 shows the fatigue life data for the 0 (unstrained), 5 and 10% pre-strained fatigue samples. The tests were conducted at four different amplitude stress levels: 140, 120, 100 and 80 MPa at a stress ratio (R) of -1. At each stress level, a minimum of 3 and a maximum of 6 samples were tested for each level of pre-strain. The data clearly shows a decrease in fatigue life with increase in pre-strain level. At a stress amplitude of 140 MPa, the shift in fatigue life with pre-strain is clearly delineated. At stress amplitudes of 120 MPa and 100 MPa, the fatigue life of pre-strained samples is less than unstrained fatigue samples but it is difficult to distinguish between 5 and 10% pre-strained samples as to which have lower fatigue life. At a stress amplitude of 80 MPa, 3 out of 4 fatigue samples tested at 0% pre-strain did not display fatigue failure after testing for 10 million cycles. These points are showed as "runout" in Figure 4-20. As far as 5 and 10% pre-strained sam-

ples are concerned at this stress level, most failed before 1 million cycles. The laboratory scale experiments clearly show that unstrained A356 has longer fatigue life.

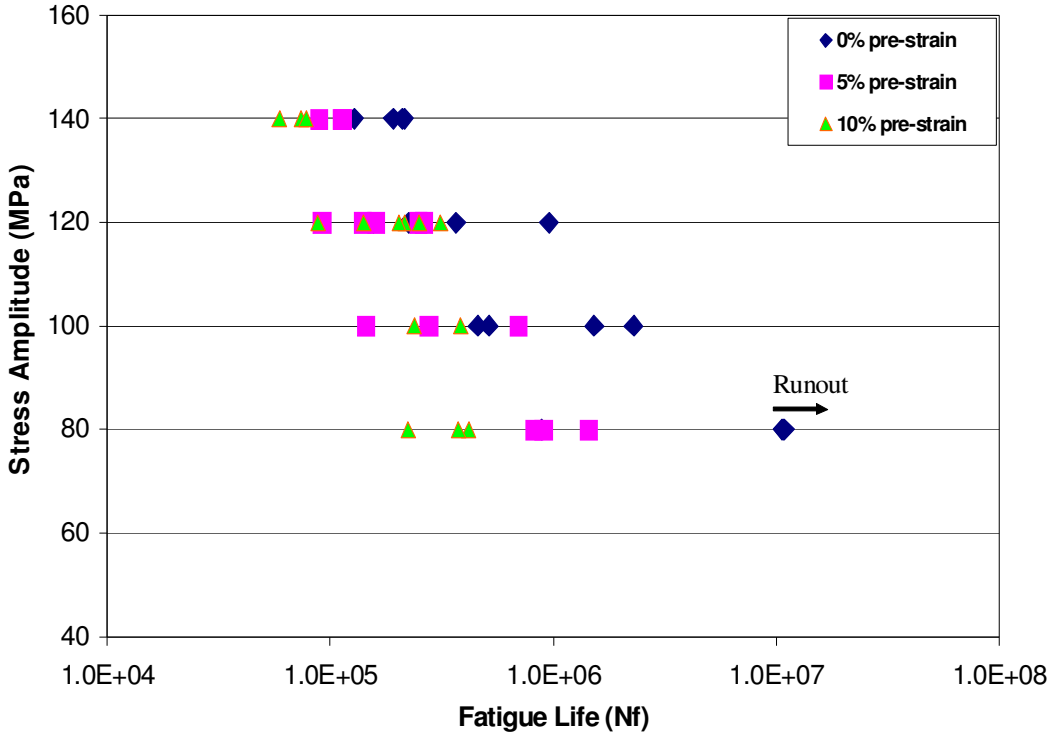

Figure 4-20. Fatigue life data

4.2.2.4. Modified fatigue life equation

The pre-strained fatigue life data was analyzed to quantify the effect of pre-strain and to develop an equation capable of predicting fatigue life based on stress amplitude and level of pre-strain. Figure 4-21 shows the trendlines and their equations for the fatigue samples. The equations can be re-written as:

$$N_{f0\%} = e^{\frac{-(\sigma_a - 324.04)}{16.021}} \tag{4-5}$$

$$N_{f5\%} = e^{\frac{-(\sigma_a - 364.76)}{20.355}} \tag{4-6}$$

$$N_{f10\%} = e^{\frac{-(\sigma_a - 426.72)}{25.907}} \tag{4-7}$$

where, $N_{f0\%}$, $N_{f5\%}$ and $N_{f10\%}$ represent fatigue life of 0, 5 and 10% pre-strained fatigue samples, respectively.

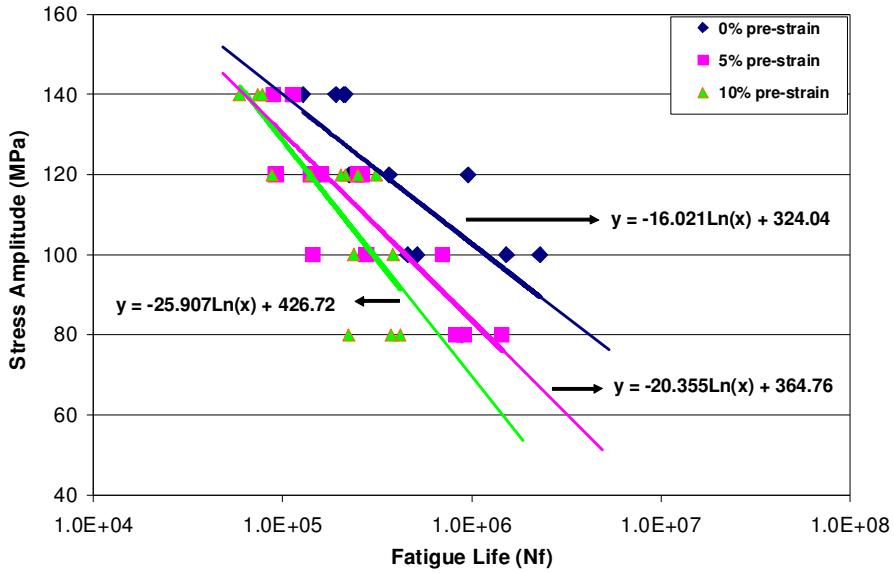

Figure 4-21. Trendlines- fatigue life

To qualitatively assess the effect of pre-strain on the fatigue life, the difference between equations (4-6) and (4-7) and the 0% pre-strain equation were plotted and can be seen in Figure 4-22.

Figure 4-22 shows a graph of the change in fatigue life versus the amplitude stress level. The graphs show that at high amplitude stress levels, the decrease in fatigue life due to pre-strain is almost zero, i.e. at high stress levels; pre-strain shows no prominent effect on the fatigue life for cast A356. From this observation, it can be implied that at high stress levels, the localized plastic stress and strain distributions around the defects dominate the fatigue crack growth rate relative to the induced level of pre-strain concentration. On the other hand, at low amplitude stress levels, a prominent effect of the pre-strain can be seen from Figure 4-22. The fatigue life decreases with an increase in the level of pre-strain level as the blue dashed line is above the solid pink line, which represent decrease in fatigue life for 10% and 5% pre-strained samples, respectively. It can also be inferred that at low amplitude stress levels, localized stress and strain concentrations around the defects in cast

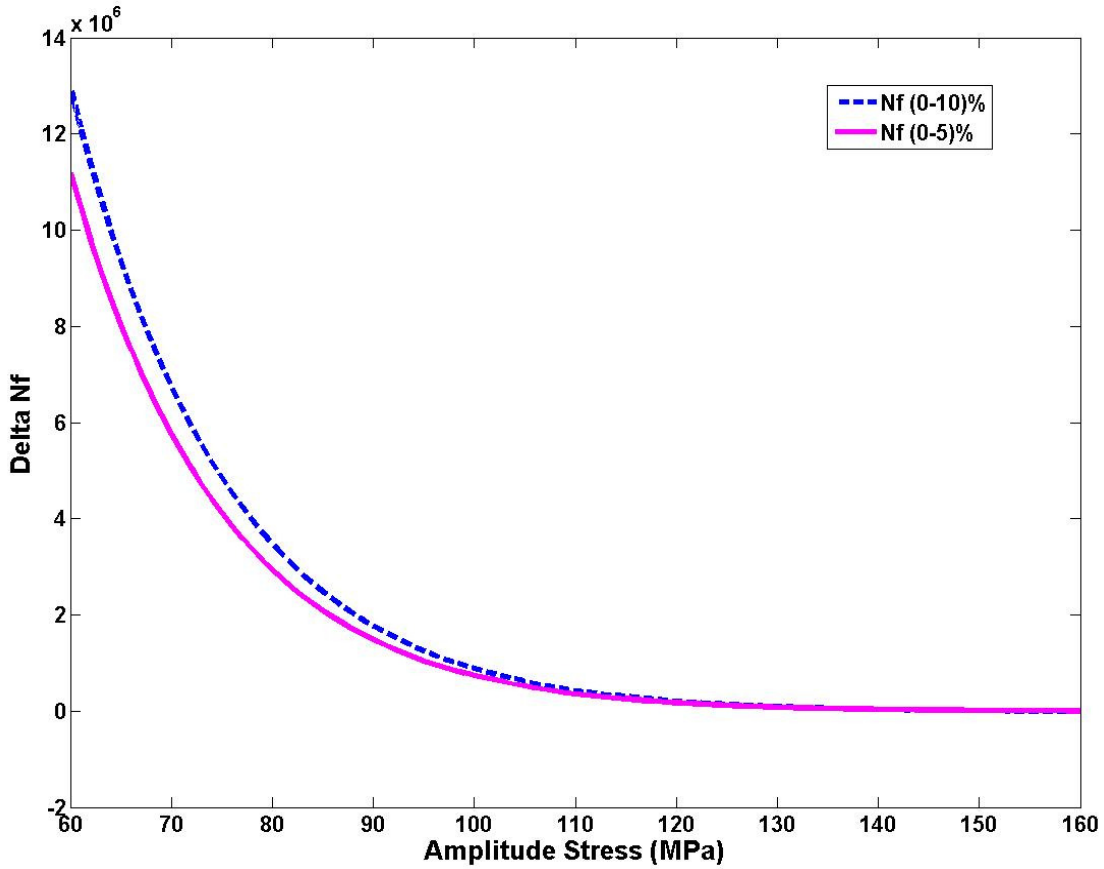

Figure 4-22. Effect of pre-strain on fatigue life

A356 are not as high, as a result pre-strain plays a major role in crack initiation/propagation.

Section 2.1.2.2 discussed the effect of micro-porosity on the fatigue life. It was mentioned that when pores are responsible for fatigue crack propagation, the fatigue initiation life is very small and can be neglected. The fracture surfaces of the fatigue samples were analyzed to identify the defect(s) responsible for fatigue crack initiation. Figure 4-23 shows a Scanning Electron Microscope (SEM) picture of a fatigue sample fracture surface. The pore shown in the figure was determined to be the fatigue initiating defect due to two reasons: i) the proximity of the pore to the surface was very close and ii) the area around the pore showed marks/ striations which validated the slow growth of fatigue crack. The initi-

ation site in each fatigue sample was examined and it was found that microporosity present either near or at the free surface was the fatigue failure causing defect in nearly all cases.

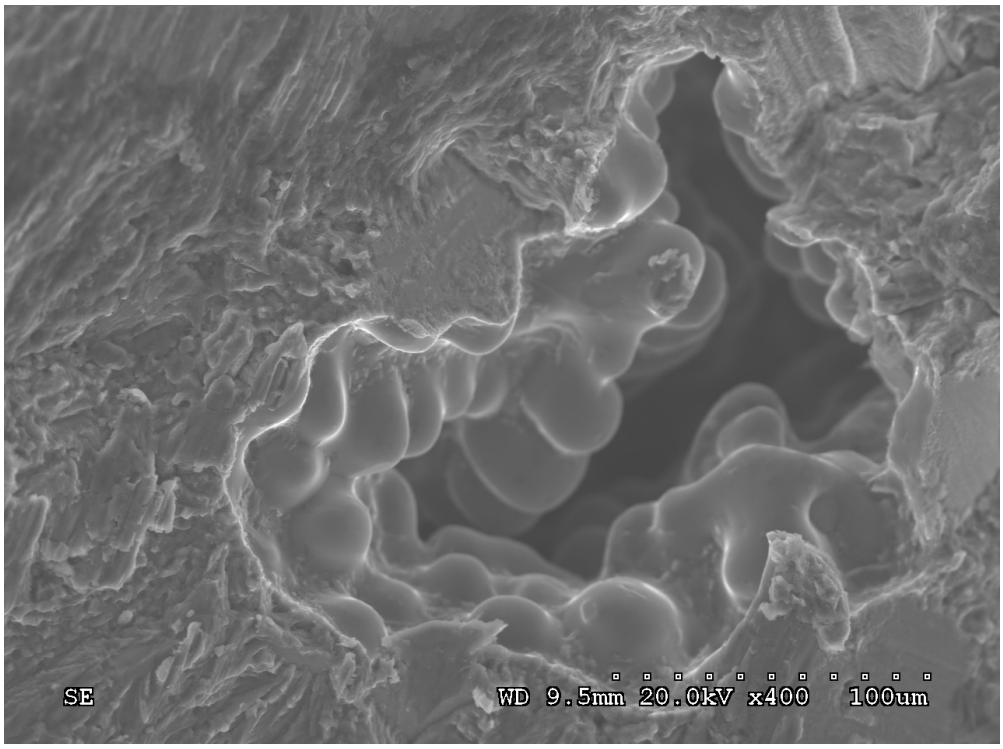

Figure 4-23. SEM picture of a pore in a fatigue sample

As microporosity was determined to be the cause of fatigue failure in the fatigue samples, the fatigue initiation life can be neglected for the cast A356 aluminum alloy used in this research work and the total fatigue life for the material can be described by the empirical fatigue propagation life relationship previously discussed (refer to equation (2-5)). A similar approach was used by Gao et. al. [2] where the fatigue propagation life (N_p) calculated using equation (2-5) was compared to the experimental fatigue life. They also assumed the final crack length (a_f) to be constant since fatigue propagation life is insensitive to it. In the current research project, all the fatigue samples were taken from the same location on the wheel, i.e. the inboard rim flange; therefore it has been assumed that initial crack length which is essentially the maximum pore size does not vary in the samples. As a result, initial

crack length (a_0) in equation (2-5) has been considered to be a constant in this research project. Hence, the fatigue life equation (2-5) can be modified to the empirical relation as shown in equation (4-8):

$$N_f = C_2 \left(\varepsilon_{\max} \frac{\sigma_a}{\sigma_y} \right)^w \tag{4-8}$$

where N_f is the total fatigue life. σ_a is the amplitude stress, σ_y is the yield strength, ε_{max} is the maximum total strain during a fatigue cycle, C_2 and w are parameters depending on the material and the level of pre-strain.

In order to determine C_2 and w for each level of pre-strain, equivalent stress ($\varepsilon_{max}\ \sigma_a/\sigma_y$) must be calculated. The analytical method of strain calculations cannot be used to determine the strain state of the fatigue sample because of the hour-glass shape of the fatigue sample. The axisymmetric model of the fatigue sample, shown in Figure 4-19 was used to estimate the equivalent stress at different stress levels for fatigue samples with varying levels of pre-strain. To simulate fatigue test conditions for samples with 5 and 10% pre-strain, the first step was to introduce pre-strain in the samples according to the technique discussed in Section 4.2.2.2. In the second step, a pressure load was applied on one end of the axi-symmetric model, keeping the other end fixed to produce the same stress conditions as used in the fatigue experiments. Simulations were performed at 140, 120 and 100 MPa amplitude stresses. Similarly for the fatigue samples with no pre-strain, the first step was skipped and directly, the second step was applied.

Figure 4-24 shows the variation of total fatigue life (N_f) with the equivalent stress, as represented by ($\varepsilon_{max}\ \sigma_a/\sigma_y$) in the equation (4-8) for 0, 5 and 10% pre-strained samples. In the equation ($\varepsilon_{max}\ \sigma_a/\sigma_y$), for a stress amplitude (σ_a) of 120 MPa, the ratio of amplitude and yield stresses (σ_a/σ_y) is same for all the fatigue samples, irrespective of the pre-strain. The differentiating parameter in the equation ($\varepsilon_{max}\ \sigma_a/\sigma_y$) is the total principal maximum strain (ε_{max}). For the un-strained (0% pre-strain) fatigue samples, the total maximum principal

strain (ε_{max}) is same as the elastic strain whereas for the 5 and 10% pre-strained samples, the total maximum principal strain contains both the elastic and plastic strains and it is dominated by the maximum principal plastic strain.

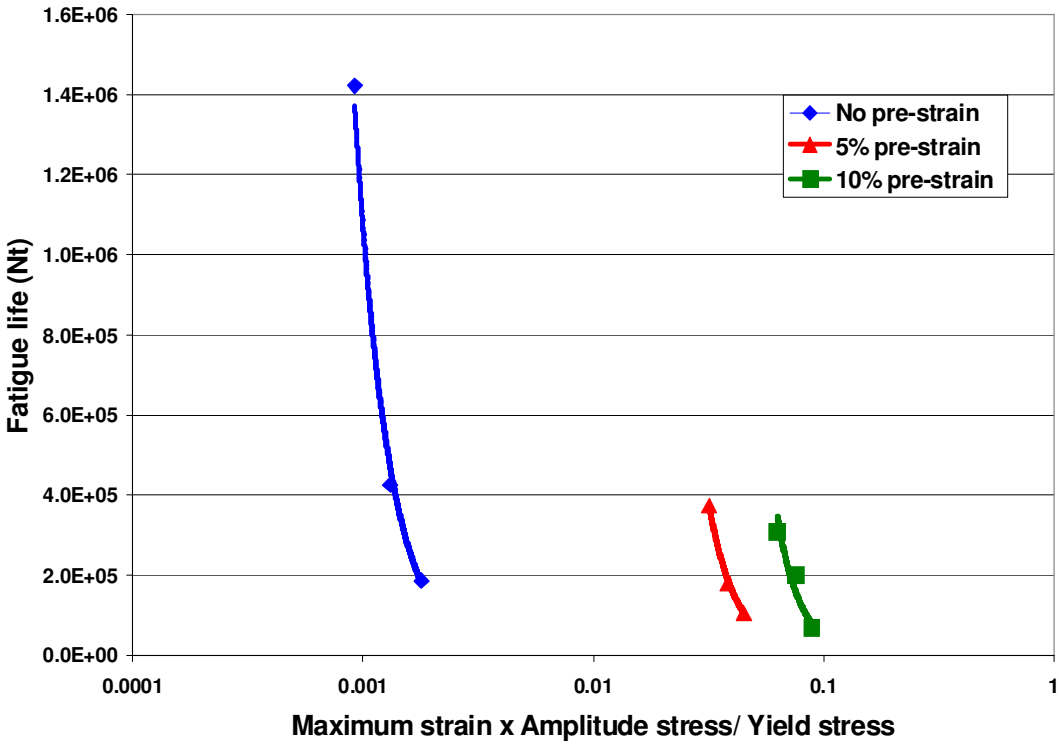

Figure 4-24. Fatigue life for samples with 0, 5% and 10% pre-strain

Parameters C_2 and w were determined by fitting a curve to the data points shown in Figure 4-24. The resulting equation to calculate fatigue life N_f for samples with no pre-strain is:

$$N_t = 0.0007\left(\varepsilon_{\max}\frac{\sigma_a}{\sigma_y}\right)^{-3.0585} \tag{4-9}$$

The parameters C_2 and w were determined to be 0.0007 and -3.0585 respectively. A similar procedure was followed for fatigue samples with 5 and 10% pre-strain. The C_2 and w derived for the 5% pre-strain level were 1.2336 and -3.6566 whereas for the 10% pre-strained samples, they were 2.5099 and -4.274, respectively.

Figure 4-25 shows the variation of C_2 and w with the level of pre-strain applied to the fatigue sample. It can be seen from the figure that both the parameters vary linearly with the level of pre-strain. Equations were developed to quantify the variation of parameters with the level of pre-strain which are shown as equations (4-10) and (4-11).

$$C_2 = 0.2509 \times \varepsilon_p - 0.0065 \tag{4-10}$$

$$w = -0.1216 \times \varepsilon_p - 3.0553 \tag{4-11}$$

where ε_p is the plastic strain in percentage.

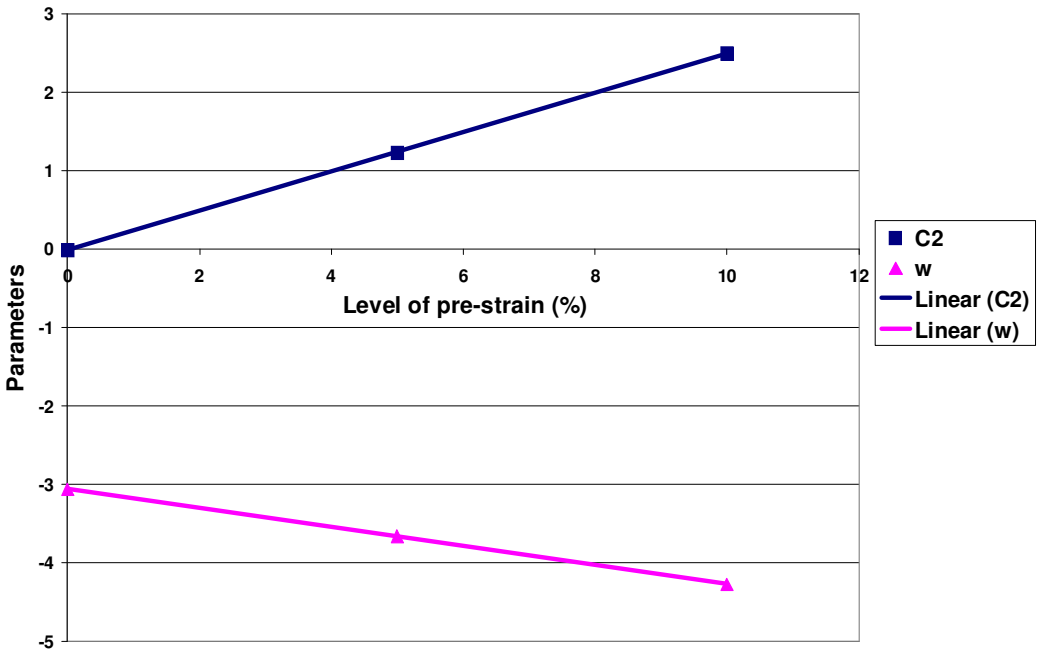

Figure 4-25. Variation of constants with pre-strain

Hence, equation (4-8) can be used in conjunction with equations (4-10) and (4-11) to determine the fatigue life of cast A356 aluminum alloy from the inboard rim flange location upto 10% level of pre-strain.

4.3. Summary

The rim indentation test provided the load versus deformation curve for the wheel. The radial fatigue test provided strain state at various locations on the wheel during the radial fatigue test.

The material data such as Young's modulus, yield strength and flow strength data for the A356 aluminum alloy used in this research project was calculated from the tensile test experiment.

The empirical fatigue life relation required to estimate the fatigue life of deformed wheels was developed by fatigue experiments on the pre-strained samples.

5 Model Development

5.1. Rim indentation model

A model of the rim indentation test was developed to predict the permanent deformation, plastic strain and residual stress distributions in a wheel following this test. The procedure for the industrial rim indentation test was explained in Section 4.1.1. Essentially, the rim is permanently deformed by the application of a predetermined static load in a mechanical testing machine. To solve this non-linear contact problem between the wheel and the platen, the commercial finite element software ABAQUS was used. This model will serve as a design tool to help engineers predict the deformation behavior of the wheels during the design stage.

5.1.1. Geometry

The geometry of the finished wheel was obtained in electronic format from the wheel manufacturing company. As the wheel is symmetric about the central plane A-A, shown in the Figure 5-1, the wheel geometry in the model may be simplified to a half section.

A three dimensional model of the platen was developed in ABAQUS. The dimensions of the platen geometry in the model were based on the specifications provided by the wheel manufacturing company. During the model development stage, the half section of the wheel geometry was meshed with 234,646 nodes arranged into 145,153 10-node tetrahedral elements. Figure 5-2 shows the finite element assembly of the wheel and the platen. The rim indentation model simulates the contact behavior between two separate bodies, the stress state developed on the wheel is a result of the load transferred to the wheel from the contact region between the platen and the wheel, hence a fine mesh was used in the contact region of the wheel to precisely simulate the contact process.

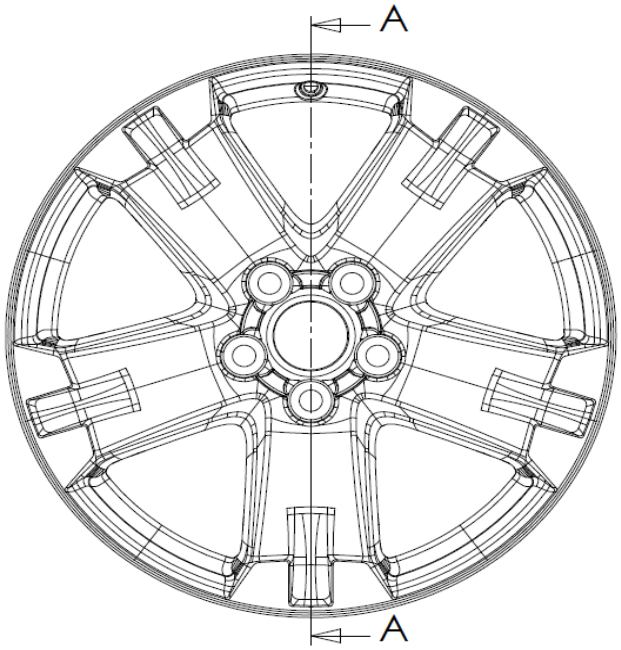

Figure 5-1. Finished wheel with symmetry plane

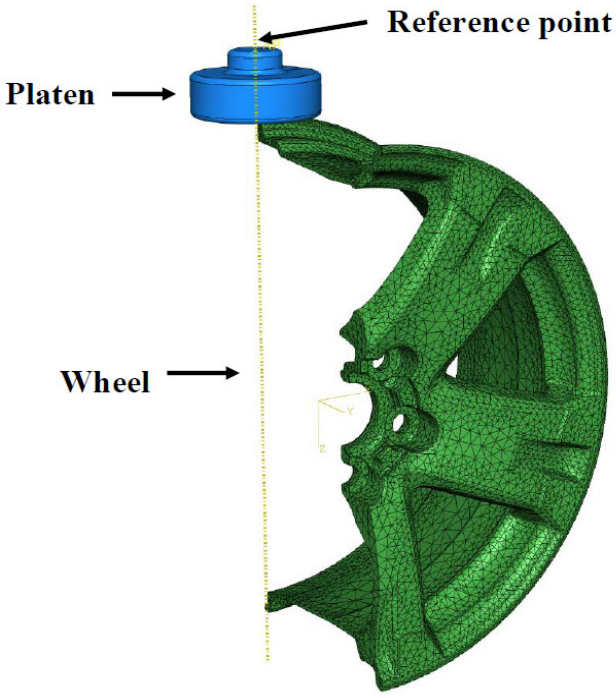

Figure 5-2. Finite element assembly model

The platen geometry was meshed with 18,689 rigid elements in ABAQUS CAE. Unlike the wheel, the platen geometry was not simplified to provide a flat surface, free of sharp edges and corners along the contact interface. If the platen were cut along the wheel symmetry plane, contact would occur along the cut edge. The simulation of contact between two such edges is not recommended as it can lead to convergence errors. Hence, the full geometry of the platen was used. The centre point at the top surface of the platen was chosen as the reference point for the rigid platen

5.1.2. Material properties

The material properties used for the A356 aluminum alloy of the wheel were determined by the tensile tests described in Section 4.2.1. Table 5-1 shows the true stress data used for alloy A356 in the model. The Young's modulus (E) of 66.25 GPa was also determined from the tensile test data. A Poisson's ratio used of 0.3 was employed based on published values [1].

Table 5-1. Flow stress A356 aluminum alloy

True stress (MPa)	Plastic strain
164	0
196	0.01
216	0.02
231	0.03
244	0.04
255	0.05
264	0.06
272	0.07
280	0.08
286	0.09
292	0.1
297	0.11
302	0.12
306.7	0.13
310.75	0.14
314.7	0.15
317.2	0.16

5.1.3. Initial conditions

Initially, the platen was positioned 0.5mm above the inboard flange of the wheel.

During the rim indentation model development stage, residual stresses developed during the quench stage of the T6 heat treatment and altered in the finish machining process were not accounted for to reduce the complexity of the model. However in earlier work at UBC, Estey [1] developed a thermal-mechanical model to estimate the residual stresses and plastic strain in a wheel following heat treatment. This procedure was later improved by Li [32] to include the effects of material removal during machining. After the development of the rim indentation model, the procedures developed by Estey and Li were followed to generate residual stress and plastic strain data for use as initial conditions in the model.

5.1.4. Boundary conditions

Figure 5-3 shows the boundary conditions for the Rim Indentation model. The nodes on the symmetry plane of the wheel were constrained in the X-direction. This constraint was applied to enforce symmetry on this plane during the simulation.

In the industrial rim indentation experiment, the wheel is mounted on to a shaft and held in position by bolts tightened on to the hub, refer Figure 4-1. In the Rim Indentation model, all nodes in the bolt region of the wheel were constrained in all degrees of freedom.

The platen only moves along the vertical direction in the industrial rim indentation tests. Hence, in the model, motion of the platen in the X and Y directions was constrained. The only motion allowed for the platen during the simulation was in the Z direction.

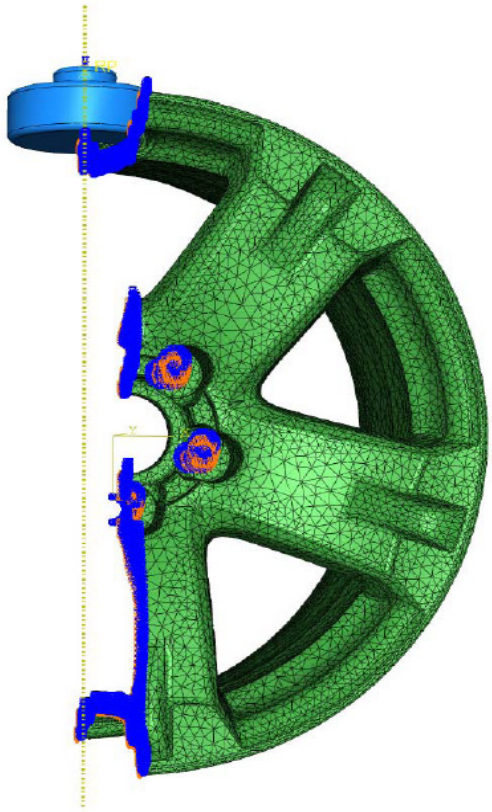

Figure 5-3. Boundary conditions in rim indentation model

5.1.5. Loading description

The application of load in the Rim Indentation model required 3 model steps:

1) Establish contact - In the first step, contact was established between the platen and the wheel. As mentioned in the Section 5.1.3, at the start of a rim indentation test, the platen was 0.5 mm above the inboard flange of the wheel. In the first step, the platen was moved down a distance of 0.6 mm. The extra 0.1 mm of translation ensured planar contact was established between the platen and the wheel as opposed to a point contact.

2) Apply load - In the second step, a concentrated force was applied at the reference point of the platen. This load in turn deformed the wheel.

3) Remove load - In the third and final step, the concentrated force at the reference point of the platen was reduced to zero.

5.1.6. Contact definition

A contact condition was defined between the surface of the platen and the inboard rim flange of the wheel. A contact condition in ABAQUS consists of two interacting surfaces called a contact pair. The two interacting surfaces are assigned either master or slave properties. The general rule is to make the stiffer surface the master surface. Thus, in the rim indentation model, the bottom surface of the platen, defined with rigid elements was defined as the master surface. The top surface of the inboard rim flange was defined as the slave surface (refer to Figure 5-4). Although ABAQUS offers additional contact definition options, this type of surface-to-surface contact was used because it eliminated large penetration errors that developed using other methods. The mesh of the contact surface on the wheel was made finer than the other regions to enable smooth contact between the platen and the wheel surfaces. Coarse mesh at the contact surfaces with surface-to-surface discretization can lead to very high computational time. Hence, finer mesh at the contact surfaces was used to optimize computational time with accurate results.

Finite sliding of the contact surfaces relative to each other was enabled in the rim indentation model. The finite sliding tracking feature allows for arbitrary sliding, separation and rotation at the contact surface. This approach was suitable for the modeling work because in the rim indentation model some degree of sliding between the master surface of the platen and the slave surface of the wheel was expected.

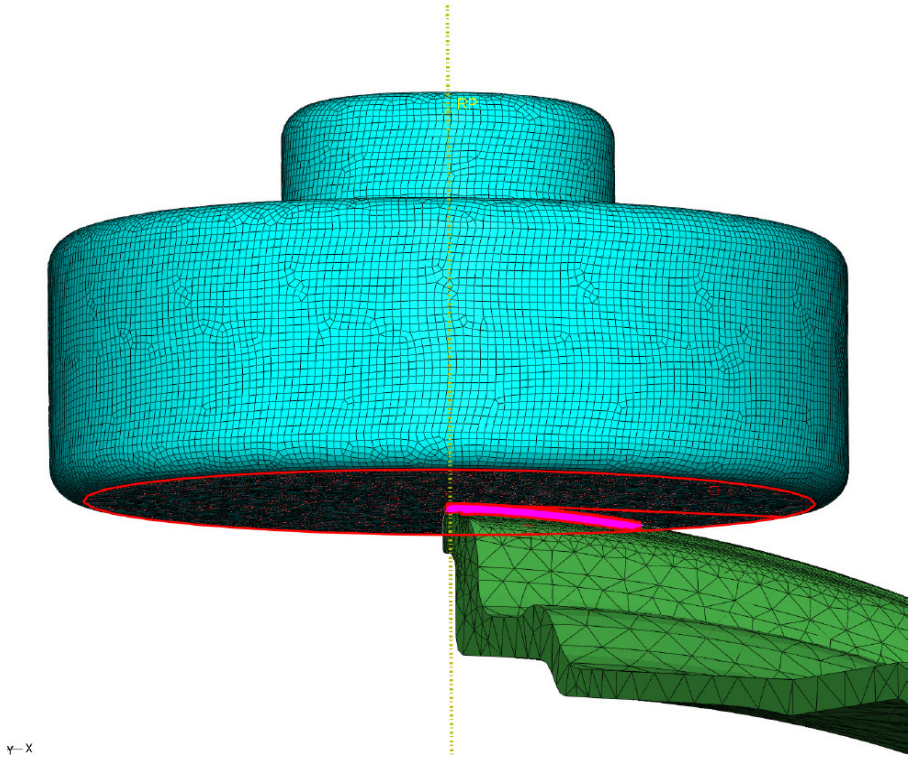

Figure 5-4. Contact pair in rim indentation model

5.2. Radial fatigue test model

The radial fatigue model was developed to simulate the stress state of the wheel during testing. Using the predictions of this model, the fatigue life for rim indented wheels can be predicted by the fatigue life equation described in Section 4.2.2.4. A description of the industrial radial fatigue test for wheels was presented in the literature review.

5.2.1. Geometry

The same type of finished wheel as used in the rim indentation model was used in the radial fatigue model. However, for this model, a mesh of the complete wheel was necessary because of the rotation that occurs during the test. The wheel was meshed with 72,485 nodes arranged into 39,724 10-noded quadratic tetrahedral elements, refer to Figure 5-5. The number of nodes and elements used in the development of the radial fatigue model is less than the rim indentation model discussed in Section 5.1.1, the reason for the difference depends on the complexity of the model. In the radial fatigue model, the load applied on the wheel is precisely defined in terms of the amount and location on the wheel as discussed in Section 5.2.5. The radial fatigue model is simpler in terms of its complexity, hence a fewer number of nodes were required in this model.

5.2.2. Material properties

The material properties used in the radial fatigue model for the A356 aluminum alloy were the same as described in Section 5.1.2. In this model, no plastic strain was expected to develop because the loads are relatively low.

5.2.3. Initial conditions

During the development of the radial fatigue model, no initial conditions were considered to simplify the model. However as discussed earlier, residual stresses and plastic strains are developed in finished wheels due to the quench and machining processes. The distributions of these quantities were calculated based on the procedures developed by Estey [1] and Li [32] and then used as initial conditions in the final radial fatigue model.

5.2.4. Boundary conditions

When the wheel is mounted on to the Radial Fatigue test machine, the hub of the wheel is held on the shaft of the machine by bolts, hence in the radial fatigue model, all the nodes in the bolt region of the wheel were constrained in all degrees of freedom (refer to Figure 5-5)

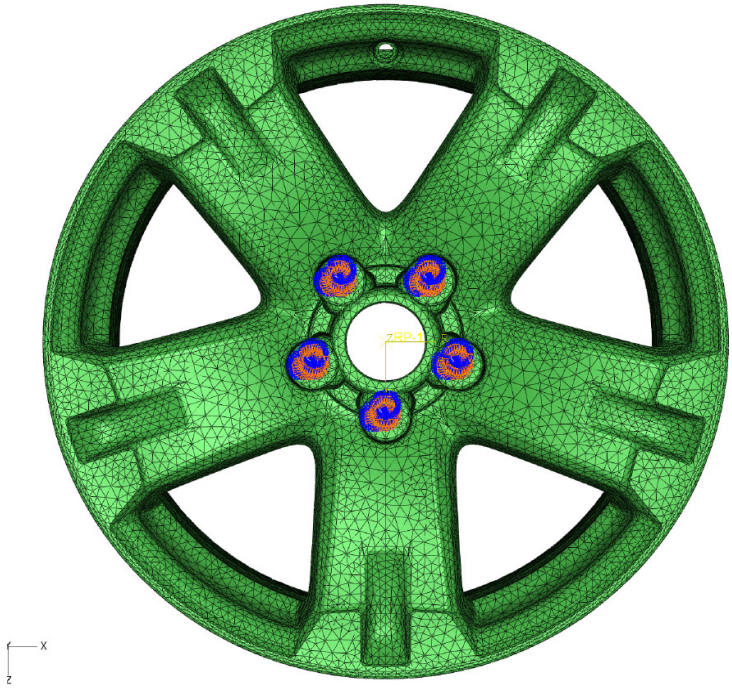

Figure 5-5. Meshed model of the wheel with boundary conditions

5.2.5. Loading description

The application of load in the Radial Fatigue model occurred in two steps:

1) Apply pressure load - A pressure load of 60 psi was applied on the wheel to simulate the loading caused by inflation of the tire. Figure 5-6 shows the area on the wheel where pressure load is applied. The pressure load also results in a transverse load on the inboard and outboard flange which was taken in account during the early stages of model development but its effect was found to be almost negligible on the stress state of the wheel.

2) Apply radial load - The radial load due to contact with the drum (refer to Figure 4-7) was applied on the wheel and the wheel was rotated. Based on the radial fatigue tests conducted, the radial load applied to the wheel was 1560 kgf and the wheel was rotated at 3 km/hr.

As discussed in Section 2.5, when the tire is pressed against the drum, load is applied to a contact patch or area on the tire. Stearns et. al. [29] defined the effect of radial reaction force on the wheel as a pressure load using a cosine waveform spanning a total angle of 80°. The pressure load is maximum at the centre and minimum at the two ends of contact area (refer to Figure 5-7). The load applied to the tire is applied to the inboard and outboard bead area of the wheel, shown in Figure 5-8, where the tire is in contact with the wheel. Stearns et. al. [29] also proposed the load on the bead area should be applied normal to the surface of the beads. Hence, the radial load in the radial fatigue model was applied normal to the bead surface.

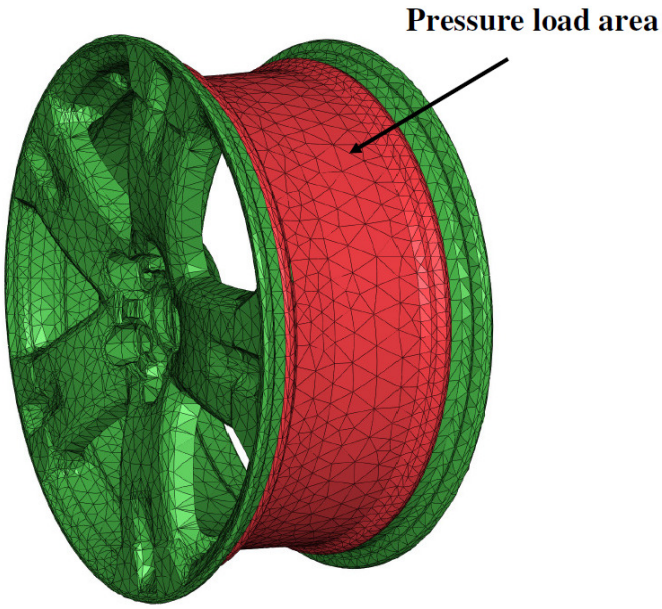

Figure 5-6. Pressure load

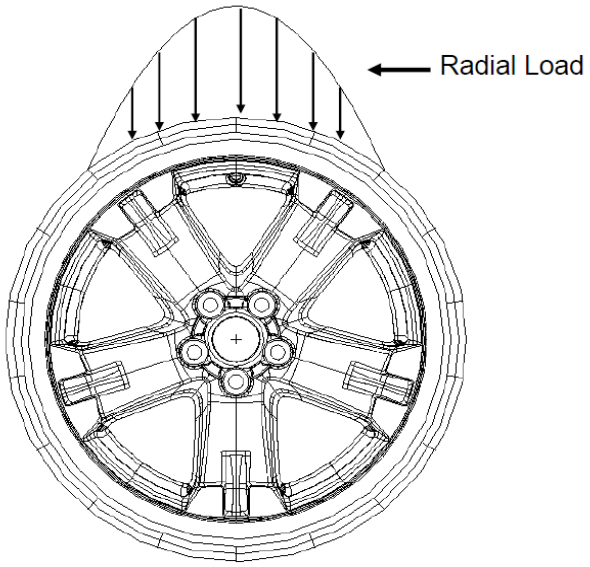

Figure 5-7. Radial loading as a cosine waveform

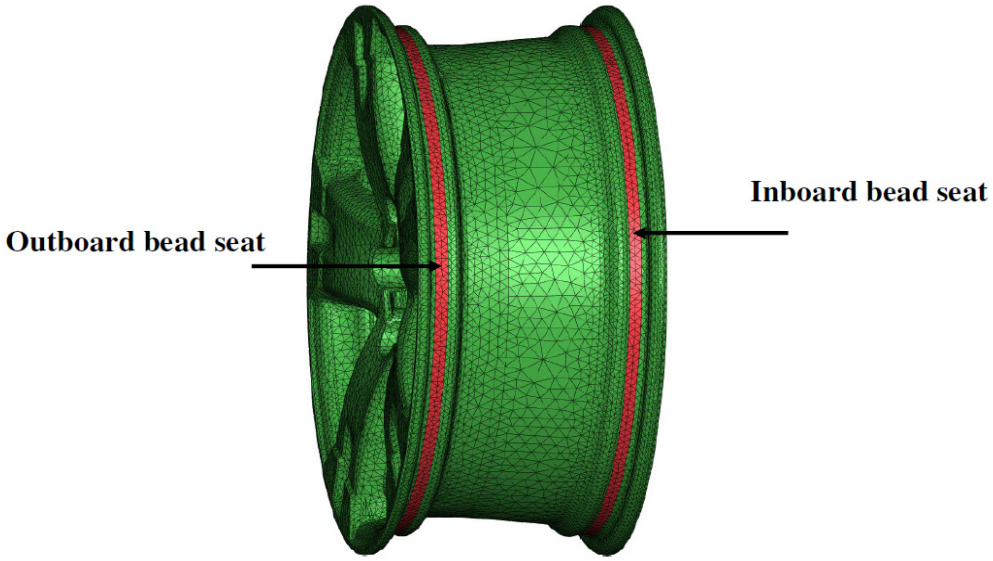

Figure 5-8. Bead area

To simulate the rotational motion of the wheel, the wheel must be rotated about its centre point. Rotating the meshed wheel requires that the coordinates of all the nodes in the wheel continuously change. Initially, this strategy was implemented in the model but it was found to be computationally intensive. To avoid excessive computational times, the wheel was held stationary and the radial load was rotated around the circumference of the wheel. A user subroutine was written in Fortran to vary the magnitude and location of the radial load based on step time. This method for simulating the test was much more efficient in terms of CPU time and accuracy.

Appendix B contains the input files for the two models.

6 Results and Discussion

6.1. Verification of the rim indentation finite element model

The rim indentation model was verified by comparing the modeling results with the rim indentation industrial tests performed at the wheel manufacturing company site. The rim indentation tests were explained in detail in Section 4.1.1 and the finite element modeling procedure of the same test has been explained in Section 5.1.

The load - displacement curves, shown in Figure 6-1, compare the model results with the measurements from the industrial rim indentation tests. During the industrial tests, two wheels were tested by applying 20.5 kN. Figure 6-1 shows that the modeling results are in general agreement with the industrial tests. Selected values from the load-displacement curves are compared in Table 6-1. The numerical values of deformation as well as the trend of curves exhibit a good correlation between the experiments and modeling results.

The load - displacement curves of the industrial tests coincide perfectly at the beginning (see dark blue and red curves in Figure 6-1), but at a displacement of 5 mm, the curves separate leading to a maximum difference of 0.55 mm at the peak load. When the load is decreased, the difference between the final permanent displacements of the two wheels was 0.49 mm. Although both the wheels were of the same type, the difference in the displacement curves for the two wheels can be attributed to stochastic differences and general variability in the wheel manufacturing process in factors such as melt chemistry, melt handling, quench conditions, etc.

The predicted load - displacement curve exhibits a similar slope to the industrial tests. However, differences between model results and industrial tests are apparent from the

beginning but the maximum displacement and final permanent displacement predictions by the model match very well with the industrial tests.

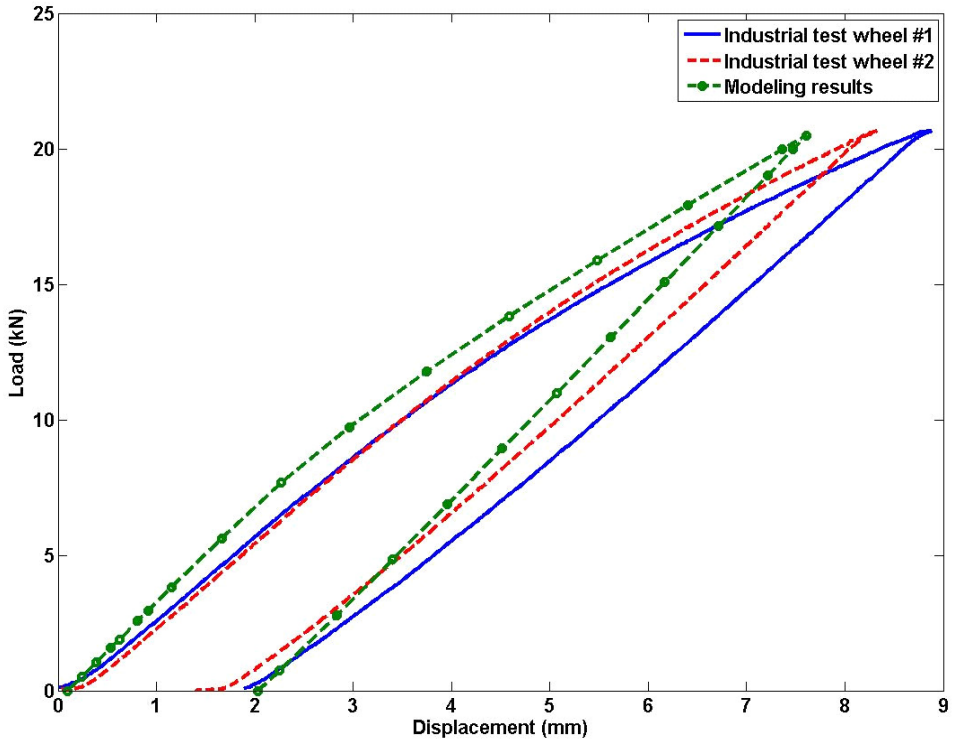

Figure 6-1. Comparison of modeling and experimental results

Table 6-1. Comparison of deformation

	Maximum displacement (mm)	Permanent displacement (mm)
Industrial test wheel #1	**8.87**	**1.89**
Industrial test wheel #2	**8.32**	**1.4**
Modeling results	**7.63**	**2.02**

The results from the rim indentation model are a source of information not available through traditional experimental work. To characterize the stress state of the wheel during rim indentation tests through traditional methods involves mounting strain gauges on the wheel, setting up a data acquisition system and analyzing the recorded data. The developed model provides more detailed information and the ability to analyze different scenarios easily. The plastic strain developed in the wheel is of particular importance for calculating the fatigue life of the wheel. The industrial tests only quantify the final permanent displacement sustained by the wheel and provide no quantification of the plastic strain distribution in the wheel.

The rim indentation model was used to estimate the amount of plastic strain sustained by the wheel. The maximum equivalent plastic strain generated in the wheel was 10% as shown in the Figure 6-2. As shown in Figure 6-2, the plastic strain is concentrated in a small zone on the inboard rim flange consistent with where the platen contacted the wheel. The red color on the figure shows the nodes / area which sustained the maximum amount of plastic strain. The majority of the wheel does not experience any plastic deformation, as shown by the dark blue color in the figure. The rim indentation model was used to estimate the range of pre-strain needed for the fatigue samples used in the laboratory scale experiments (refer Section 4.2.2.2). On the basis of the modeling results, the levels of pre-strain selected for the laboratory scale experiments were 5 and 10%.

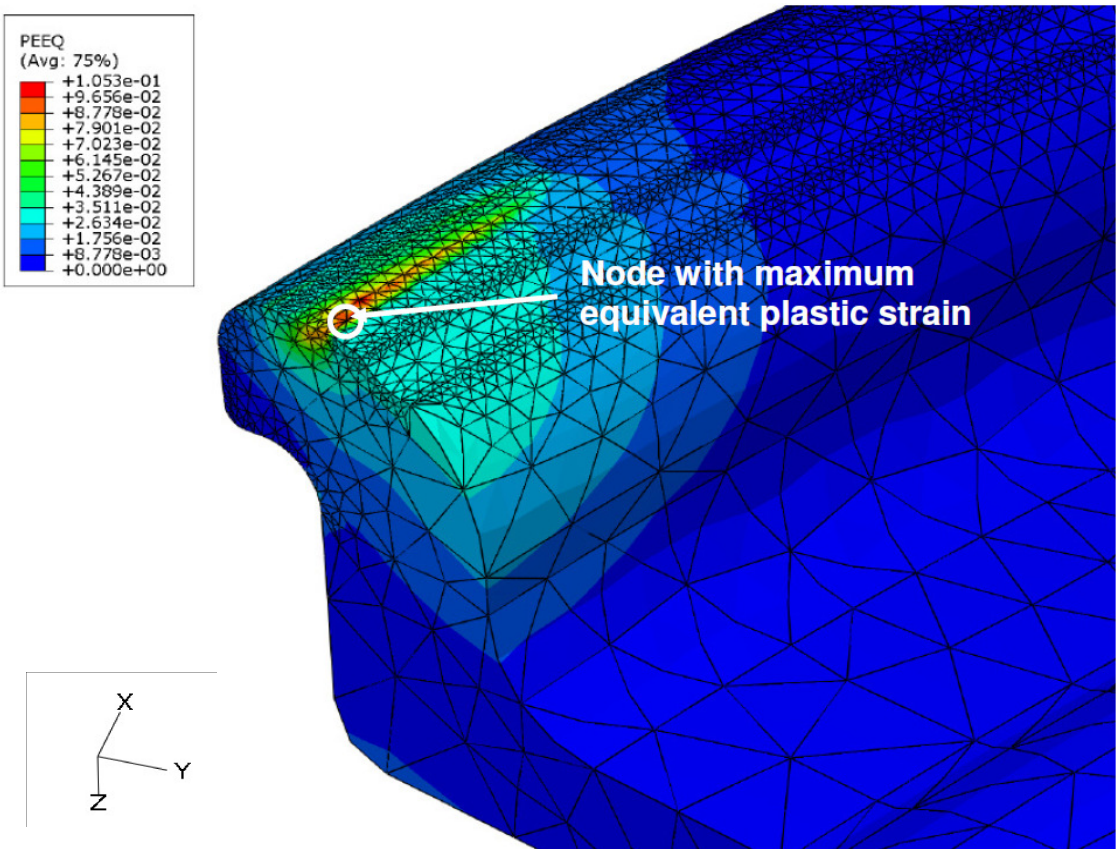

Figure 6-2. Predicted equivalent plastic strain following rim indentation testing

6.1.1. Contact simulation

The contact area and contact pressure are valuable pieces of information predicted by the rim indentation model. For wheel designs which do not pass the rim indentation test, this information can be used to modify the geometry of the rim flange of the wheel. Figure 6-3 shows the progressive change of contact area on the wheel surface during a rim indentation test. The platen has been removed from the figures to provide a better view of the contact area on the wheel surface. Figure 6-3 (a) shows the initial condition of the model where the platen is not in contact with the wheel. The blue surface in the figure shows the maximum area on the wheel which can come in contact with the platen and was defined as the slave surface in contact formulation. The rest of the surface of the wheel which will never come in contact with the platen is free of any contact properties defined for it to minimize computational expense. At the end of step 1, contact is established between the platen and the wheel as shown in Figure 6-3 (b) (small light blue surface). It should be noted that the contact zone established is a surface and not a point contact. After step 1, the load applied to the wheel is increased to the maximum test load. Figure 6-3 (c) shows the contact area on the wheel surface, when half of the load has been applied (~ 5 kN). Figure 6-3 (d) shows the contact area when the full load has been applied on the wheel. Figure 6-3 (e) shows the contact area when the load has been removed from the wheel.

The maximum contact pressure and area were observed at the maximum applied load of 10.25 kN. The maximum contact area on the wheel inboard flange surface was calculated to be 19.2 mm^2. As the maximum contact area involved in the rim indentation test is small, the contact pressure in the area is very high, reaching a maximum of 1100 MPa at certain nodes. This contact pressure is responsible for the deformation in the wheel.

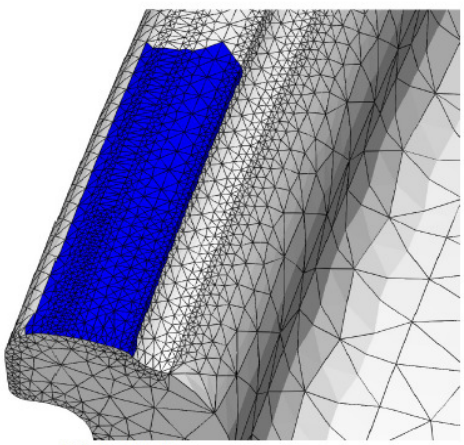

(a) Initial step- no contact

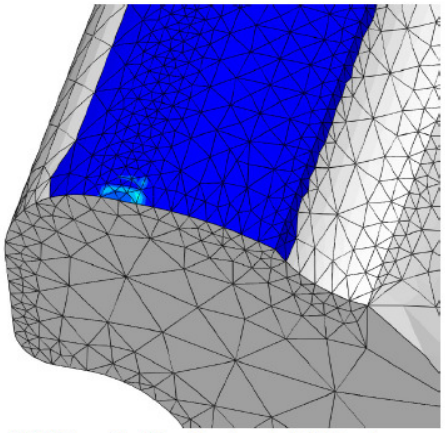

(b) Step 1- Contact established

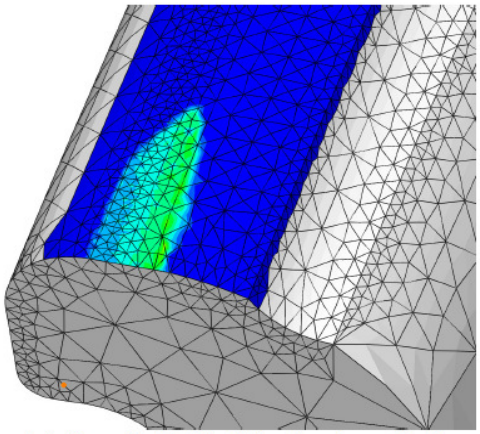

(c) Step 2- Half of the load applied (~5 KN)

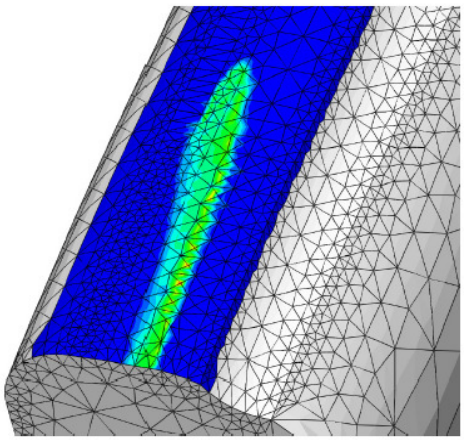

(d) Step 2- Full load applied (10.25 KN)

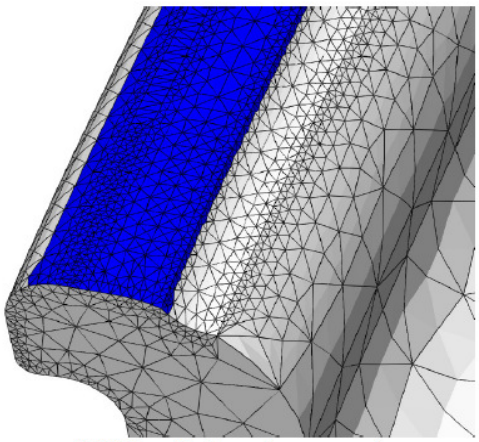

(e) Step 3- Load removed

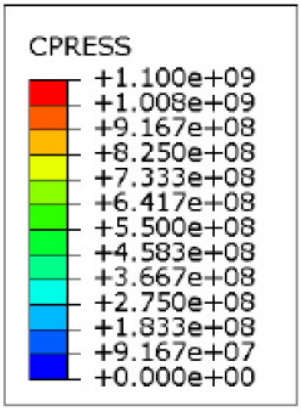

Figure 6-3. Contact pressure under platen predicted for rim indentation test

Figure 6-4 shows the stress state of a node in the contact region of the wheel. The node is marked in Figure 6-2. Prior to contact between the platen and the wheel, the stresses are zero. When contact is made and load is applied, a high compressive stress develops at the node. These high compressive stresses are shown as S-XX, S-YY and S-ZZ in the Figure 6-4 where XX, YY and ZZ represent circumferential, axial and radial directions, respectively. At the point of maximum load, all three of the stress components S-XX, S-YY and S-ZZ are above the yield strength and attain their maximum values of 567 MPa, 395 MPa and 666 MPa, respectively. The Von-Mises stress, shown as a dark blue curve in the graph, reaches a maximum of 328 MPa. This node sustained the highest amount of equivalent plastic strain of 10%. Following removal of the load, high tensile residual stresses in the circumferential direction remain at this location.

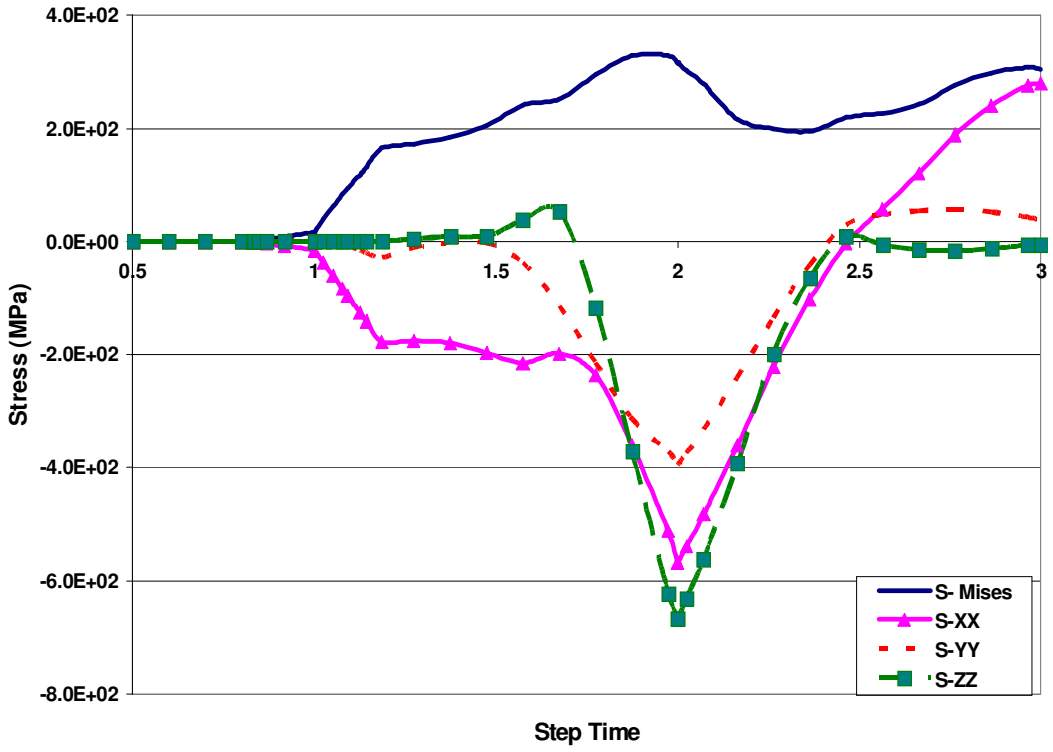

Figure 6-4. Stress state of a node in the contact region

6.1.2. Sensitivity analysis

The sensitivity of the rim indentation model to the parameters involved in the modeling process was analyzed to establish their effects. Two different parameters were analyzed:

6.1.2.1. Effect of flow stress of aluminum alloy A356

The rim indentation model was used to assess the sensitivity of the result to variations in the flow stress of the aluminum alloy. The results of the rim indentation tests performed for the wheel manufacturing company (dark blue and dashed red colored curves in the Figure 6-1), show considerable variability. Hence a sensitivity analysis was carried out on the rim indentation model to determine the effects of varied flow stress on the rim indentation test and explain the variability in curves in Figure 6-1. In this analysis, the flow stress was increased and decreased by 10% while Young's modulus and Poisson's ratio remained the same.

Table 6-2 shows the maximum displacement, permanent displacement and maximum equivalent plastic strain data for the two cases compared to the baseline result. As shown in the table, when the flow stress was increased by 10%, the amount of equivalent plastic strain (PEEQ) decreased to 9.5% (a decrease of 5% relative to the baseline) whereas it increased to 11.8% (an increase of 18% relative to the baseline) with the reduction in the flow stress. It can be concluded that a decrease in flow stress level has a more pronounced effect on the plastic strain sustained by the wheel.

The deformation sustained by the wheel was also analyzed. With an increase of 10% in the flow stress, both the maximum and permanent displacements decreased. The total deformation decreased to 7.29mm and plastic deformation decreased to 1.72mm, a decrease of 4.42% and 14.42% from the baseline displacement, respectively. On the other hand, with a 10% decrease in the flow stress, the maximum displacement increased to 8.02mm and permanent displacement increased to 2.41mm which is an increase of 5.11% and 19.3% from the baseline, respectively. The displacement levels also support that a decrease in flow stress has a more pronounced effect than an increase in flow stress.

Table 6-2. Comparison of rim indentation model results for different flow stress

Flow stress	Maximum displacement (mm)	Permanent displacement (mm)	PEEQ(%)
10% decreased	**8.02**	**2.41**	**11.8**
Baseline	**7.63**	**2.02**	**10**
10% increased	**7.29**	**1.72**	**9.5**

6.1.2.2. Effect of change in Young's modulus

Figure 6-1 showed the comparison of model predictions with the experimental results for the rim indentation test. Although, the peak and permanent displacements predicted by the model were within the acceptable range of the experiments, the slope of the curve predicted by the model differs appreciably from the experiments. It can be inferred from the difference in the curves that the stiffness of the aluminum wheel in the model is higher as compared to the experiments. Hence, a sensitivity analysis of the Young's modulus used in the rim indentation model was conducted. The Young's modulus (E) as determined by the tensile test (see Section 4.2.1) was decreased by 5% to 62.1 GPa and 10% 59.6 GPa. The flow strength data was unchanged. The rim indentation of the wheel was simulated with the changed material properties for the aluminum wheel.

Figure 6-5 shows the load versus displacement curves for the experiments and the rim indentation model's sensitivity to the Young's modulus. The blue colored solid line and the red colored dashed line are the experimental results. The dark green colored dashed line with circle markers is the displacement curve for the baseline rim indentation model with Young's modulus (E) = 66.25 GPa. The solid pink colored line with square markers is the rim displacement predicted by the indentation model with a 10% reduction in E (59.6 GPa). It can be clearly seen from the graph that the pink curve matches better with the experimental curves than the green curve. The slope of the pink curve is closer to the slope of the experimental curves. Also, the peak displacement predicted by the rim indentation model for the 10% reduced value of E, is between the peak displacements measured during the experiments. Finally, it should also be noted that the permanent displacement estimated for

the 10% reduced value of E is higher than the permanent displacement values of the experiments and the baseline model.

Table 6-3 shows the numerical values of the peak and permanent displacements as predicted by the rim indentation model compared with the experiments. The baseline displacement predictions of peak and permanent displacements, i.e. 7.63 and 2.02 mm, respectively correspond to a Young's modulus of 66.25 GPa. When the Young's modulus was decreased by 5% to 62.1 GPa, the peak and permanent displacements increased to 7.88 and 2.06 mm, an increase of 3.27% and 1.9% respectively. Similarly, when the Young's modulus was decreased by 10% to 59.6 GPa, the peak and permanent displacements increased to 8.36 and 2.14 mm, an increase of 9.56% and 5.9% respectively.

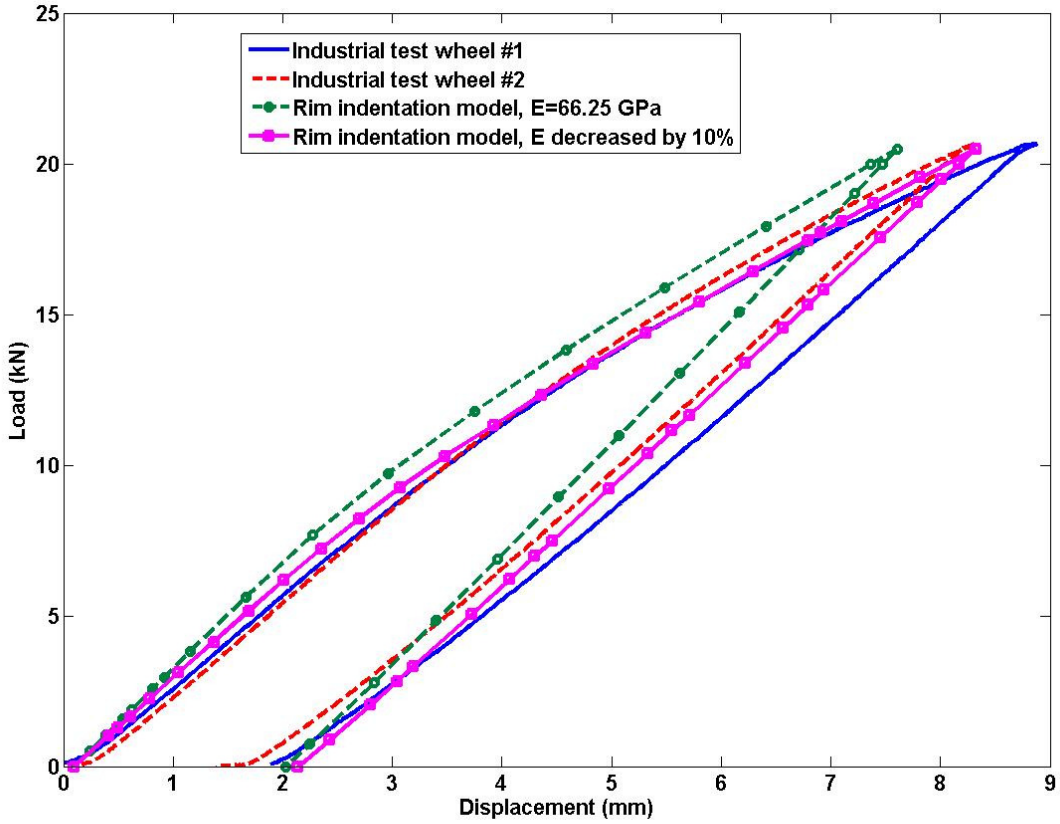

Figure 6-5. Comparison of sensitivity analysis results for model with different values of E

With the 10% decreased Young's modulus, the peak displacement of 8.36 mm was in between the peak displacements of 8.32 and 8.87 mm, as determined through experiments but the permanent displacement of 2.14 mm was more than the permanent displacements, 1.89 and 1.4 mm, established through experiments.

Table 6-3. Comparison of rim deformation sensitivity analysis for variation in Young's modulus

	Maximum displacement (mm)	**Permanent displacement (mm)**
Industrial test wheel #1	**8.87**	**1.89**
Industrial test wheel #2	**8.32**	**1.4**
Model E=66.25 GPa	**7.63**	**2.02**
Model E=62.1 GPa	**7.88**	**2.06**
Model E=59.6 GPa	**8.36**	**2.14**

After further investigation, an improved fit between the model results and the experiments was found when *E* was decreased by 15% to 56.3 GPa and the flow strength values were increased by 10%, keeping the plastic strain unchanged. Figure 6-6 shows the displacement prediction with the model in solid orange color line with circular markers and measured during the experiments in solid blue and dashed red lines. The peak displacement predicted with the rim indentation model was 8.38 mm and the permanent displacement was 1.87 mm, both of which lie in between the experimental data: peak displacement between 8.32 and 8.87mm and permanent displacement between 1.4 and 1.89mm.

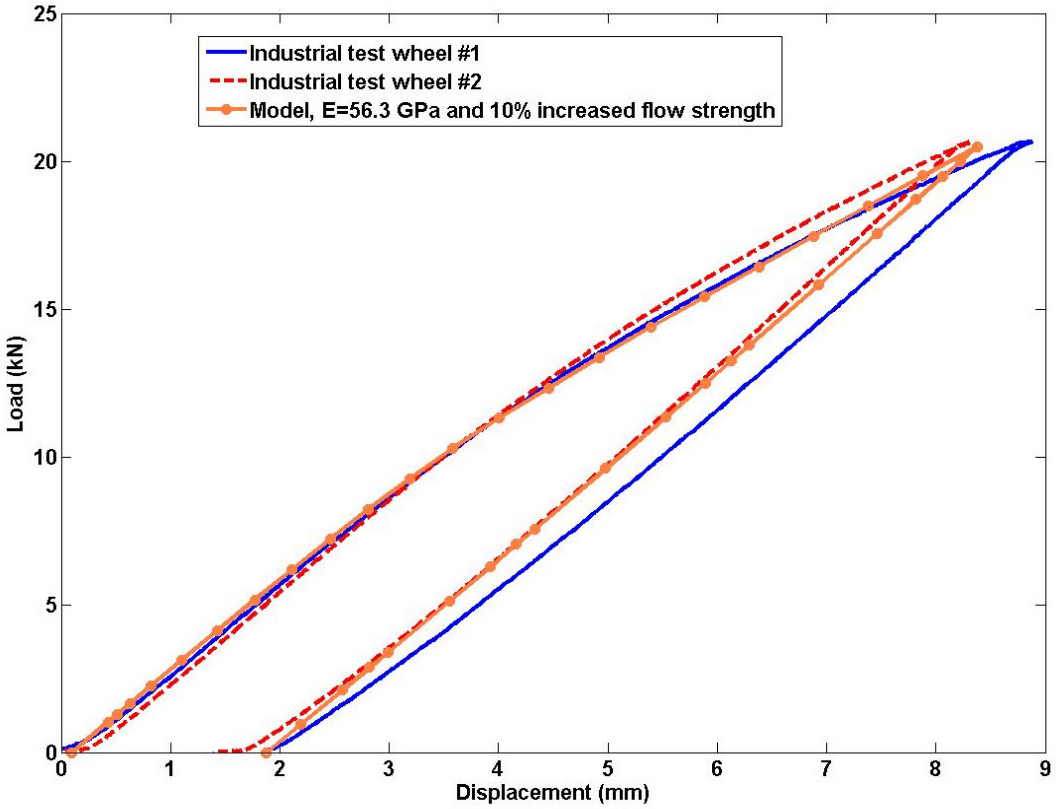

Figure 6-6. Sensitivity analysis with the rim indentation model for variation in E and flow strength

6.1.2.3. Numerical sensitivity

The sensitivity of the rim indentation model to element type was assessed as a measure of the numerical sensitivity. The model was run with 4-node linear tetrahedral (C3D4) elements by removing the mid-side nodes on each of the original 10-node quadratic tetrahedral elements. All the other conditions such as material properties and the contact description were the same for both the models. Figure 6-7 shows the comparison of numerical model results i.e. 4-node tetrahedral elements and 10-node tetrahedral elements with the experimental results. The load - displacement predictions are very sensitive to the element type.

The size of the elements in the contact region also effect the accuracy of results. Fine mesh with smaller element size as compared to a coarser mesh results in a better distribution of contact pressure over the contact area. Finer mesh is also recommended to avoid situations such as, a node from the master surface penetrating into the salve surface.

In general, second order elements with finer mesh in the contact region should be used to model contact behavior between two bodies.

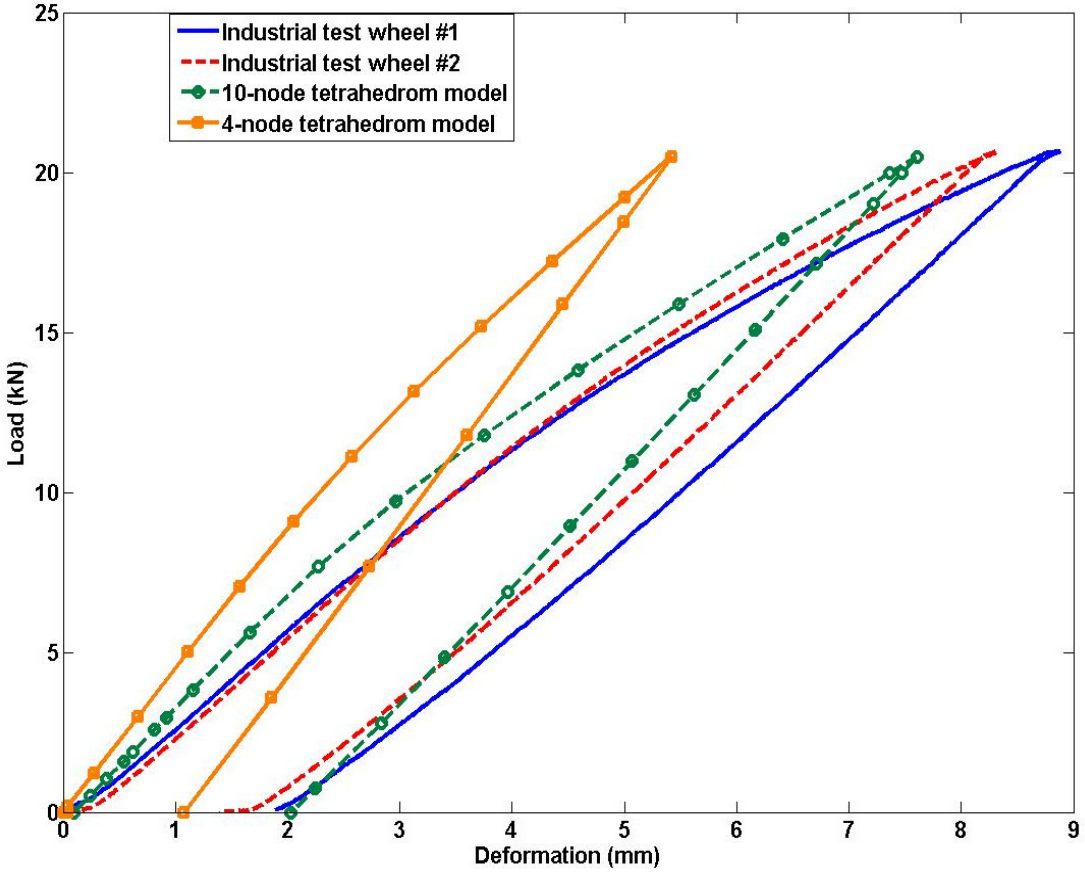

Figure 6-7. Comparison of numerical models

6.2. Verification of the radial fatigue test model

The radial fatigue test model was verified by comparing the simulation results with the industrial tests done on a finished wheel. The industrial tests were performed to determine the strain state of the wheel during the radial fatigue test. The test setup, instrumentation details and strain curves were discussed in Section 4.1.2. The loads, boundary conditions and simulation steps required to model this test were discussed in detail in Section 5.2.

Figure 6-8 shows a comparison of the strain measurements for strain gauge 1 to the predicted elastic strain from a node in a corresponding location from the radial fatigue model. The location of strain gauge 1 on the wheel is on the spoke region (see Figure 4-4). In Figure 6-5, the solid blue line shows the experimental measurements whereas the dashed red line shows the simulation results for an applied radial load of 15.2 kN. The strain curves shown for the model results are for two complete rotations of the wheel whereas the experimental strain data was recorded for just under two rotations of the wheel limited by the capacity of the DAQ system. In Figure 6-8, the variation of strain between markers A and E represents the strain cycle at this location for one complete rotation of the wheel. When the wheel rotates, the cycle from A to E repeats itself, making the strain repetitive in nature. At the markers A and E, strain gauge 1 is directly under the radial load i.e. centre of the contact patch. Markers B, C and D are placed at points on the graph equivalent to 90°, 180° and 270° from point A. The maximum tensile strain measured at this location was 6.85 x 10-4 during the experiments. The applied radial load of 15.2 kN was applied in the model to duplicate the experimental loading conditions.

It is evident from the strain curves of Figure 6-8 that the numerical values of the strain predicted with the radial fatigue model for a radial load of 15.2 kN are low as compared to the experimental strain measurements. Although, the strain values are different, the trends of the strain curves for both the experiments and modeling results are the same. The qualitative comparison of the strain curves confirms the correctness of the basic modeling methodology. In an effort to achieve a more quantitative fit, the radial load was increased. In Figure 6-8, the curves in dark green and orange color show the strain variation at the same node with increased radial loads. As the radial load was increased, the strain amplitude, maximum and minimum strain values increased and came closer to the experiments.

Although, there is a scope for further increase in the radial load but the results with the radial load of 23 kN were accepted based on the fit of the curve for gauge 13 located at the inboard flange location which is critical to this research work.

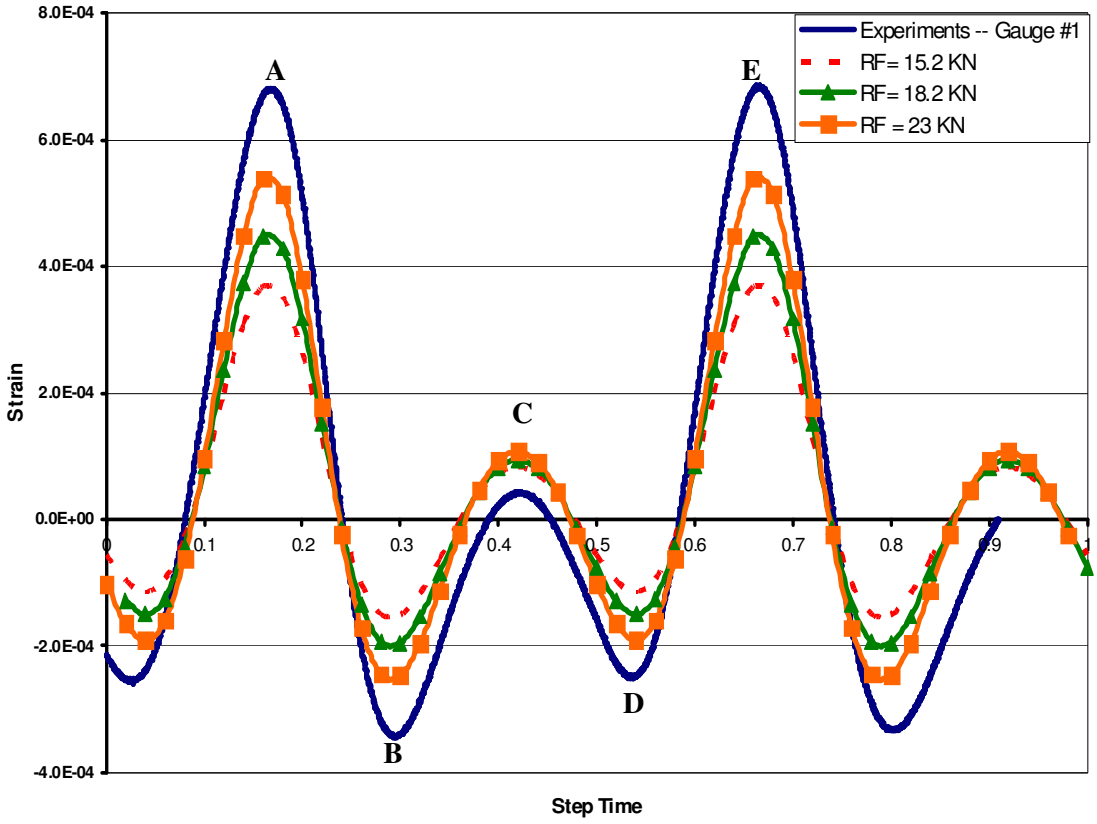

Figure 6-8. Comparison of predicted and measured strains for gauge 1 during radial fatigue test

Similarly, strain measurements for gauges 7, 10, 13 and 16 (refer to Figure 4-4, Figure 4-5 and Figure 4-6) were compared to the strain estimated by the radial fatigue model.

Figure 6-9 shows a comparison of the strain gauge 7 measurements with the strain predicted by the radial fatigue model for a node in the same location on the wheel. Strain curves for radial loads of 15.2, 18.2 and 23 kN are plotted. As with strain gauge 1, the pre-

dicted strains show the same trends. At this location, the amplitude of the predicted strain variation matches the amplitude of the measured strains for a radial load of 23 kN.

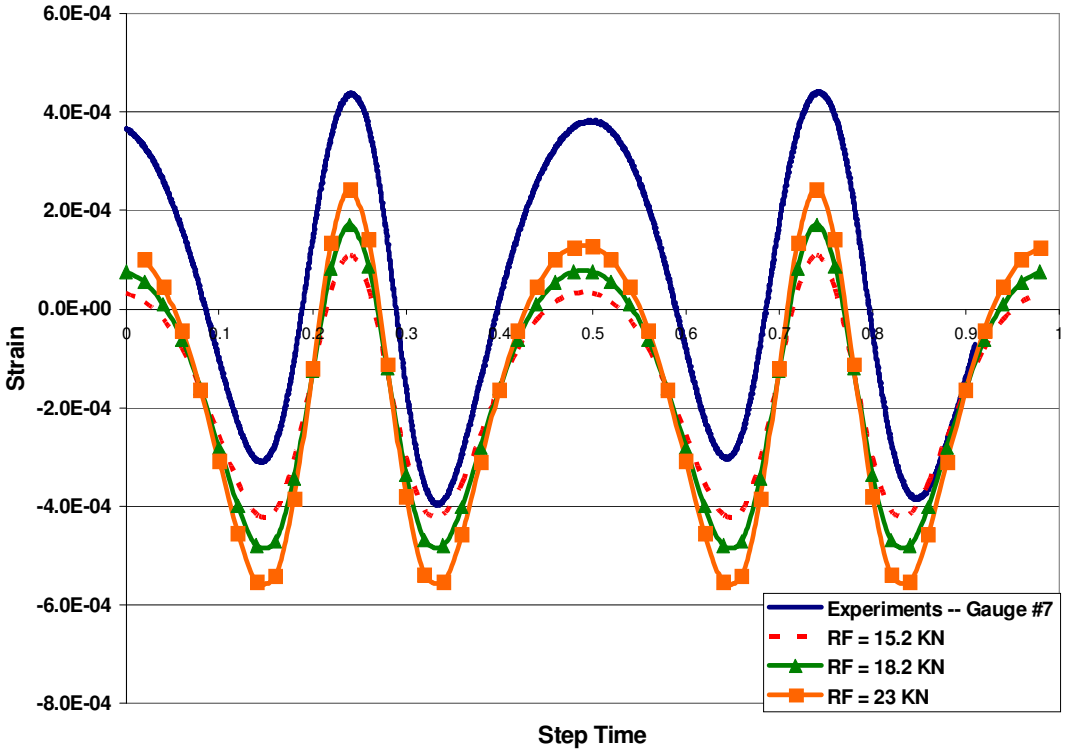

Figure 6-9. Comparison of predicted and measured strains for gauge 7 during radial fatigue test

Figure 6-10 shows a comparison of the experimental measurements for strain gauge 10 with the strain estimated from the radial fatigue model. A similar trend can be seen in this figure as in Figure 6-8 and 6-7 where the radial load 15.2 kN resulted in very low strains and as the radial load was increased, the predicted strains approached the experimentally measured strains.

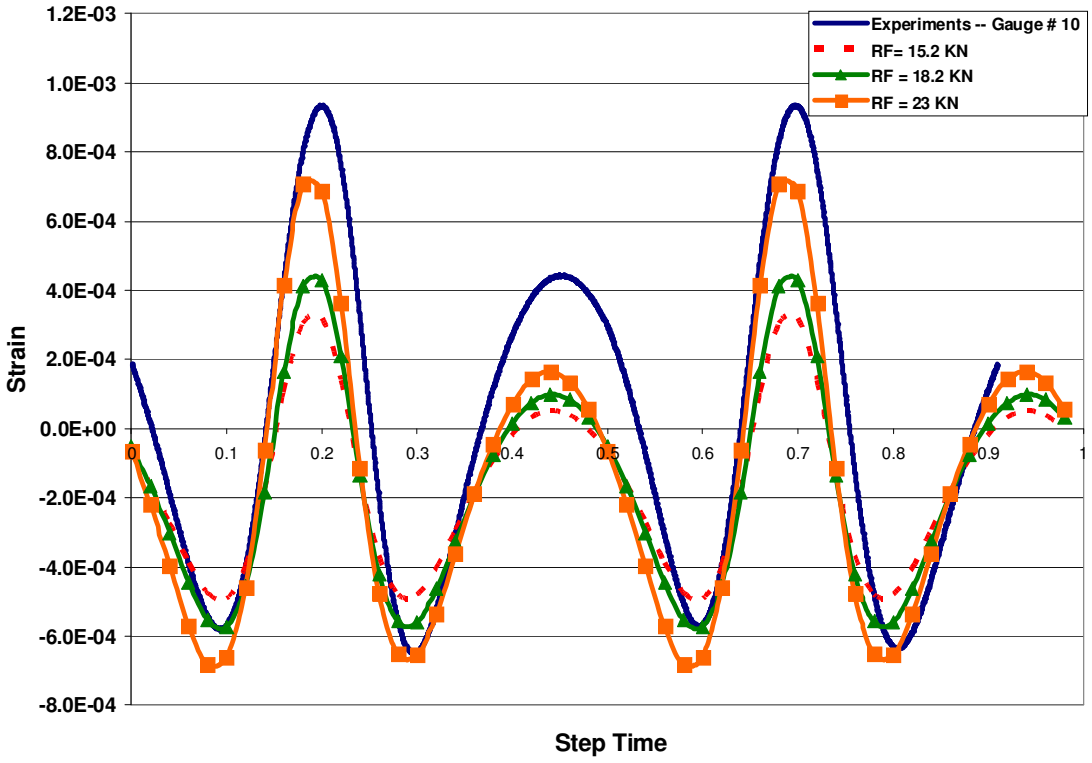

Figure 6-10. Comparison of predicted and measured strains for gauge 10 during radial fatigue test

Figure 6-11 shows the strain comparison for strain gauge 13 (refer to Figure 4-5) measurements with the radial fatigue model. This strain gauge was strategically located at the inboard rim flange where the rim is deformed in the rim indentation test. As mentioned in Section 4.1.1.1, fatigue failure for rim indented wheels was observed at this location, accurate prediction of the strains in this area is very critical.

It can be clearly seen in Figure 6-11, strain predicted by the radial fatigue test model at gauge 13 for a radial load of 23 kN matched with the experiments better than other radial loads. As the focus of this research work is to predict the fatigue life of rim indented wheels, the strain characteristics at the inboard rim flange location are of paramount importance. Based on this fit of the curve, it can be inferred that the radial fatigue test model with a load of 23 kN gives: i) the exact match for the maximum strain between the model and

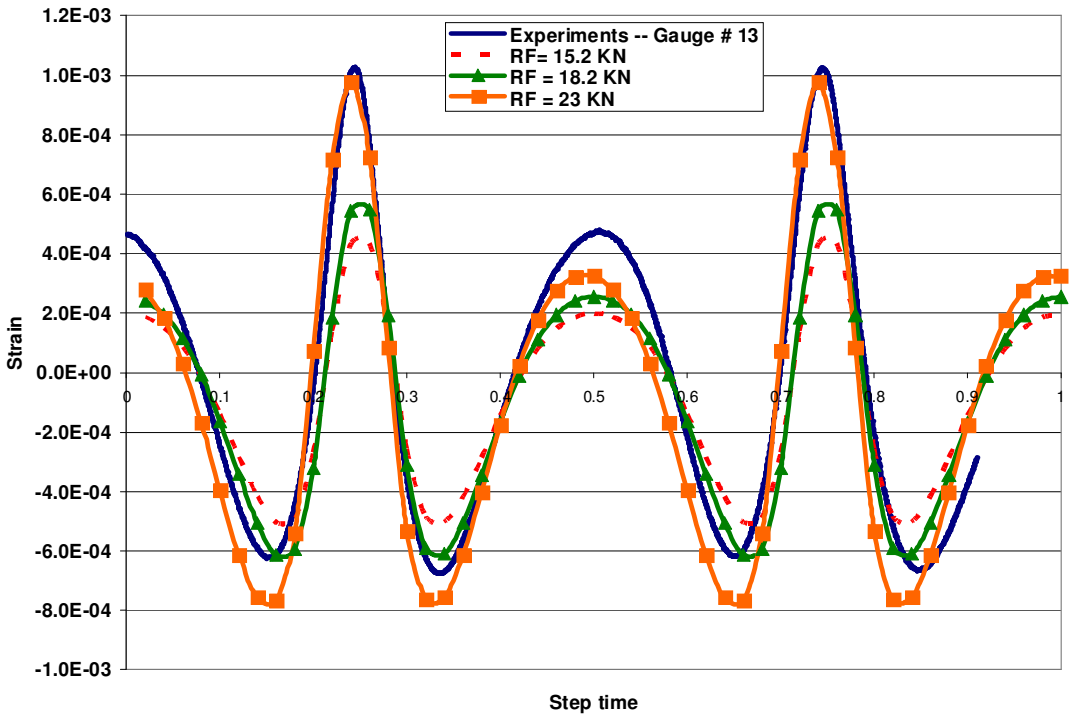

Figure 6-11. Comparison of predicted and measured strains for gauge 13 during radial fatigue test

the experiments and ii) reliable estimations of the strain state at the inboard rim flange area on the wheel can be made.

In the fatigue model developed to estimate the fatigue life of wheels (see Section 4.2.2), the maximum strain is one of the parameters. Hence, with a radial load of 23 kN, the radial fatigue test model provides a good estimate of the maximum strain state at the inboard flange location of the wheel. Hence, the radial fatigue test model with a radial load of 23 kN was accepted.

Figure 6-12 shows the strain comparison for gauge 16. The numerical values predicted by the radial fatigue model do not match with the experimental calculations but the trend of the curves match. This strain gauge is placed on the spoke region of the wheel (refer to Figure 4-6). The amplitude strain of the measurements matches closely with the radial fatigue model predictions with 23 kN load.

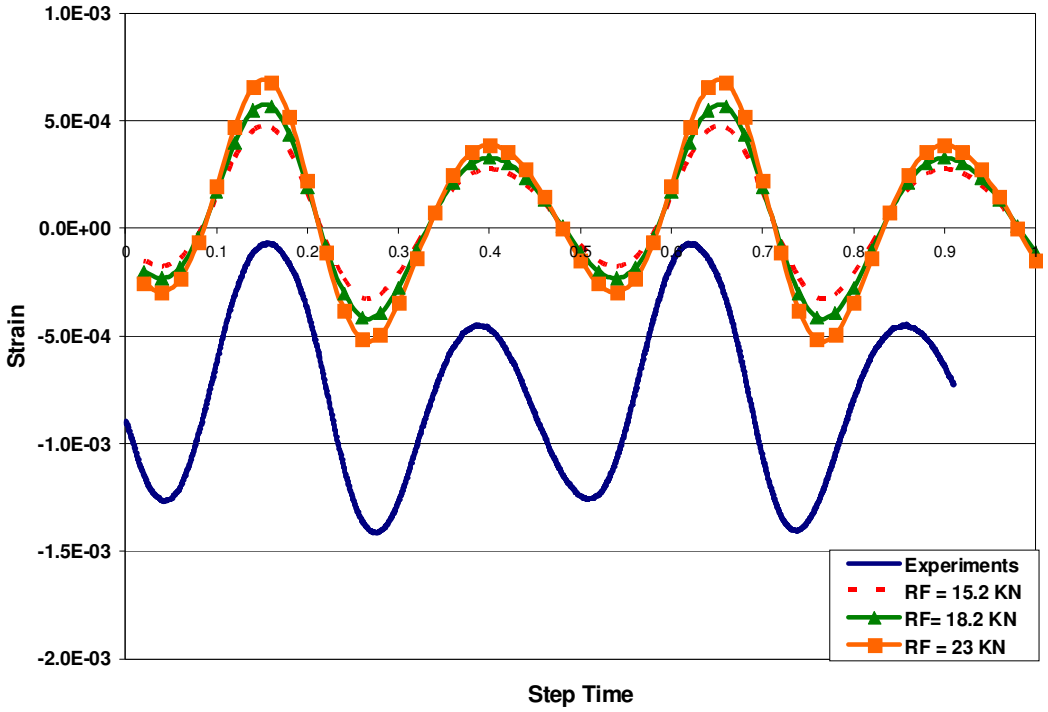

Figure 6-12. Comparison of predicted and measured strains for gauge 16 during radial fatigue test

6.2.1. Sensitivity analysis

A sensitivity analysis was performed on the radial fatigue test model for the wheel to establish the effects changes in the material properties of the wheel, specifically Young's modulus on the strain state of the wheel.

6.2.1.1. Effect of change in Young's modulus

As discussed earlier, the Young's modulus used in the radial fatigue test model was determined through a tensile test to be 66.25 GPa, it was decreased by 5% to 62.1 GPa and 10% to 59.6 GPa, to estimate the change in strain state of the wheel during the radial fatigue test with the change in Young's modulus.

Figure 6-13 shows the change in strain state of a node present at the inboard flange location on the wheel with variation in Young's modulus. The radial load applied on the wheel was 23 kN. The solid orange colored line shows the strain state of the node with Young's modulus equal to 66.25 GPa, the red dashed curve shows the strain state of the node with Young's modulus decreased by 5% to 62.1 GPa and the solid blue line with square markers shows the strain state of the node for Young's modulus decreased by 10% to 59.6GPa. As Young's modulus decreases, the maximum and minimum strains increase. With a 5% decrease in the Young's modulus, the maximum strain increased by 5.33% and with the 10% decrease in the modulus, the maximum strain increased by 13.2%.

As discussed in Section 6.1.2.2, when the Young's modulus was decreased by 15% to 56.3 GPa, the rim indentation model matched well with the experiments. Hence, for the radial fatigue test model, the Young's modulus was reduced to 56.3 GPa, as a result, the radial load required to produce the same strains measured during the experiments decreased. For the strain gauge 13 located at the inboard flange, the load may be was reduced to 20.5 kN. The strain comparison has been done with the strain gauge 13 because it is placed at a critical location on the wheel, for this research work. As during the rim indentation test, the wheel is deformed at the inboard flange location and has been observed to fail at the same location during the radial fatigue test following rim indentation, the correct strain estimation for gauge 13 were required.

In Section 6.2, it was established that 23 kN radial load was required in the radial fatigue test model to match with the experiments performed at 15.2 kN radial load, a difference of 50.3%. After modifying the material properties, the radial load required to match the experimental data was decreased to 20.5 kN which matches better with the applied load of 15.2 kN.

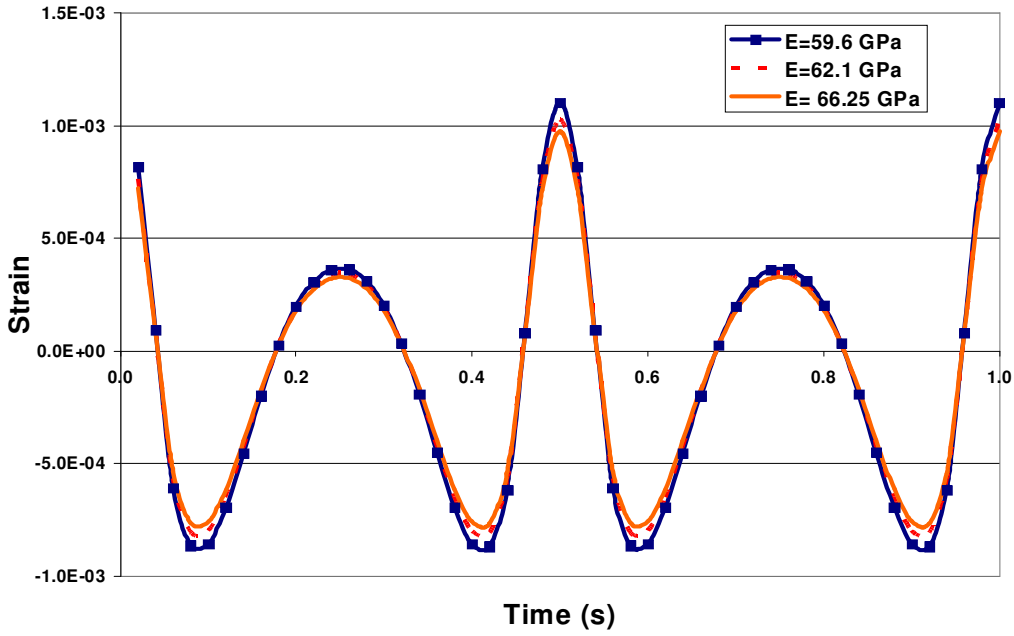

Figure 6-13. Strain state of a node present at the inboard flange with variation in Young's modulus

6.2.2. Summary

The radial fatigue test model was developed to predict the stress and strain characteristics of the wheel during the radial fatigue test. The trend of strain curves developed at 15.2 kN radial load matched with the strain measurements but the numerical values did not match. The radial fatigue load was increased to 23 kN, in order to achieve the best match in terms of strain amplitude and numerical values for the strain gauge placed at the inboard rim flange location. As the inboard rim flange is the critical location in this research project, the radial fatigue model with 23 kN was accepted. With the sensitivity analysis it was established that with the Young's modulus decreased to 56.3 GPa, the radial load required in the radial fatigue test model decreased to 20.5 kN.

6.3. Fatigue life prediction

One of the main objectives of this research is to predict the fatigue life of rim indented wheels during the radial fatigue test. This objective may be accomplished by combining the validated models of rim indentation and radial fatigue testing with the empirical equation for fatigue life of pre-strained cast aluminum alloys developed in Section 4.2.2.4. In this section, the integration of the models for rim indentation, radial fatigue, quenching and machining with the fatigue life relationship will be described and used to predict the fatigue life of rim indented wheels.

Estey [1] developed a thermo-mechanical model to predict the stress state of a wheel after the quench process which is part of the T6 heat treatment to which all wheels are subjected. This model was used in conjunction with a technique developed by Li [32] to estimate the effects of the material removal that occurs during machining on the stress state of a wheel. The quench process is performed on wheels that have been rough trimmed following casting, but not machined to the final geometry. Thus, the trimmed wheel geometry was required for this analysis.

The trimmed wheel geometry obtained from the wheel manufacturing company was meshed with 149,605 nodes arranged in 669,070 4-node linear tetrahedral (C3D4) elements. The C3D4 elements were used to reduce the computational time as compared to 10-node quadratic tetrahedral elements required to simulate the rim indentation and radial fatigue processes. For the work done by Estey [1] and Li [32], 4-node tetrahedral elements were shown to perform adequately, especially because their work did not involve any contact simulation. To assist the reader in understanding the quenching and machining model and their integration into the overall model, a brief description of them is provided next. It should be emphasized that the techniques developed by Estey [1] and Li [32] have been used in this research work without any modification, hence these models were not discussed in the model development section in Chapter 5.

6.3.1. Thermal model

The thermal modeling technique developed by Estey [1] was used to predict the temperature response of the wheel during the quench process. The quench process is part of the T6 heat treatment process which follows a solutionizing step where the wheel is held at a temperature of 540°C to dissolve Magnesium-based precipitates. During the quench process, the wheel is rapidly cooled in a water bath to obtain a supersaturated solid solution state. The quench process was modeled by applying the temperature dependent heat transfer coefficient boundary condition reported by Estey [1] to the exposed surface of the wheel. The quench process results in high thermal gradients at raised temperatures which induces stress and plastic deformation in the wheel.

Two heat transfer processes take place simultaneously, i.e. convective heat transfer between the wheel and the water and heat conduction within the wheel. The surface of the wheel, which comes in contact with the water first, is most effectively cooled, whereas the core region of the wheel takes more time to cool due to conduction. The predicted temperature variations with time for surface, core and flange nodes are shown in Figure 6-14. The temperature variation shown in solid blue line is for a surface node located on the spoke region of the wheel. As shown in Figure 6-14, from 0 to 2s, the surface node has a faster cooling rate than the other two nodes. This can be attributed to the fact that only the surface node comes in direct contact with water. After 2s, the cooling rate slows down because of two reasons; firstly, as the surface temperature is reduced, the difference in temperatures between the water and the wheel surface is reduced, resulting in a lower heat transfer rate and secondly, due to heat transfer from the core of the spoke to the surface. As a result, the surface node on the spoke maintains a temperature which is determined by the balance of convection and conduction heat transfer. The green dash-dot curve represents the temperature state of a node present on the flange of the wheel. As this node is not in direct contact with the water, the initial cooling rate is low but due to the small thickness of the flange, after 2s the cooling rate increases. The core node is surrounded by material on all sides and must rely on the conduction to the surface of the wheel for the cooling. It has the slowest cooling rate among the three nodes shown in Figure 6-14.

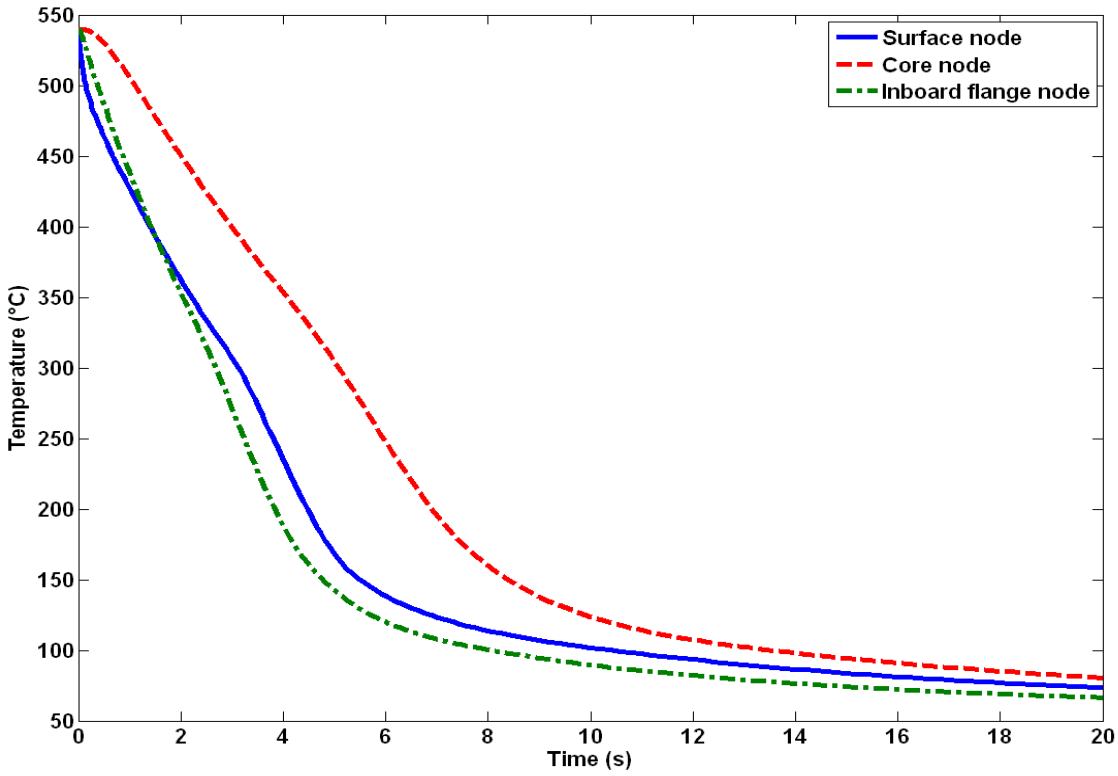

Figure 6-14. Temperature variation during quench process

6.3.2. Residual stress model

The mechanical model, also developed by Estey [1], was used to estimate the residual stress state in the wheel after the quench process. The results from the thermal model discussed in Section 6.3.1 were used as an input in the residual stress model providing the temperature variation of the wheel during the quench process. The flow stress as a function of temperature, strain and strain rate were acquired from Estey's [1] work. The coefficient of expansion as a function of temperature was also obtained from Estey [1]. Boundary conditions were used to restrict rigid body motion of the wheel. These included constraining the nodes on the symmetry plane of the wheel to remain on this plane as well as constraining a number of nodes on the inboard rim flange to move in the plane normal to the symmetry plane of the wheel [1].

Approximately 1 mm of material is removed during machining from the inner and outer surfaces of the rim flange and the back of the spokes which results in a re-distribution of the residual stresses in the wheel. During the quench process, the surface of the wheel is placed in a state of compression whereas the core region of the wheel is in tension. Upon machining, interior locations that were once in a state of tension may be exposed and the resulting redistribution of stress may place these locations in a state of compression. A compressive stress state on the wheel surface can retard fatigue crack growth whereas the tensile stress in the core region can aid the propagation of fatigue cracks.

The technique developed by Li [32] to estimate the effect of material removal during machining on the final residual stress state of a finished wheel was employed in this research. This required a single modeling step where the elements representing the material cut during machining were removed from the analysis. The boundary conditions were also changed to restrict the motion in all the directions of the nodes in the bolt holes [32].

Figure 6-15 shows the stress state of a finished wheel i.e. after the quench, air cool and machining processes. The figure shows that compressive stresses are developed on the surface whereas tensile stresses develop at the interior locations. It may also be observed that thicker regions in the spoke developed higher tensile stresses compared to the thinner sections, where compressive stresses may develop. The complex geometry near the bolt holes

developed high tensile stresses. The rim surface connected to the spoke region of the wheel developed tensile stress contrary to the compressive stress developed on the rest of the surface.

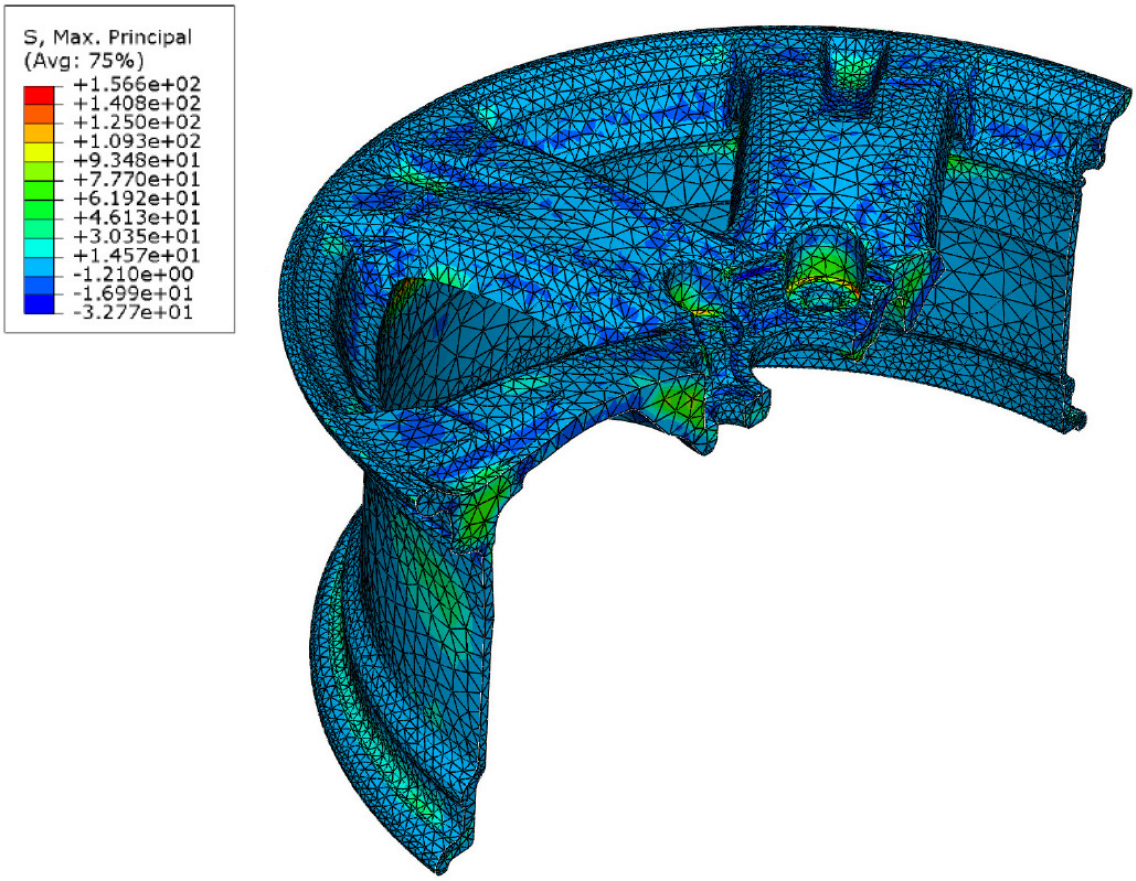

Figure 6-15. Stress state of the wheel after quench, air cool and machining processes

As the focus of this research project is the response of the inboard flange area of the wheel, the stress state of a node (see Figure 6-16) on the inboard flange is shown in Figure 6-17. As shown in Figure 6-17, tensile stresses (S-XX, S-YY and S-ZZ) are developed at this location during the quench process (t ≤ 20s). Small changes in the stress level are observed during the air cool down following quenching (t = 20 - 30s). During the machining step (t =30 - 35s), the node which was in the interior of the wheel is now on the surface of the finished wheel. The re-distribution of stress takes place and the node develops a residual compressive stress. It will be discussed later in the chapter but out of the three stresses, S-XX, S-YY and S-ZZ (directions shown in Figure 6-16), S-XX which is in the normal direction of the plane shown in Figure 6-16 plays the most important role in fatigue life estimation. The stress values at the node are -28, -15 and -1 MPa in the directions X, Y and Z respectively.

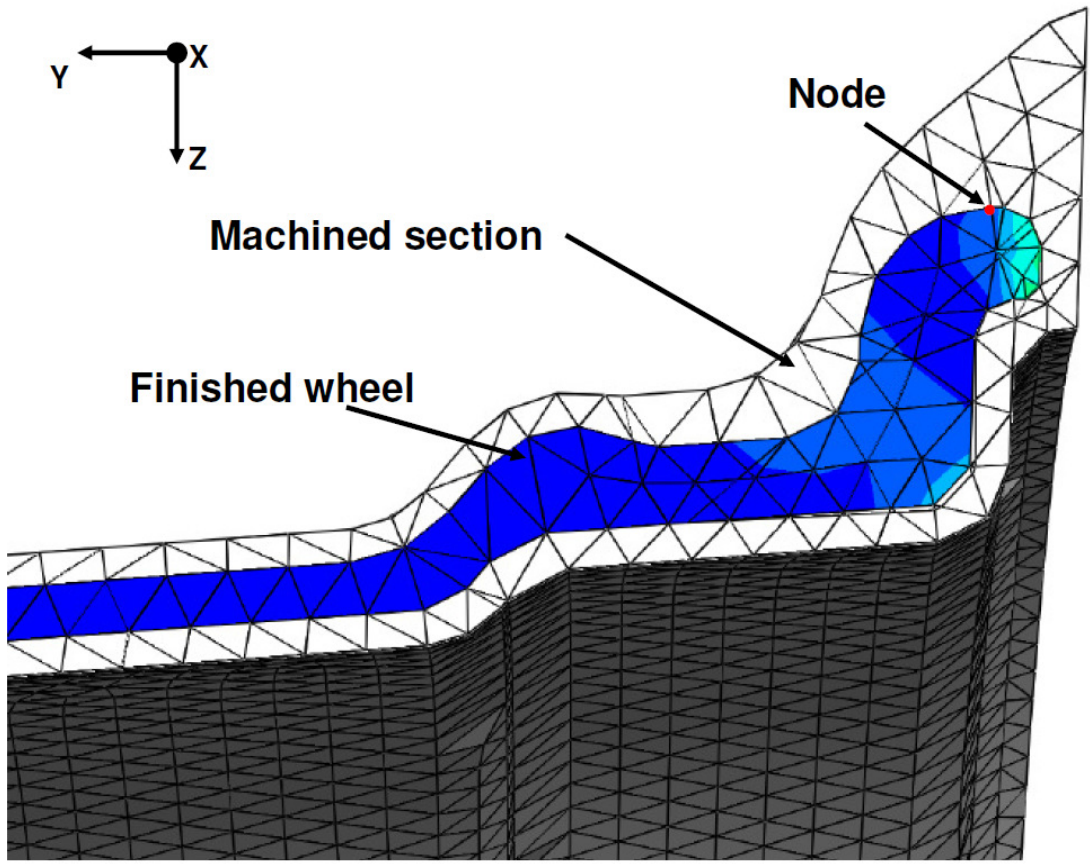

Figure 6-16. Node at inboard flange

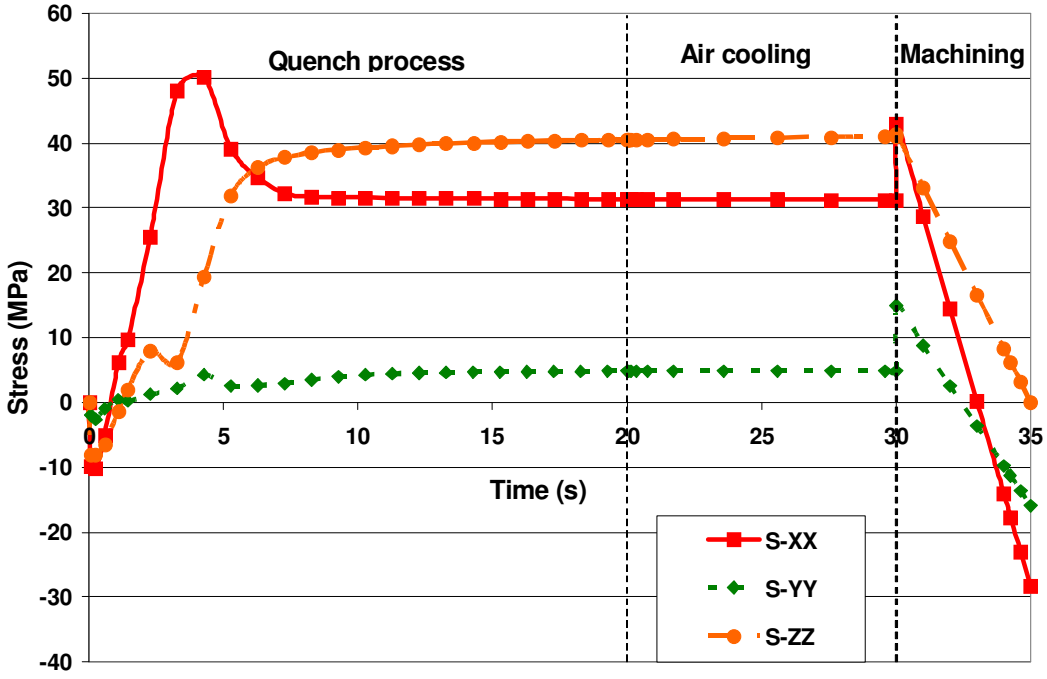

Figure 6-17. Stress state of a node on the inboard flange

The stresses developed in the wheel model used in this research project were compared with the works of Li [32]. The residual stresses developed were in accordance with Li's estimations for a different wheel geometry, but similar process conditions. According to Li [32], the highest tensile stresses developed in the thick spoke region connected to the rim of the wheel, were around 90 MPa. Similar values of 70 - 90 MPa were calculated for the wheel geometry used in this research project. Li [32] also predicted compressive stresses at the surface of the wheel with a maximum stress of -30 MPa, which is similar to the value of -32 MPa calculated in this research project.

The elements used in the model to predict the residual stress state of the wheel after the quench and machining processes were linear tetrahedral (C3D4). These elements provide good performance for the thermal-stress analysis, but were found to inaccurately describe the contact conditions occurring in the rim indentation test. Thus, prior to running the rim indentation model, the residual stress state of the wheel was mapped to the wheel mesh

formed with 10-node tetrahedral elements (C3D10) using a utility routine available in ABAQUS.

6.3.3. Summary

The residual stress state developed in the wheel during the quench and machining processes affects the in-service stress state. As discussed, compressive stresses are known to retard the fatigue crack growth rate whereas the tensile stresses can increase the fatigue crack propagation rate. Thus an estimation of the residual stress needs to be included when studying fatigue crack growth behavior.

6.3.4. Rim indentation model including residual stress

The predicted residual stress state of the wheel after the quench and machining processes was used as an initial condition for the rim indentation model. This was added as an initial step of 1 second duration to the rim indentation model discussed in Section 6.3.2. Similar to the other steps in this model, the duration of this step is arbitrarily set at 1 s since the interpolation process to import the residual stress results is independent of time. Figure 6-18 shows the predicted load versus deformation plot for the rim indentation model with and without the initial residual stress distribution compared with the industrial experiments. The deformation curve (pink solid line with square markers) for rim indentation with residual stress state coincides with the deformation curve (dashed green with round markers) for rim indentation without the residual stress.

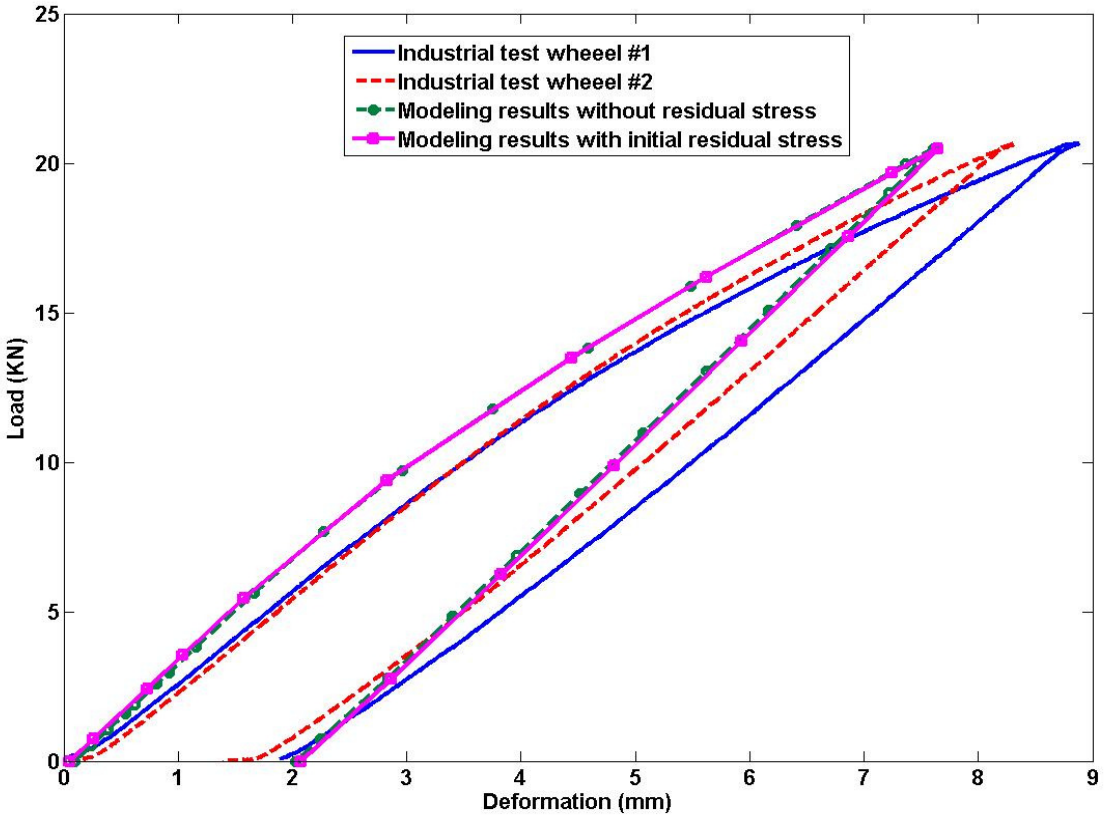

Figure 6-18. Comparison of modeling results with and without residual stress

A comparisons of the numerical values of displacement from the rim indentation model with and without residual stress are presented in Table 6-4. The initial residual stress does not affect the displacement values for the modeling results, such a behavior may be attributed to the low initial residual stress and strain values present in the inboard rim flange location as discussed in Section 6.3.2 in relation to the node shown in Figure 6-16.

Table 6-4. Comparison of displacement for the rim indentation test

	Maximum displacement (mm)	**Permanent displacement (mm)**
Industrial test wheel #1	**8.87**	**1.89**
Industrial test wheel #2	**8.32**	**1.4**
Modeling results - NO initial residual stress	**7.63**	**2.02**
Modeling results with residual stress	**7.64**	**2.07**

Figure 6-19 shows the evolution of stress at a node on the surface in the contact region where the highest plastic deformation occurs. During the initial step (0 - 1s), the residual stress state predicted with the model of the quench and machining processes is imported. In the second step (1 - 2s), the platen is moved into contact with the wheel. In the third step (2 - 3s), the load is applied to the wheel generating high compressive stresses as shown in the curves for S-XX, S-YY and S-ZZ. When the platen is removed from contact with the wheel (3 - 4s), the compressive stresses decrease and eventually evolve into tensile residual stress. When compared with the results of the rim indentation model without initial residual stress (see Figure 6-4); the stresses presented in Figure 6-19 are very similar.

There was no significant change in the deformation values by including the residual stress data. As discussed earlier, in the literature review, fatigue failure is most probable in the tensile zone of the wheel with highest principal stress and strain.

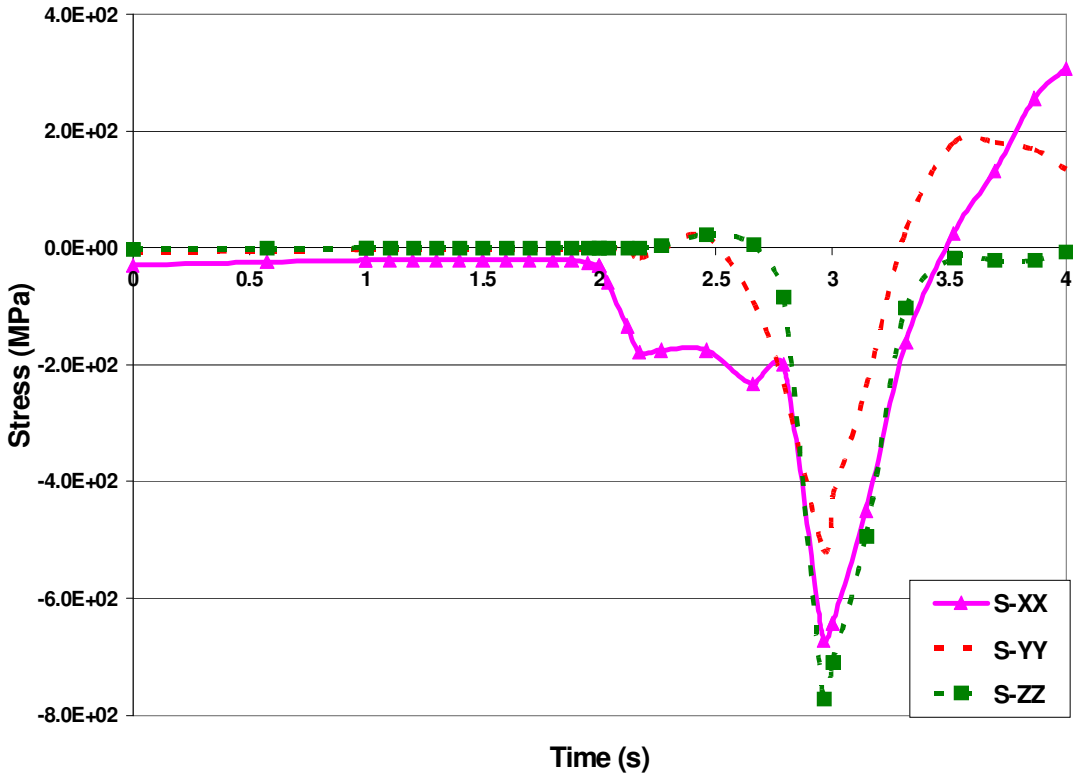

Figure 6-19. Stress state of a node in contact region

6.3.5. Radial fatigue model following rim indentation

As the final step in this analysis, the radial fatigue test was simulated including the effects of rim indentation and the initial residual stress distribution. Figure 6-20 shows the stress variation for one complete rotation of the radial fatigue test at the same node discussed in Figure 6-18. This particular node sustained the maximum equivalent plastic strain during the rim indentation test. In Figure 6-20, the Y-axis represents stress in MPa and the X-axis represents time in seconds. For the simulation process it was arbitrarily chosen that one complete rotation of the wheel takes 0.5 second, as discussed earlier that step time is arbitrary in this simulation. Figure 6-19 shows the first four steps of 1 sec time duration each. In the fourth step, the force on the platen was removed and the indented zone on the wheel developed a tensile residual stress state as shown in Figure 6-19. In the fifth step (4 - 5s), the contact condition between the platen and the wheel was removed so that in the sixth step (5 - 6s), the platen can be displaced away from the wheel. Although, these two steps do not change the stress distribution of the wheel and have not been shown on the graph, these steps are important in the model so that when radial fatigue test conditions are applied to the wheel, the platen does not interfere with the deformation in the wheel. In the seventh step (6 - 7 s), the pressure load consistent with the tire inflation is applied and in the eighth step (7 - 8s), radial fatigue test conditions are applied on the wheel. The radial fatigue test step (eighth step), has been setup to simulate two complete rotations of the wheel as discussed in Section 6.2, Figure 6-20 shows the stress variations at the node for one of the rotations (7.5 - 8s). During the radial fatigue test, only one stress component, i.e. S-XX exhibits significant variation with time. All other stress components such as S-YY, S-ZZ are nearly constant i.e. amplitude stress is very small.

Appendix B contains the input file for the full analysis.

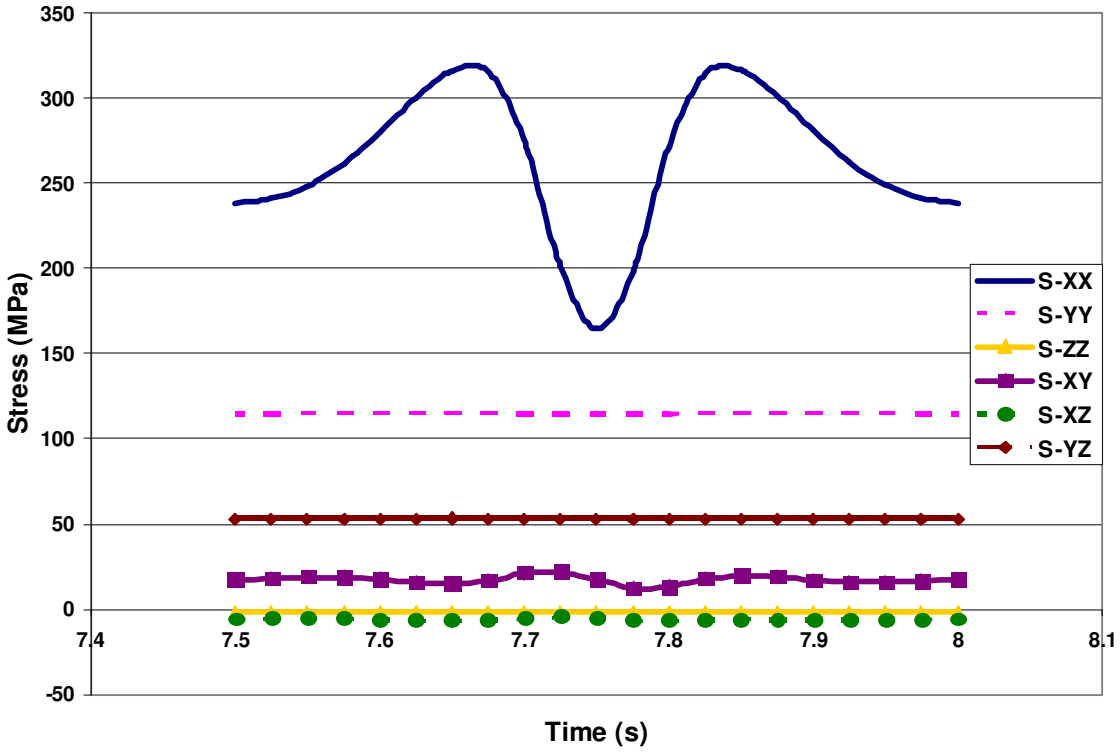

Figure 6-20. Stress state of a node during radial fatigue test

To put this result in context, the variation of stresses at the indented location of the wheel with respect to the position of the radial load may be plotted. Figure 6-21 shows the variation of principal stresses at the same node discussed in Figure 6-18, 16 and 17 with the angular variation if the radial load. At $\theta = 0$, the radial load is applied at the bead area diametrically opposite the indent location. At $\theta = 180$, the radial load is applied at the bead area closest to the node location. The principal stress estimations are shown in Figure 6-21. The maximum principal stress (solid blue curve) coincides with the stress oriented in the hoop direction or S-XX at this location (dashed pink curve). The intermediate and minimum principal stresses do not change significantly with time. Fatigue crack growth will be most pronounced in the plane perpendicular to the maximum principal stress. Thus, it

can be inferred that the stress state in the wheel at this location will lead to fatigue failure consistent with uni-axial loading conditions.

The laboratory fatigue experiments discussed in Section 4.2.2 and the empirical fatigue life equation (4-8) developed in the same section can be used to predict the fatigue life of the wheel. It should be noted that laboratory fatigue experiments were performed at load ratio (R) of -1. Based on Figure 6-21, R is estimated to be 0.53 in the radial fatigue tests which is very different from the fatigue experiments. Gao et. al. [2] have conducted experiments at R=0.1 and found the empirical relation (2-5) to predict fatigue life is valid. However, the effect of higher load ratios on the fatigue life has not been investigated. In this research project, it has been assumed that the equation (4-8) can be used for higher load ratios.

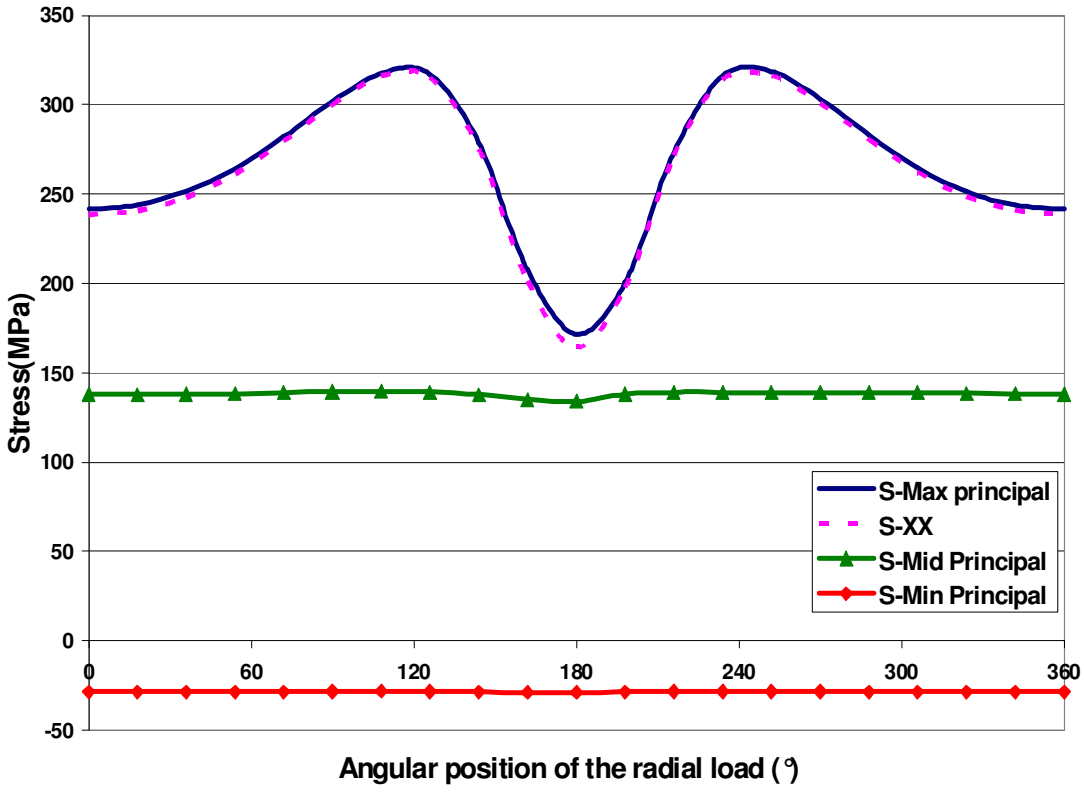

Figure 6-21. Principal stress of the node with maximum strain

The strain variation at a node on the inboard rim flange during the one rotation of the wheel during a radial fatigue test is shown in Figure 6-22. The two components of maximum principal total strain (E-Max Principal), the maximum principal plastic strain (PE- Max Principal) are shown in Figure 6-22. The total strain at the node is dominated by the plastic strain component. As seen from the figure, there is no significant change in the total strain during the radial fatigue test, it can be attributed to the fact that during the radial fatigue test, the amount f load applied on the wheel is not high enough to change the plastic strain state of the wheel.

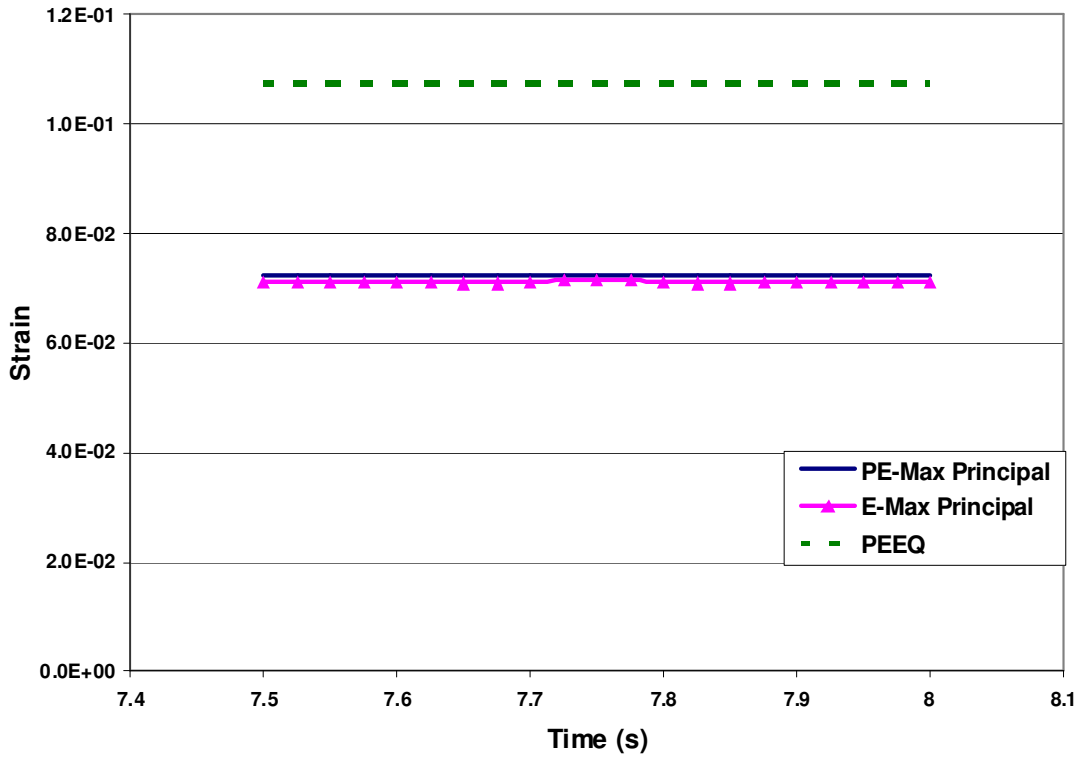

Figure 6-22. Strain state of the node during radial fatigue test

6.3.6. Numerical fatigue life

Equation (4-8) can be used to predict the numerical fatigue life for the rim indented wheels. Parameters C_2 and w were determined based on the predicted plastic strain. Since fatigue cracks are most likely to grow in the plane normal to maximum principal stress, the maximum principal plastic strain was used to determine the parameters C_2 and w.

For the node discussed in Section 6.3.5, the parameters C_2 and w were calculated with equations (4-10) and (4-11) based on the maximum principal plastic strain shown in Figure 6-22 were 1.8145 and -3.937. The total maximum strain (ε_{max}) extracted from Figure 6-22 is 7.16 x 10^{-2}. The stress amplitude (σ_a), 74.23 MPa was calculated based on the variation of maximum principal stress shown in Figure 6-21. The numerical fatigue life estimated for the rim indented wheel during the radial fatigue test using equation (4-8) is 1.32×10^6 cycles. Based on this fatigue life estimation, this particular wheel will pass the quality assurance check.

6.3.7. Verification

To verify the fatigue life estimation for radial fatigue test on rim deformed wheels, experiments need to be performed on the wheels. First the wheel should be deformed with the indentation load of 20.5 kN as discussed in Section 4.1.1 and then radial fatigue tests should be performed on the wheel as explained in Section 4.1.2.

It is critical to the verification of the fatigue life model that the number of cycles required to fail by the wheel are determined as accurately as possible through experiments. When the wheel is rotating on the radial fatigue test machine, the experiment needs to be paused and wheel must be tested at regular intervals for any cracks using dye-penetration test. This is a cumbersome job because everytime the wheel is checked for cracks, it needs to be taken off from the radial fatigue setup, the tire should be deflated and then removed from the wheel and after which the wheel can be checked for any cracks. If a crack is detected, the number of cycles to failure is reported in terms of the two cycles between consecutive stops. Otherwise, if no crack is detected, the wheel is again loaded on the radial fatigue test

setup with test re-started. This is a labor intensive job requiring a lot of time and the availability of fatigue setup.

Currently, the experiments are in progress with the two wheels which have already been discussed in section 4.1.1.

Till now, the wheels have been tested for 1.25×10^6 cycles. None, of the wheels have failed yet which agrees with the predictions made by the fatigue model discussed in section 6.3.6.

Further testing of the wheels has been delayed by production constraints at the wheel manufacturing company but there are definite plans in future at the wheel manufacturing company to complete the testing work for the wheels.

6.3.8. Sensitivity

This research project contributed in three main areas: 1) Rim Indentation test 2) Radial fatigue test and 3) Empirical fatigue life equation for different levels of pre-strain. Each of these factors can have an effect on the final fatigue life estimation for the wheels. In order to quantify the effects of these parameters, a sensitivity analysis was performed on the fatigue life estimation for wheels.

6.3.8.1. Variation in rim indentation load

In order to quantify the sensitivity of total fatigue life (N_f) with respect to rim indentation load, the load in the rim indentation model was increased by 10% to 22.55 kN and then decreased by 25% to 15.375 kN with respect to the baseline load of 20.5 kN. The rim indentation model was followed by radial fatigue test model with a radial load of 23 kN. In one of the cases, the radial fatigue model with 23 kN radial load was also simulated for an undeformed wheel (i.e. rim indentation load = 0 kN).

Figure 6-23 shows the principal stress variation of a node in the contact region of the wheel. For the curves with non-zero rim indentation load i.e. solid blue line with circular markers, dashed orange line with square markers and dashed dark green line with triangular markers, rim indentation loads were 22.55, 20.5 and 15.375 kN respectively. This particular node on all the three curves sustained the maximum strain. Whereas for the solid red line with zero rim indentation load and hence no plastic strain, this particular node is present at the same location as the node discussed for non-zero rim indentation loads. Also, the red curve represents maximum amplitude stress at that particular location (Maximum principal stress - Minimum principal stress). As shown in the Figure 6-23, the stress amplitude is the same for all the four cases because there is no change in the radial fatigue load of 23 kN but as the maximum stress is varying in the four conditions, the maximum principal total strain and maximum principal plastic strain are different for the four conditions.

For the 15.375 kN rim indentation load, maximum principal plastic strain was estimated to be 5.71×10^{-2}. Parameters C_2 and w estimated based on the maximum principal plastic strain using equations (4-10) and (4-11) were 1.427 and -3.75, respectively. The amplitude

stress extracted from the Figure 6-23 was 72.67 MPa and maximum principal total strain (ε_{max}) was estimated to be 5.55×10^{-2}. Based on these values, using equation (4-8), the total fatigue life (N_f) for the wheel was estimated to be 1.45×10^6 cycles. The fatigue life increased by 9.8% with a decrease of 25% in the rim indentation load. Similar procedure was carried out for 22.55 kN rim indentation load and the total fatigue life (N_f) estimated to be 1.25×10^6 cycles, a decrease of 5.3%. Figure 6-24 shows the variation of total fatigue life with change in rim indentation load for radial fatigue test load of 23 kN, as the load increases, the total fatigue life (N_f) decreases.

The fatigue life prediction for zero rim indentation load (i.e. undeformed wheel) failing at the inboard flange location using parameters from equation (4-9) was estimated to be 22×10^6 cycles, which is very high as compared to the fatigue lives shown in Figure 6-24 and hence is not shown in the figure.

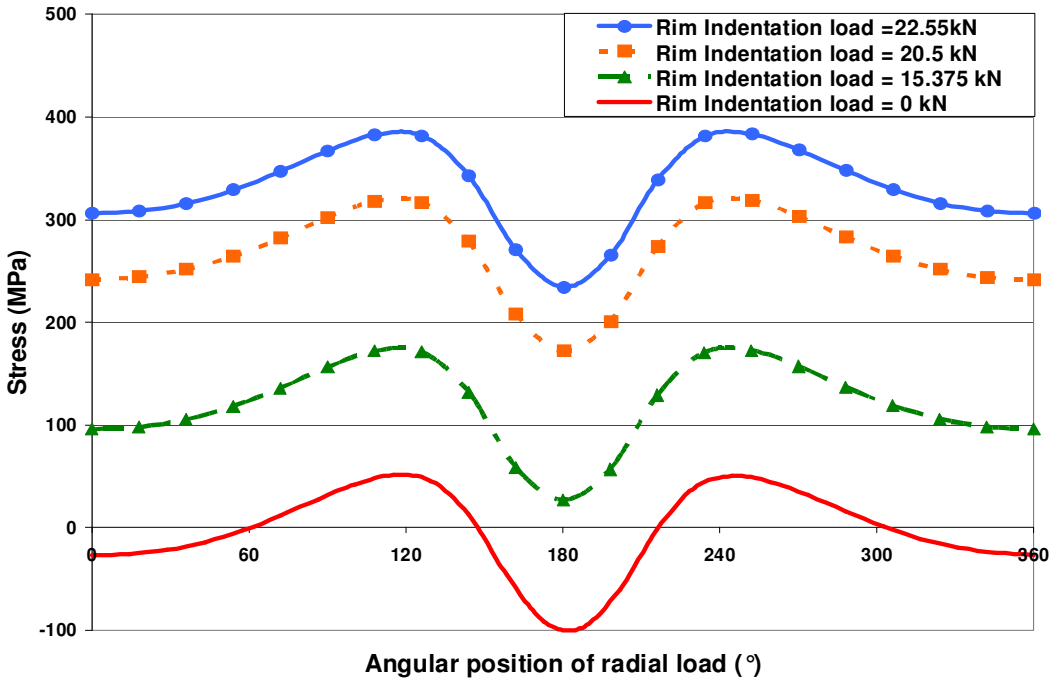

Figure 6-23. Principal stress variation with angular position of radial load

This fatigue life estimation is only applicable, if the fatigue failure occurs at the inboard flange. For an undeformed wheel, it is highly unlikely that the wheel will fail at the inboard flange, generally, the undeformed wheels have been observed to fail at the spoke region.

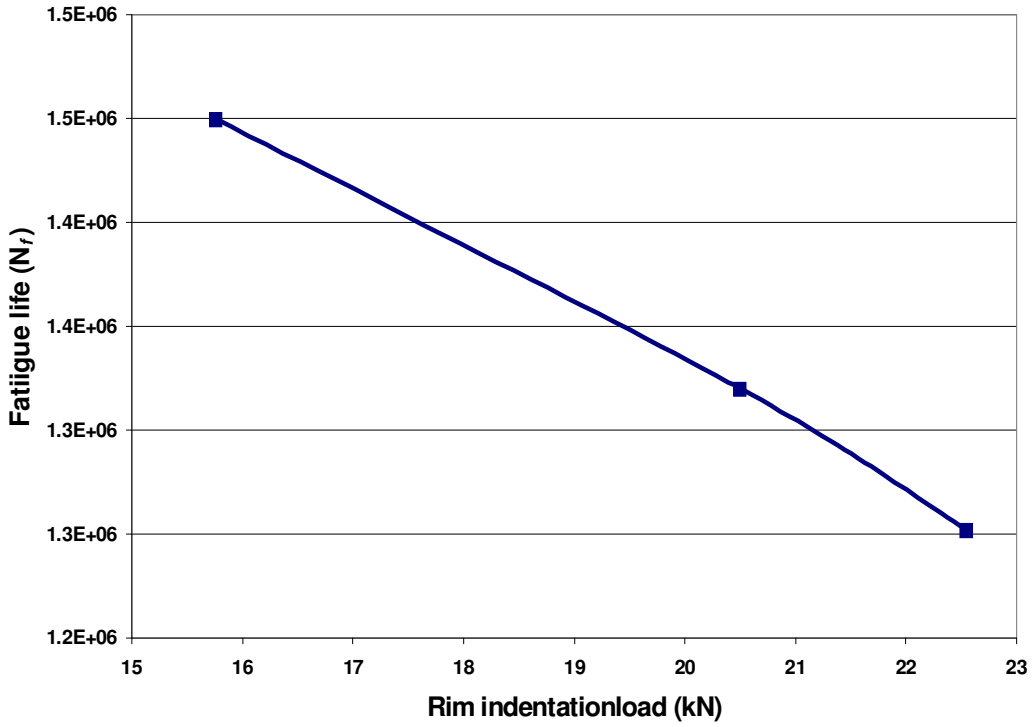

Figure 6-24. Variation of total fatigue life with rim indentation load

6.3.8.2. Variation in radial fatigue load

To quantify the effect of radial fatigue load on the total fatigue life (N_f), the rim indentation load was maintained at 20.5 kN and the radial fatigue test load was changed to 15.2 kN from 23 kN. As the rim indentation load was unaltered, the residual stress state of the node that sustained the maximum plastic strain is unchanged.

Figure 6-25 shows the principal stress variation of the same node that sustained the maximum plastic strain for the two radial fatigue test loading conditions. As expected, both curves have the same trend. It should also be noted that both curves have the same numerical value for the maxima of principal stress but the minima for the curves is dependent on the radial load applied. As both the curves have the same maximum principal stress, the total principal strain (ε_{max}) is equal for both the conditions (7.16×10^{-2}). The maximum principal plastic strain for the curve with radial load 15.2 kN was estimated at 7.25×10^{-2} whereas the same quantity for 23 kN radial load was determined to be 7.27×10^{-2}. These values are almost equal and show that the plastic strain sustained by the wheel is unaffected by the radial fatigue load upto 23kN. Parameters C_2 and w calculated for radial load 15.2 kN are 1.8195 and -3.94 using equations (4-10) and (4-11). The amplitude stress determined from Figure 6-25 for a radial load 15.2 kN is 51.67 MPa which is significantly different than 74.23 MPa amplitude stress determined for 23 kN radial load. The fatigue life calculated for wheels indented with a 20.5 kN deformation load and then subjected to 15.2 kN radial fatigue tests was 5.58×10^6 cycles.

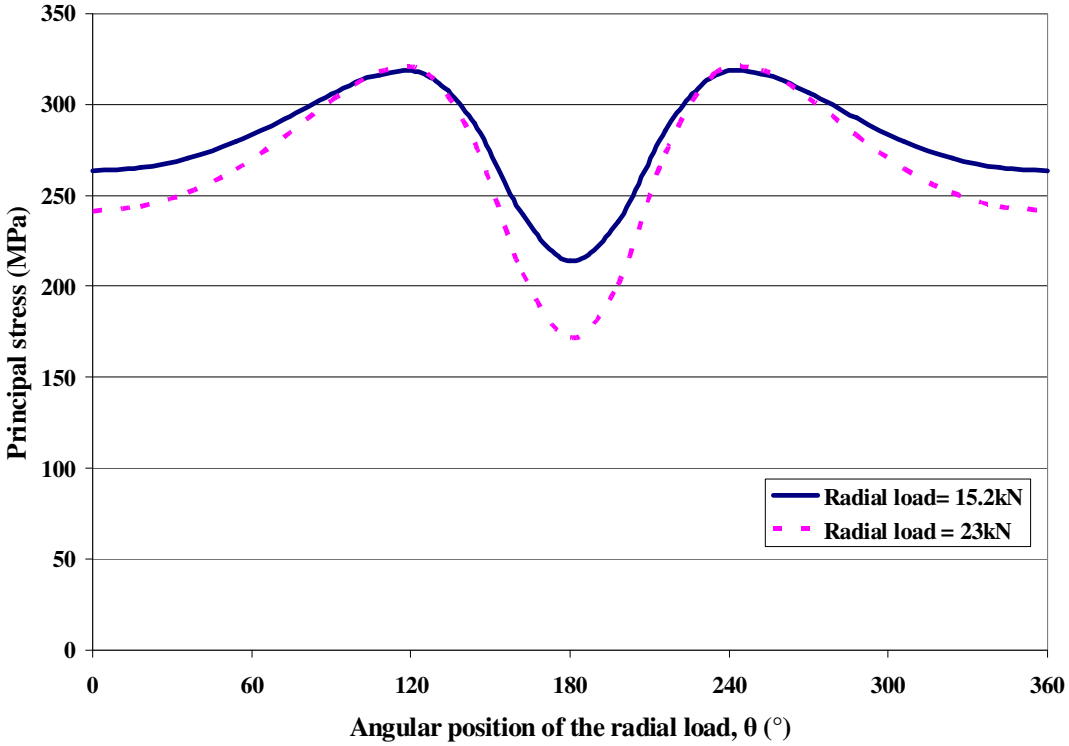

Figure 6-25. Principal stress with different radial loads

Following the same procedure as discussed above, fatigue life was calculated for a 17.5 and 20 kN radial load. Figure 6-26 shows the variation of total fatigue life with the radial fatigue test loading. The graph follows a non-linear path where the non-linearity is introduced by the different amplitude stress values due to variation in radial load.

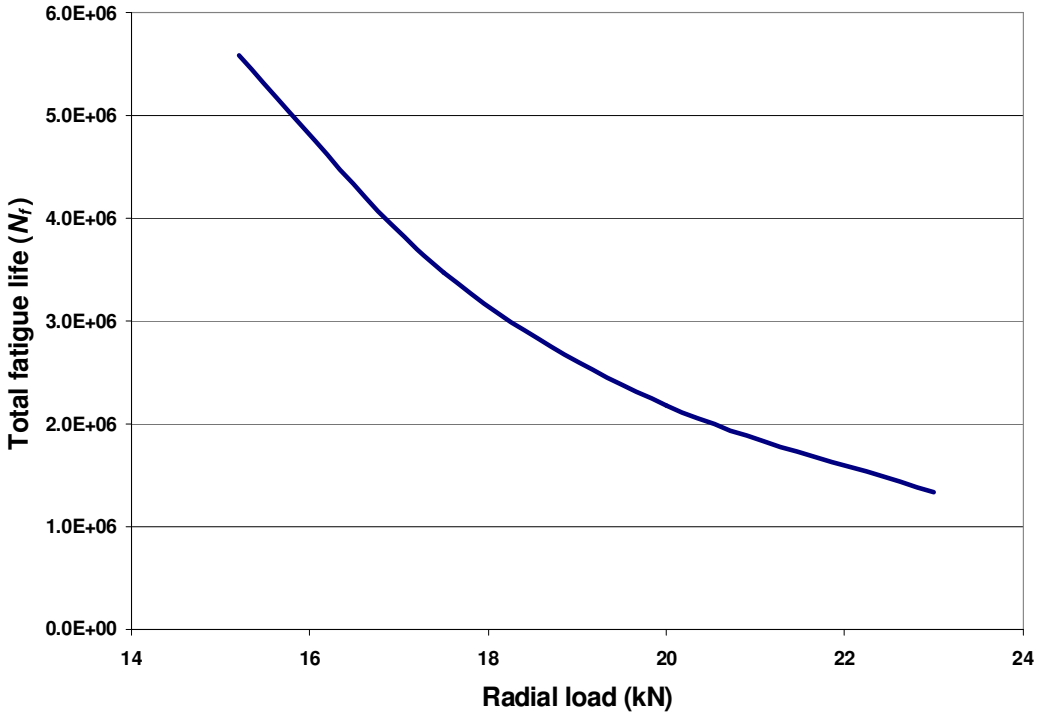

Figure 6-26. Effect of radial load on total fatigue life

6.3.8.3. Variation in the empirical parameters

The empirical relationship (see equation (4-8)) was used for estimating the fatigue life of rim indented wheels under radial fatigue test as discussed in Section 6.3.6. To estimate the effect of change in the empirical relation (4-8) on the total fatigue life (N_f), parameters C_2 and w were varied keeping the amplitude stress (σ_a), yield strength (σ_y) and maximum total strain (ε_{max}) constant. The numerical values used for σ_a, σ_y and ε_{max} were obtained for a rim indentation test load of 20.5 kN and radial fatigue test load condition of 23kN, as explained in Section 6.3.6.

i) Parameter C_2: The numerical value of parameter C_2 used in determining the fatigue life in the previous section was 1.8145. Keeping parameter w constant at -3.937, the value of parameter C_2 was increased by 10% to 1.9959 and then decreased by 10% to 1.633. Table 6-5. shows the percentage change in total fatigue life with change in parameter C_2 in comparison to baseline fatigue life of 1.33×10^6. From the table, it can be seen that with a 10% decrease in parameter C_2 fatigue life decreased by 10.02% and with the 10% increase in parameter C_2, there was a 9.95% increase in fatigue life. A linear relationship between total fatigue life (N_f) and parameter C_2 can be inferred from the analysis. The analysis can be extended to conclude that a small error in determining the value of parameter C_2 will introduce a linearly dependent small error in the numerical value of total fatigue life (N_f). Further, a safety of factor considered in reporting the allowed total fatigue should be able to eliminate the effect of parameter C_2.

Table 6-5. Change in total fatigue life with parameter C_2

Parameter C2	Nf	% change
10% decrease	1.19E+06	-10.02
1.8145	1.33E+06	0.00
10% increase	1.46E+06	9.95

ii) Parameter *w*: To estimate the effect of parameter *w* on the total fatigue life (N_f), parameter C_2 was kept constant at 1.8145 and parameter *w* was changed by +/-10%. When the numerical value of parameter *w* was decreased by 10% to -3.5433, the total fatigue life decreased by 74.15%. On the other hand, an increase in the value of parameter *w* by 10% to -4.33, increased the total fatigue life by 284.78%. Table 6-6 summarizes the results of the analysis. It can be clearly seen that the dependence of total fatigue life (N_f) on parameter *w* is far from linear. To ascertain the effect of the parameter *w* on total fatigue life (N_f), Figure 6-27 was developed which shows the percentage change in total fatigue life (N_f) with change in parameter *w*. The figure shows that the change in fatigue life is more pronounced when there is an increase in parameter *w*. For example, in Figure 6-27, four data points have been marked at +/- 2% and 6% change in parameter *w*. At 2% increase in parameter *w*, the total fatigue life increased by 31% whereas for the 2% decrease in parameter *w*, the total fatigue life decreased by 23%. A factor of safety can be defined which can accommodate error in determining the value of parameter *w* upto +/- 2% but if the error in determining the value of parameter is as high as +6%, the error in estimating total fatigue life is very high to a value of 124%. Hence, maximum care should be taken in deciding the parameter *w*.

Table 6-6. Change in total fatigue life with parameter *w*

Parameter *w*	**Nf**	**% change**
10% decrease	3.43E+05	-74.15
-3.937	1.33E+06	0.00
10% increase	5.11E+06	284.78

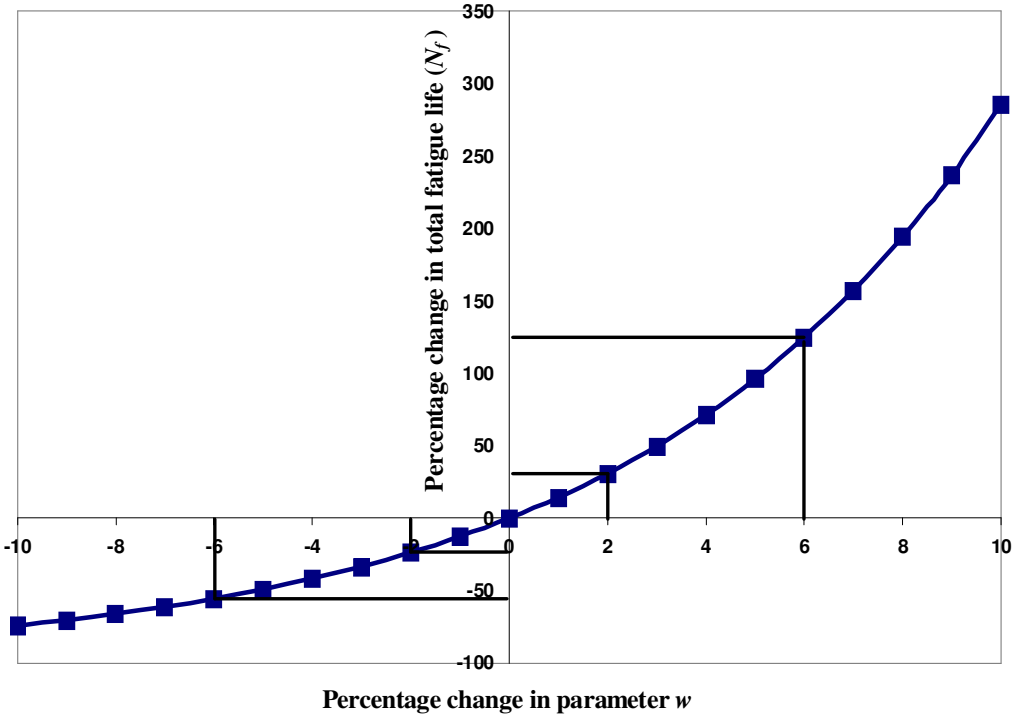

Figure 6-27. Percentage change in fatigue life with change in parameter *w*

6.3.8.4. Variation in material properties

Sections 6.1.2.1 and 6.1.2.2 describe the effect of changing material properties on the rim indentation model. It was established that with a 15% decrease in Young's modulus to 56.3 GPa and a 10% increase in the flow strength, the load versus displacement curve for the wheel matched well with the experiments.

It was also established in Section 6.2.1.1 that radial fatigue model is sensitive to the material properties such that with a reduced Young's modulus to 56.3 GPa, the radial load required in the radial fatigue test model to match the experiments was estimated to be 20.5 kN which is still larger than 15.2 kN radial load applied in the experiments but reduced from 23 kN, as required with a Young's modulus of 66.25 GPa.

For the node discussed in Section 6.3.5 and the material properties, E=56.3 GPa and 10% increased flow strength, the maximum principal plastic strain is estimated to be 6.342 x 10^{-2}. The parameters C_2 and w calculated with equations (4-10) and (4-11) are 1.526 and -3.824. The total maximum strain (ε_{max}) extracted from the radial fatigue model is 6.035x 10^{-2}. The stress amplitude (σ_a) is estimated to be 70 MPa based on the variation of maximum principal stress during the radial fatigue test. Finally, as the flow strength data was increased by 10%, the Yield strength used in equation 4-8 is 180.4 MPa. Based on the above parameters, the fatigue life estimated for the rim indented wheel during the radial fatigue test using equation (4-8) is 1.92×10^6 cycles.

In Section 6.3.6, the predicted the fatigue life was 1.32×10^6 cycles based upon the material properties determined through the tensile test (see Section 4.2.1) whereas with the changed material properties (the Young's modulus decreased by 15% and the flow strength increased by 10%), the fatigue life was estimated to be 1.92×10^6 cycles. The percentage increase in the fatigue life with modified material properties as compared to original properties is calculated to be 45.45%. Hence, it can be inferred that the fatigue life model is sensitive to the material properties of the aluminum alloy used for manufacturing.

7 Conclusions and Future Work

7.1. Conclusions

7.1.1. Rim indentation model

A model of an industrial rim indentation test used during quality assurance testing of wheels was developed to predict the permanent deformation of a wheel following a specified load cycle. This finite element model was developed using ABAQUS, a commercial software package. The modeling results were verified through comparison to data measured during industrial tests. It was established that rim indentation produces high tensile stress (~300 MPa) and plastic strains (~10%) in a localized region defined by contact with the platen. The indented location with high residual tensile stress was recognized as the potential site for fatigue failure. A previously developed modeling technique was used to predict the residual stress distribution following the quench and machining processes for use as an initial condition in the rim indentation model. Their inclusion of the residual stresses did not alter the results significantly at the indentation location but provided a more comprehensive estimation of the deformation and stress state of the wheel during indentation. It was established that due to the low stress levels present at the rim flange location (-30 MPa maximum as shown in Figure 6-16), residual stresses do not affect the results of the rim indentation. It was also established that second order 10-node tetrahedral elements were better suited for contact simulation of the rim indentation test as compared to linear 4-node tetrahedral elements. The rim indentation model was found to be sensitive to the material properties used for the wheel.

7.1.2. Radial fatigue test model

A model of the radial fatigue test for wheels was developed to estimate the characteristic cyclic stress and strain variation during this test. Although, the model does not predict the correct maximum and minimum strains at the applied test load, it was able to qualitatively predict the strain curves. The radial load was increased to 23 kN to obtain the same strain amplitudes through model as in experiments. With a radial load of 23 kN, the strain amplitude, and numerical values for maximum and minimum strain matched well with the experiments for the strain gauge located at the rim flange which is critical to this project. It was also established that the radial fatigue test model is sensitive to the material properties of the aluminum alloy used in the model. With a reduced Young's modulus to 56.3 GPa, the radial load required to match the model predictions with the experimental data was reduced to 20.5 kN.

7.1.3. Empirical fatigue life relation

Uni-axial laboratory fatigue experiments were performed on samples cut from wheels and pre-strained with 0, 5 and 10% plastic strain. It was observed that with the increase in the pre-strain level of the fatigue samples, their fatigue life decreased. The defect(s) responsible for the failure of the samples were identified using a Scanning Electron Microscope (SEM) and in all case were found to be micro-porosity in close proximity to the specimen surface. The fatigue data was used to modify an empirical relationship for total fatigue life of cast aluminum alloys to include levels of pre-strain in the samples.

7.1.4. Combination of models

The rim indentation model, radial fatigue model and empirical fatigue life equation were combined to estimate the fatigue life of a rim indented wheel during radial fatigue testing. It was observed that the rim indentation load played a major role in deciding the plastic strain state of the wheel which was crucial for determining the parameters in the empirical fatigue life equation. The amplitude stress and total maximum strain during a radial fatigue cycle were the parameters obtained from the radial fatigue model. It was noticed that the amount of radial load during the radial fatigue test had a direct influence on the amplitude stress for the fatigue life estimation whereas the total maximum strain was found to be independent of the amount of radial load. The numerical value of fatigue life predicted for 20.5 kN indentation load and 23 kN radial load was 1.32×10^6 cycles.

The sensitivity of the fatigue life was analyzed based on rim indentation load, radial fatigue load, the new empirical fatigue equation and material properties. With a reduced Young's modulus to 56.3 GPa and 10% increased flow strength, the radail fatigue life for the rim indented wheel was estimated to be 1.92×10^6 cycles.

7.2. Future work

7.2.1. New rim indentation test

During the course of this research project, the wheel manufacturing company has modified the Rim Indentation test. The new rim indentation test has two changes over the earlier test:

1) Instead of directly deforming the wheel using a platen as done in the earlier test, now, a tire mounted wheel is deformed using a wedge shaped platen. The load applied to the wedge shaped platen deforms the tire first and as the load is gradually increased, the wheel is deformed.

2) In the earlier test, only the inboard rim flange was deformed and the permanent deformation sustained at that section was measured whereas in the new rim indentation test, both the inboard and outboard rim flanges are deformed.

As discussed in the Section 1.2, the rim indentation test was developed to assess the effects of rim deformation on the radial fatigue life of wheels. The deformation was intended to be similar to that sustained by a wheel following events like hitting a curb or running into a pothole etc. In all practical cases of rim deformation, a tire is mounted on the wheel. Hence, the changes made to the earlier rim indentation test are done with a point of view of correlating the test more closely to the driving scenarios.

In light of the new developments, the current rim indentation model can be modified to include the tire geometry and material behavior of rubber in the model. As both the inboard and outboard rim flanges are deformed in the new test, more fatigue experiments should be done, in order to modify the empirical fatigue life relation to include the fatigue properties of the outboard flange of the wheel. The radial fatigue test model developed in this research project can be directly applied without change to predict the stress characteristics of the wheel for the radial fatigue test after the new rim indentation test.

7.2.2. Modified fatigue life equation

The fatigue life relation (refer equation (4-8)) considering pre-strain that was developed in this research project is specific to the casting parameters and defects seen in the inboard rim flange of the wheel.

As discussed in the Section 4.2.2.2, all the fatigue samples for developing the mathematical relation for fatigue life with pre-strain were taken from the inboard rim flange of the wheel. Within acceptable variations, the SDAS, pore density, size and distribution of the eutectic particles were same in all the fatigue samples tested. This was justified as the developed fatigue life equation was used to calculate the fatigue life of wheels which were deformed at the inboard rim flange.

In order to develop, a generalized equation of fatigue life with pre-strain, varying SDAS and pore sizes should be tested for fatigue behavior. The developed equation would show distinctly the effect of pre-strain on fatigue life. In the current research work, fatigue behavior of cast aluminum alloy was analyzed for only two levels of pre-strain (5 and 10%), more pre-strain levels should be examined for a better understanding of the effect of pre-strain on fatigue life. A more detailed analysis of the effects of pre-strain on the fatigue life of cast aluminum alloys is an underexplored interesting topic of research.

The current research work also exhibited the limited amount of work available on the fatigue life estimation for cast aluminum alloys with high load ratio. The fatigue life data available in the literature ranges for a load ratio of -1 to 0.1. In the current research project, due to rim indentation test, high tensile stresses are developed which give rise to high load ratio (~ 0.5) during the radial fatigue test. Hence, the fatigue life empirical relation developed in future should consider the effects of high load ratios on the fatigue life.

7.2.3. Multi-axial fatigue loading

In the radial fatigue test model of the wheel, the radial fatigue test conditions were close to a uni-axial fatigue loading conditions with the maximum principal stress varying with time while the intermediate and minimum principal stresses were constant during the radial fatigue test. Although, the intermediate and minimum principal stress values did not change with time and their effects on the fatigue life of the wheels were neglected for simplicity but in a general case, a constant load in a direction other than the uni-axial fatigue load direction will affect the fatigue life of the sample. Hence, in future, the fatigue life relation should be modified to include the effect of intermediate and minimum principal stresses on the fatigue life of specimen.

References

[1] Christina M. Estey, " Thermal mechanical analysis of wheel deformation induced from quenching," M.A.Sc. thesis, University of British Columbia, 2004

[2] Y. X. Gao, J. Z. Yi, P. D. Lee and T. C. Lindley, "The effect of porosity on the fatigue life of cast aluminum silicon alloys," Fatigue Fract Engng Mater Struct 27, 559–57

[3] J. Z. Yi, Y. X. Gao, P. D. Lee and T. C. Lindley, "Microstructure based Fatigue Life Prediction for Cast A356-T6 aluminum -Silicon Alloys," METALLURGICAL AND MATERIALS TRANSACTIONS B, VOLUME 37B, APRIL 2006-301

[4] Yeh-Liang Hsu, Chia-Chieh Yu, Shang-Chieh Wu, " Developing an automated design modification system for alumiunm disc wheels," Proceedings of the 10th International Conference on Computer Supported Cooperative Work in Design, IEEE 2006

[5] P. Ramamurty Raju, B. Satyanarayana , K. Ramji , K. Suresh Babu, " Evaluation of fatigue life of aluminum alloy wheels under radial loads ," Engineering Failure Analysis 14 (2007) 791–800

[6] M. Firat, U. Kocabicak, "Analytical durability modeling and evaluation - complementary techniques for physical testing of automotive components," Engineering Failure Analysis 11 (2004) 655-674

[7] V. Grubisic, G. Fischer, "Automotive wheels, methods and procedures for optimal design and testing," SAE Technical Paper Series. 830135; 1984:1.508–1.525

[8] J. Z. Yi, Y. X. Gao, P. D. Lee and T. C. Lindley, "Scatter in fatigue life due to effects of Porosity in Cast A356-T6 aluminum silicon Alloys," METALLURGICAL AND MATERIALS TRANSACTIONS A, VOLUME 34A, SEPTEMBER 2003-1879

[9] Q.G. Wang, D. Apelian, D.A. Lados, "Fatigue behavior of A356-T6 aluminum cast alloys. Part I. Effect of casting defects," Journal of Light Metals 1 - Copyright The Minerals, Metals & Materials Society (TMS), (2001) 73-84

[10] Q.G. Wang, C. J. Davidson, J. R. Friffiths and P. N. Crepeau, “Oxide Films, Pores and the Fatigue Lives of Aluminium Alloys,” METALLURGICAL AND MATERIALS TRANSACTIONS B, VOLUME 37B, APRIL 2006-887

[11] Q.G. Wang , D. Apelian, D.A. Lados, “Fatigue behavior of A356/ 357 cast aluminum cast alloys. Part II. Effect of microstructural constituents,” Journal of Light Metals 1- Copyright The Minerals, Metals & Materials Society (TMS), (2001) 85-97

[12] J. Campbell, “ Castings,”First edition, Butterworth_Heinemann, Oxford, U.K. 1991

[13] Ken Gall, Mark F. Horstemeyer, Brett W. Degner, David L. McDowell and Jinghong Fan ,"On the driving force for fatigue crack formation from inclusions and voids in a cast A356 aluminum alloy," International Journal of Fracture 108: 207-233, 2001

[14] J. Z. Yi, Y. X. Gao, P. D. Lee and T. C. Lindley, “ Effect of Fe-content on fatigue crack initiation and propagation in a cast aluminum–silicon alloy (A356–T6),” Materials Science and Engineering A 386 (2004) 396–407

[15] M. J. Couper, A. E. Neeson and J. R. Griffiths, “Casting Defects and the Fatigue behaviour of an aluminium casting alloy,” Fatigue Fracture Engineering Material Structures Vol. 13 No. 3 pp. 213-227, 1990

[16] D.L. McDowell, K. Gall, M.F. Horstemeyer, J. Fan, "Microstructure-based fatigue modeling of cast A356-T6 alloy," Engineering Fracture Mechanics 70 (2003) 49-80

[17] J Campbell,” An overview of the feects of bifilms on the structure and properties of cast alloys,” METALLURGICAL AND MATERIALS TRANSACTIONS B, VOLUME 37B, DECEMBER 2006-857

[18] C. Nyahumwa, N.R. Green and J. Campbell, “ Influence of Casting Technique and Hot Isostatic Pressing on the Fatigue of an Al-7Si-Mg Alloy,” METALLURGICAL AND MATERIALS TRANSACTIONS A, VOLUME 32A, FEBRUARY 2001—349

[19] M. J. caton, J. W. Jones, J. M. Boileau and J. E. Allison, “ The Effect of Solidification on rate on the growth of fatigue cracks in cast 319 type aluminium alloy,” METALLURGICAL AND MATERIALS TRANSACTIONS A, VOLUME 30A, SEPTEMBER 1999-3055

[20] M. J. caton, J. W. Jones, J. M. Boileau and J. E. Allison, “Use of small fatigue crack growth analysis in predicting the S-N response of cast aluminium alloys,” ASTM International 2000

[21] Y. X. Gao, J. Z. Yi, P. D. Lee and T. C. Lindley, “A micro-cell model of the effect of microstructure and defects on fatigue resistance in cast aluminium alloys,” 2004 Acta Materialia Inc. Published by Elsevier Ltd

[22] B. Skallerud, T. Iveland and G. Harkegard, “Fatigue Life Assessment of Aluminum Alloys with Casting Defects,” Engng Fract Mech, Vol 44, pp 857-874, 1993

[23] H. Nisitani, M. Goto and N. Kawagoishi, “ A small-crack growth law and its related phenomena,” Eng Fract Mech 41 (4) (1992), pp. 499–513

[24] A. F. Getman and Yu. K. Shtovba, “ Influence of preliminary plastic deformation on the fatigue properties of aluminium alloys,” Energy Scientific Production Association, Moscow, translated from Problemy Prochnosti, No. 2, pp70-73, 1982

[25] Kassim S. Al-Rubaie, Emerson K.L. Barroso, Leonardo B. Godefroid, “ Fatigue crack growth analysis of pre strained 7475- T7351 aluminum alloy,” International Journal of Fatigue, V.28, p. 129-139, 2006

[26] Kassim S. Al-Rubaie , Marcio A. Del Grande, Dilermando N. Travessa and Katia R. Cardoso, “ Effect of the pre strain on fatigue life of 7050-T7451,” Material Science and Engineering, V.464, p. 141-150, 2007

[27] P. Ramamurty Raju, B. Satyanarayana, K. Ramji, K. Suresh Babu, “ Evaluation of fatigue life of aluminum alloy wheels under radial loads,” Engineering Failure Analysis 14 (2007) 791–800

[28] Yeh-Liang Hsu, Shu-Gen Wang and Tzu-Chi Liu, “ Prediction of Fatigue Failures of Aluminum Disc Wheels Using the Failure Probability Contour Based on Historical Test Data,” Journal of the Chinese Institute of Industrial Engineers, Vol. 21, No. 6, pp. 551-558 (2004)

[29] J. Stearns, T. S. Srivatsan, X. Gao, and P. C. Lam, “Understanding the Influence of Pressure and Radial Loads on Stress and Displacement Response of a Rotating Body: The AutomobileWheel,” International Journal of Rotating Machinery, Volume 2006, Article ID 60193, Pages 1–8

[30] U. Kocabicak and M. Firat, “Numerical analysis of wheel cornering fatigue tests,” Engineering Failure Analysis 8 (2001) 339-354

[31] M H R Ghoreishy, “ Steady state rolling analysis of a radial tyre: comparison with experimental results,”Proceedings of IMechE Vol. 220 Part D: Journal of Automobile Engineering, 2006

[32] Peifeng Li, “ Through Process Modeling of Aluminum alloy Castings to predict fatigue performance.” PhD thesis, Imperial College, London, 2006

Appendices

Appendix A

Section 4.1.2.3 provided strain measurements observed for gauges 1, 4, 7, 10, 13 and 16 during a radial fatigue test. These strain gauges were chosen for discussion because of their orientations where of primary interest for the model development. The rest of strain measurements are discussed in this appendix.

As discussed in Section 4.2.1.2, strain measurements were taken for 18 gauges at four different conditions:

1) Base level (Zero error): Strain gauge measurements for all the 18 gauges at conditions 2, 3 and 4 were zero error corrected by subtracting the base level strain from them

2) Tire mounted on the wheel but not inflated

3) Tire inflated to test conditions i.e. 60 psi

4) Wheel rotated under radial fatigue test conditions

Figure 1 shows the zero corrected strain measurements for all the 18 gauges before and after the inflation pressure of 60 psi. The diamond shaped dark blue markers in the figure represent the strain measurements for all the gauges after the tire has been mounted on the wheel but not inflated. The numerical strain values are very low as no load has been applied on the wheel yet. The square shaped dark red markers in the figure show the effect of inflation pressure of 60 psi on the strain levels of the wheel. It can be seen from Figure 1 that gauges 1 to 6, which are located on the inner spoke region undergo compressive strain whereas the strain gauges on the outer spoke region i.e. 16 to 18 sustain tensile strain. Gauges 11 to 13 did not have an appreciable change in strain level because of the air pressure. Gauges 7 and 8 sustained tensile strain whereas gauges 9, 10, 14 and 15 sustained compressive strain due to the inflation pressure.

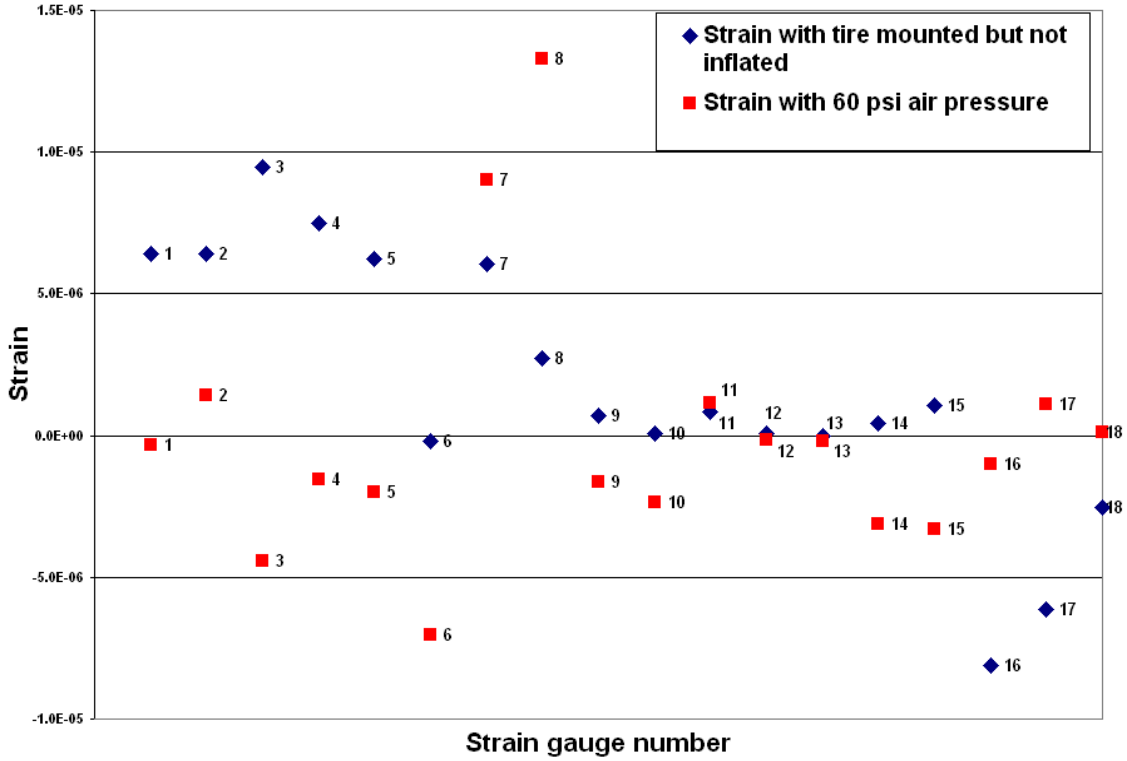

Figure A-1.Strain measurements for 18 gauges before and after air pressure

In Chapter 4 Figures 4-7 to 4-10 showed the strain sustained by gauges 1, 4, 7, 10, 13 and 16 under radial fatigue test conditions i.e. radial load of 1560 kgf and a rotational speed of 3 km/ hr. This appendix presents the strain curves for the gauges not discussed in chapter 4.

Figure 2 shows the strain curves for gauges 2 and 5. Their similar location on two different gauges (see Figure 4-4) results in similar trend as shown in the figure. The numerical values of strain for gauge 5 are lower than gauge 2, which may be due to the angular orientation of the gauges not being exactly same. Figure 3 shows the strain curves for gauges 3 and 6, as expected, they also have similar trend in their curves but it is interesting to note that the strain values for gauge 6 are higher than gauge 3. A simple explanation for this behavior can be summarized as the vector addition of strains in gauge 2 and gauge 3 should be equal to similar addition for gauges 5 and 6. This should also be true as the numerical strain values for gauges 1 and 4 were equal as shown in Figure 4-7.

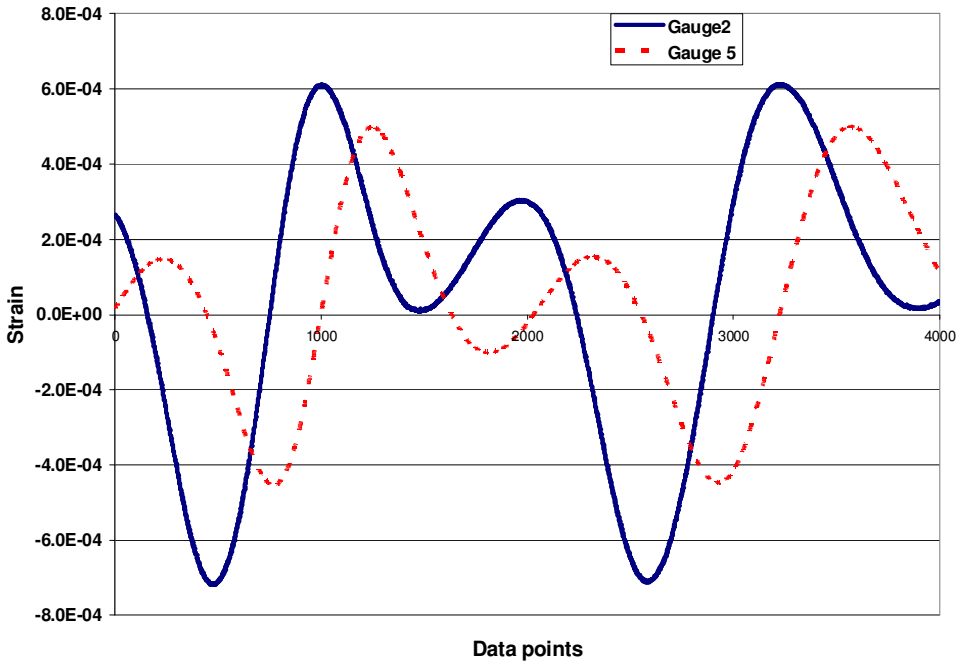

Figure A-2. Strain curves for gauges 2 and 5

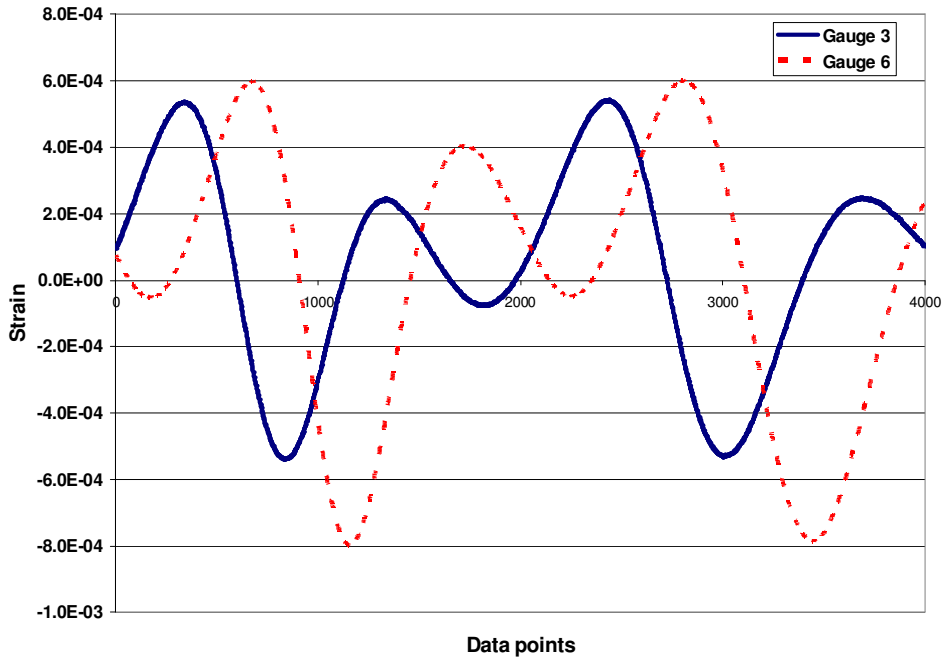

Figure A-3. Strain curves for gauges 3 and 6

Gauges 9 and 12 are located on the rim area of the wheel as shown in Figure 4-4. Figure 4 shows the strain levels and trends for these gauges. As explained for gauges 7 and 10 in Section 4.1.2.3 and Figure 4-8, the difference in the numerical values of the strain for the gauges can be attributed to high stiffness near the spoke region for gauge 9 and comparatively lower stiffness for gauge 12 at the window location between two spokes.

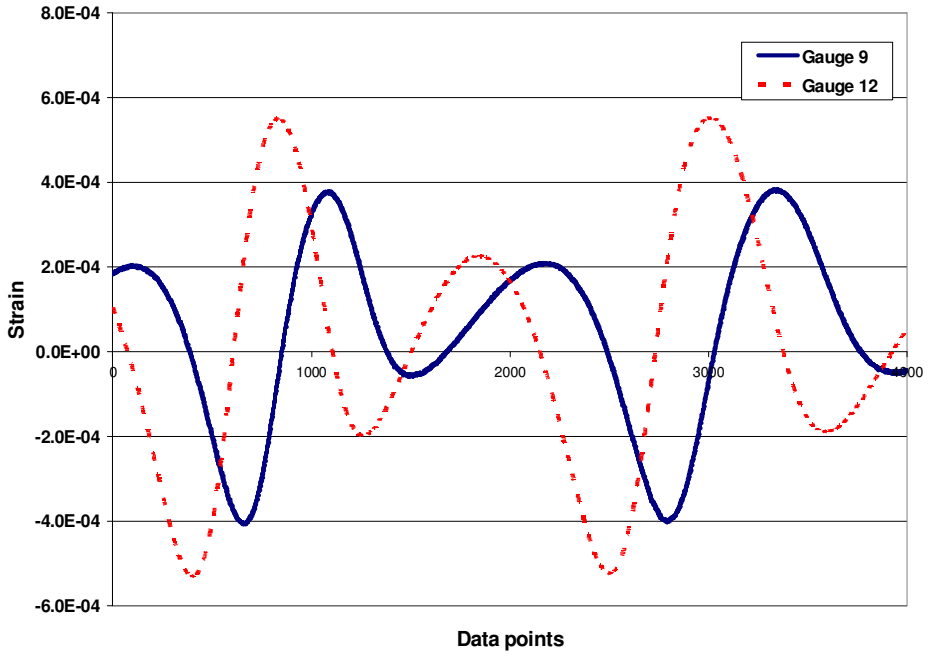

Figure A-4. Strain curves for gauges 9 and 12

.

Figure 5 shows the strain curves for gauges 10 and 12. A similar reasoning can be applied to explain their behavior and numerical values as applied to gauges 9 and 12.

Figure 6 shows the strain data for gauges 14 and 15. These strain gauges are located on inboard rim flange as shown in the Figure 4-5. They show higher tensile strain and were recognized as probable fatigue failure locations

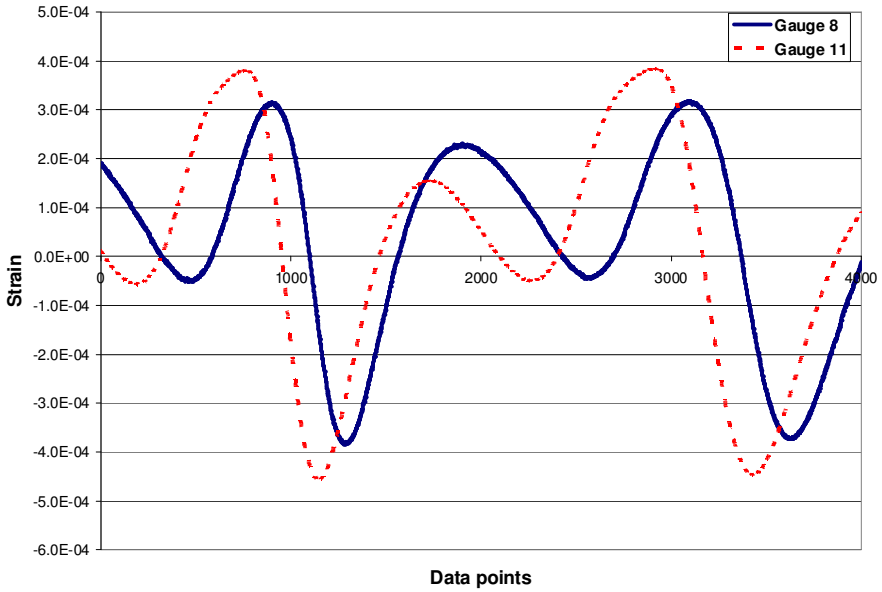

Figure A-5. Strain curves for gauges 8 and 11

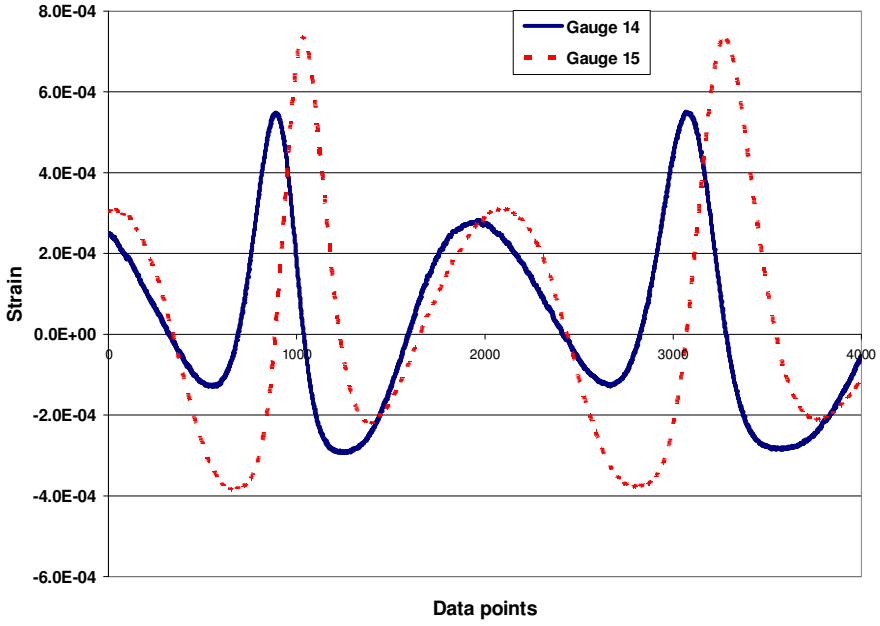

Figure A-6. Strain curves for gauges 14 and 15

Figure 7 shows the strain curves for gauges 17 and 18. These gauges show high compressive strains which is consistent with strain gauge 16, see Figure 4- 10.

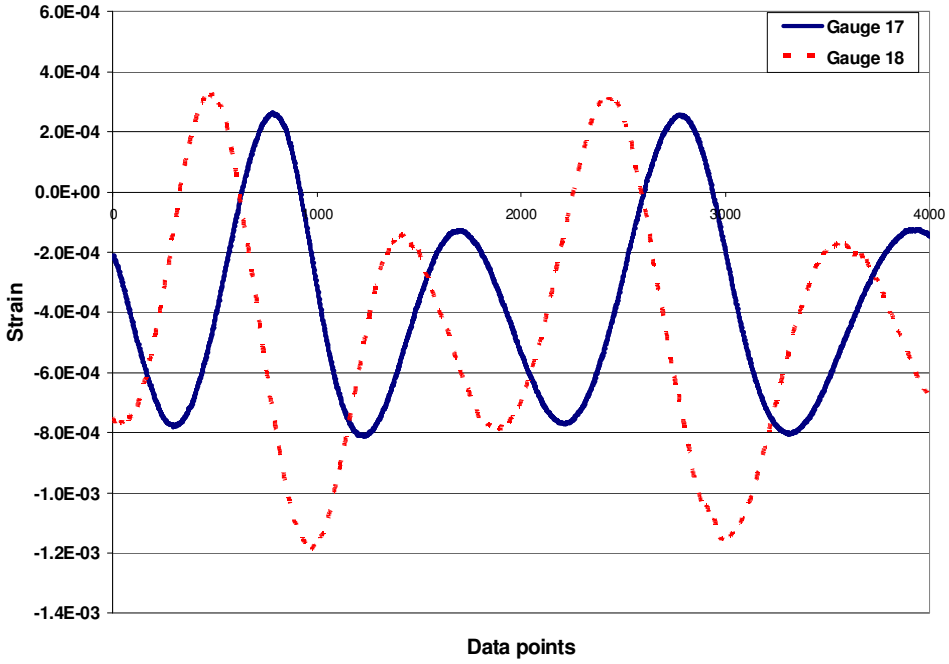

Figure A-7. Strain curves for gauges 17 and 18

Appendix B

Input file for the analysis

****

********INITIAL PARAMETERS **********

****

*Heading

** Job name: Rim_indentation_radial_fatigue

**Model name: Rim_indentation_radial_fatigue_model

*Preprint, echo=NO, model=NO, history=NO, contact=NO

****

*******DEFINITION OF FIRST PART, FULL WHEEL**********

****

** PARTS

**

*Part, name=FULL_WHEEL_MESHED

*Node

**

**Definition of the nodes on the wheel

**

*Element, type=C3D10

**

**Definition of elements on the wheel and their connectivity to the nodes

**

*NSET

**

```
** Node sets defined for boundary conditions
**
*ELSET
**
** Element sets for surface definition where pressure and bead loads are applied
** Set of elements which define the slave surface on the wheel
**
*Surface, type=ELEMENT, name=Wheel_slave_surf
**Defines the slave surface on the wheel
**
*Surface, type=ELEMENT, name= FULL_WHEEL_MESHED-1.Pressure_area
**Defines the surface on the wheel where pressure is applied
**
*Surface, type=ELEMENT, name= FULL_WHEEL_MESHED-1.Bead_area
**Defines the bead surface on the wheel where radial load is applied
**
** Section: Section-1-_WHEEL-1_PICKEDSET9
*Solid Section, elset=_WHEEL-1_PICKEDSET9, material="A356 ALLOY"
1.,
**Selects the full volume of the wheel to assign the material properties
**
*End Part
**End of part FULL_WHEEL_MESHED
**********************************************************************
*******DEFINITION OF SECOND PART, PLATEN **************************
```

```
**********************************************************************
*Part, name=Platen
*Node
**
**Definition of the nodes on the platen
**
*Element, type=R3D3
**
**Definition of elements on the platen and their connectivity to the nodes
**
*NSET
**
** Reference node selected for applying boundary conditions and concentrated load
**
**
*ELSET
**
** Set of elements which define the master surface on the platen
**
*Surface, type=ELEMENT, name=Platen_mater_surface
**
**Master surface on the platen
**
*End Part
**
```

```
**********************************************************************
*******DEFINITION OF ASSEMBLY OF TWO PARTS************************
**********************************************************************
** ASSEMBLY
**
*Assembly, name=Assembly
**
*Instance, name=FULL_WHEEL_MESHED-1, part=FULL_WHEEL_MESHED
*End Instance
**
*Instance, name=Platen-1, part=Platen
*End Instance
**
** Definition of a new cylindrical coordinate system
 *Orientation, name=FULL_WHEEL_MESHED-1-Cyl_sys, system=CYLINDRICAL
        0.,          0.,          0.,          0.,          -1.,          0.
1, 0.
** Constraint: Constraint-1
*End Assembly
**
**********************************************************************
*******MATERIAL AND INTERACTION PROPERTIES************************
**********************************************************************
** MATERIALS
**
```

```
*Material, name="A356 ALLOY"
*Elastic
 66250., 0.3
*Plastic
   164.,   0.
   196., 0.01
   216., 0.02
   231., 0.03
   244., 0.04
   255., 0.05
   264., 0.06
   272., 0.07
   280., 0.08
   286., 0.09
   292.,  0.1
   297., 0.11
   302., 0.12
  306.7, 0.13
 310.75, 0.14
  314.7, 0.15
  317.2, 0.16
**
** INTERACTION PROPERTIES
**
**Definition of type of contact between the wheel and the platen
```

```
**
*Surface Interaction, name=IntProp-1
1.,
*Friction
0.,
*Surface Behavior, pressure-overclosure=HARD
**
** Interaction: Int-1
*Contact Pair, interaction=IntProp-1, type=SURFACE TO SURFACE, no thickness,
        adjust=0.0
Wheel_slave_surf, Platen-1.Platen_mater_surface
**********************************************************************
*******BOUNDARY AND INITIAL CONDITIONS*****************************
**********************************************************************
** BOUNDARY CONDITIONS
**
** Name: RP_fixed Type: Displacement/Rotation
*Boundary
**
**Fix the reference node on the platen in all directions except vertical
** Name: Tie_node_fixed Type: Symmetry/Antisymmetry/Encastre
**
*Boundary
**
**Fix the bolt holes in all degree of freedom
```

**

**Import the initial stress state of the wheel

*MAP SOLUTION, STEP=1, INC=4

**

****

*******STEP1: ACHIEVE EQUILIBIRIUM**********************************

****

**

** STEP: Acheive_equilibirium

**

*Step, name=Acheive_equilibirium

*Static

0.1, 1., 1e-05, 0.5

**

** INTERACTIONS

**

** Interaction: Int-1

*Model Change, type=CONTACT PAIR, remove

Wheel_slave_surf, Platen-1.Platen_mater_surface

**

** OUTPUT REQUESTS

**

*Restart, write, frequency=0

**

** FIELD OUTPUT: F-Output-1

**

*Output, field, frequency=4

*Node Output

RF, RT, U, UR, UT

*Element Output, directions=YES

E, EE, PE, PEEQ, S

*Contact Output

CSTRESS,

*Output, history, frequency=0

*End Step

****

*******STEP2: ESTABLISH CONTACT BETWEEN PLATEN AND WHEEL *******

****

** STEP: Establish contact

**

*Step, name="Establish contact"

*Static

0.025, 1., 1e-05, 0.025

**

** BOUNDARY CONDITIONS

**

** Name: Move_platen_establish_contact Type: Displacement/Rotation

*Boundary

**

**Apply boundary condition on the reference node of the platen

```
**
**
** INTERACTIONS
**
** Interaction: Int-1
*Model Change, type=CONTACT PAIR, add
Wheel_slave_surf, Platen-1.Platen_mater_surface
**
** OUTPUT REQUESTS
**
*Restart, write, frequency=0
**
** FIELD OUTPUT: F-Output-1
**
*Output, field, frequency=4
*Node Output
RF, RT, U, UR, UT
*Element Output, directions=YES
E, EE, PE, PEEQ, S
*Contact Output
CSTRESS,
*Output, history, frequency=0
*End Step
**********************************************************************
*******STEP3: APPLY RIM INDENTATION LOAD**************************
```

```
**********************************************************************
** STEP: Apply_load
**
*Step, name=Apply_load
*Static
0.025, 1., 1e-05, 0.05
**
** BOUNDARY CONDITIONS
**
**Remove the displacement boundary condition from the reference node of the platen
**
** LOADS
**
** Name: Load_applied   Type: Concentrated force
*Cload
**
**Apply concentrated load on the reference node of the platen
**
** OUTPUT REQUESTS
**
*Restart, write, frequency=0
**
** FIELD OUTPUT: F-Output-1
**
*Output, field, frequency=4
```

*Node Output

RF, RT, U, UR, UT

*Element Output, directions=YES

E, EE, PE, PEEQ, S

*Contact Output

CSTRESS,

*Output, history, frequency=0

*End Step

****

*******STEP4: REMOVE RIM INDENTATION LOAD**********

****

** STEP: Remove_load

**

*Step, name=Remove_load

*Static

0.1, 1., 1e-05, 0.1

**

** LOADS

**

** Name: Load_applied   Type: Concentrated force

*Cload

**Modify the concentrated force load to zero

**

** OUTPUT REQUESTS

**

*Restart, write, frequency=0

**

** FIELD OUTPUT: F-Output-1

**

*Output, field, frequency=4

*Node Output

RF, RT, U, UR, UT

*Element Output, directions=YES

E, EE, PE, PEEQ, S

*Contact Output

CSTRESS,

*Output, history, frequency=0

*End Step

****

*******STEP5: REMOVE CONTACT BETWEEN WHEEL AND PLATEN*********

****

** STEP: Remove_contact

**

*Step, name=Remove_contact

*Static

0.1, 1., 1e-05, 1.

**

**

** Interaction: Int-1

*Model Change, type=CONTACT PAIR, remove

Wheel_slave_surf, Platen-1.Platen_mater_surface

**

** OUTPUT REQUESTS

**

*Restart, write, frequency=0

**

** FIELD OUTPUT: F-Output-1

**

*Output, field, frequency=4

*Node Output

RF, RT, U, UR, UT

*Element Output, directions=YES

E, EE, PE, PEEQ, S

*Contact Output

CSTRESS,

*Output, history, frequency=0

*End Step

****

*******STEP6: MOVE PLATEN AWAY**********

****

** STEP: Move_platen_away

**

*Step, name=Move_platen_away

*Static

0.1, 1., 1e-05, 0.5

```
**
** BOUNDARY CONDITIONS
**
** Name: Move_platen_away Type: Displacement/Rotation
*Boundary
**
**Apply displacement boundary condition on the reference node of the platen and move
**it away from the wheel
**
** OUTPUT REQUESTS
**
*Restart, write, frequency=0
**
** FIELD OUTPUT: F-Output-1
**
*Output, field, frequency=4
*Node Output
RF, RT, U, UR, UT
*Element Output, directions=YES
E, EE, PE, PEEQ, S
*Contact Output
CSTRESS,
*Output, history, frequency=0
*End Step
**********************************************************************
```

*******RIM INDENTATION MODEL'S STEPS*******************************

****

******RADIAL FATIGUE TEST MODEL STARTS*****************************

******STEP7: APPLY PRESSURE ON THE WHEEL*************************

****

** STEP: Apply_pressure

**

*Step, name=Apply_pressure

*Static

0.1, 1., 1e-05, 0.25

**

** LOADS

**

** Name: Pressure_load_wheel   Type: Pressure

*Dsload

FULL_WHEEL_MESHED-1.Pressure_area, P, 0.413685

**

** OUTPUT REQUESTS

**

*Restart, write, frequency=0

**

** FIELD OUTPUT: F-Output-1

**

*Output, field, frequency=4

*Node Output

RF, RT, U, UR, UT

*Element Output, directions=YES

E, EE, PE, PEEQ, S

*Contact Output

CSTRESS,

*Output, history, frequency=0

*End Step

****

*******STEP8: APPLY RADIAL LOAD **********

****

** STEP: Apply_radial_Load

**

*Step, name=Apply_radial_Load

*Static

0.025, 1., 1e-05, 0.025

**

** LOADS

**

** Name: Radial_Load Type: Surface traction

*Dsload, follower=NO, orientation=FULL_WHEEL_MESHED-1-Cyl_sys, constant resultant=YES

FULL_WHEEL_MESHED-1.Bead_surface, TRVECNU, 1., -1., 0., 0.

**

** OUTPUT REQUESTS

**

*Restart, write, frequency=0

**

** FIELD OUTPUT: F-Output-1

**

*Output, field

*Node Output

RF, RT, U, UR, UT

*Element Output, directions=YES

E, EE, PE, PEEQ, S

*Contact Output

CSTRESS,

*Output, history, frequency=0

*End Step